

A Morphologic and Alignment Analysis of Volcanic Ridge and Cones to  
Determine Stress Directions, Adare Basin, Antarctica.

Senior Thesis

Submitted in partial fulfillment of the requirements for the

Bachelor of Science Degree

At The Ohio State University

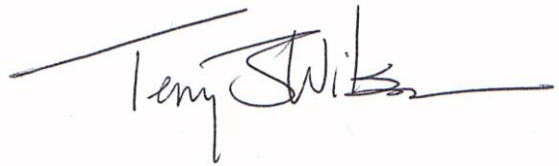
By

Brian Vargo

The Ohio State University

2014

Approved by

A handwritten signature in black ink, appearing to read "Terry J. Wilson", is written over a horizontal line.

Terry J. Wilson, Advisor  
School of Earth Science

## **Abstract**

This study examines the tectonic forces at work in a region of Antarctica in the northwest Ross Sea, along the western boundary of the West Antarctic Rift System. The focus is on analysis of a submarine volcanic ridge and associated cones found in the Adare Basin. Multibeam sonar data were examined using spatial analysis tools to map the morphology of the seafloor, specifically to map volcanic cones and their alignments to constrain crustal stresses. The analysis revealed that the NE-SW volcanic ridge is composed of four segments of varying trend. Cone alignments and the long axes of elongate volcanic cones have trends generally parallel to the ridge segments. These results suggest that the crustal stresses at the time of magmatism consisted of NE-SW maximum and NW-SE minimum horizontal stresses. The volcanic ridge, cones and cone alignments are parallel to and spatially linked with mapped normal faults in the area. The presence of en echelon cone alignments in a zone that runs parallel to the volcanic ridge and fault trends suggests that right-lateral shear occurred along pre-existing faults at the time of emplacement. An overall rhombic shape of the ridge and a wider central ridge area are consistent with shear along curved, pre-existing faults. Pre-existing rift faults apparently acted as conduits for magmatism to reach the surface.

## **Acknowledgements**

I would first like to give many thanks to my advisor, Dr. Terry Wilson, for giving me the opportunity to work with her and this subject, the incredible leadership and advice that she has provided me with while working on this research has been invaluable. She has guided me through my more difficult parts of my research with incredible clarity and patience, even from half way around the world.

The Shell Exploration and Production Company gets a very large thank you for the opportunity to work as an intern this summer with the Shell Undergraduate Research Experience. The internship allowed me to get an incredible amount of work done over the summer and I would not have completed this research without that opportunity.

I would also like to thank Jie Chen for his assistance with Fledermaus and Linux. Without him I would have spent many more hours just transferring the data within the Linux system. He was always happy to help me with any issue.

Stephanie Konfal also deserves a big thank you. Her incredible knowledge of the ArcGIS program was helpful throughout my research process and has enhanced my previous knowledge of the program to take with me into my career. Like Jie she was always happy to help with any little issue I may have been having.

I would like to thank the School of Earth Sciences faculty and staff for instilling in me the knowledge required to work on this research. I would also like to mention my fellow students within the department for their support and assistance throughout my time in the program.

I would finally like to thank the people and organizations that provided the raw data used within this research. The data were provided by the Antarctic Southern Portal via the Marine

Geoscience Data System (MGDS) and International Bathymetric Chart of the Southern Ocean (IBCSO). These two data systems provided the basis of my research and I could not have done it without them.

## Table of Contents

|   |    |
|---|----|
| Abstract.....   | i  |
| Acknowledgements.....   | ii |
| List of Figures.....  | v  |
| List of Tables.....   | vi |
| Introduction.....   | 1  |
| Geologic Setting.....   | 2  |
| Methods.....  | 9  |
| Determining Stress through Volcanic Alignment.....            | 9  |
| Bathymetric Analysis and Processing.....                      | 9  |
| Analysis of Cone Slope.....                                   | 17 |
| Charting of Cones and Determination of Ellipsoidal Shape..... | 21 |
| Cone Alignment and Selection of Reliability.....              | 23 |
| Results.....  | 25 |
| Morphologic Provinces.....                                    | 25 |
| Ridge and Vent Morphology.....                                | 27 |
| Cone Elongation and Vent Alignment.....                       | 27 |
| Discussion.....   | 40 |
| Mapping Seafloor Terrain and Vent Alignment.....              | 40 |

|   |    |
|---|----|
| Volcanic Ridge and Alignment Relative to Regional Rift Structure..... | 40 |
| Conclusion.....   | 47 |
| Suggestions for Future Research.....                                  | 47 |
| References Cited.....   | 49 |
| Appendix A: Excel Cone Profiles.....                                  | 51 |

### **List of Figures**

|   |    |
|---|----|
| 1. Maximum vs. minimum stress associated with elongate volcanoes..... | 2  |
| 2. Rift zone cross section.....                                       | 3  |
| 3. Map of West Antarctic Rift System (WARS).....                      | 3  |
| 4a. Summary of Adare basin faults and volcanics.....                  | 4  |
| 4b. Cross section of the southern Adare Trough.....                   | 5  |
| 5. Tectonic map of the Ross Sea region.....                           | 7  |
| 6. Adare Basin dredge sites.....                                      | 8  |
| 7a. Image of R/V Nathaniel B. Palmer.....                             | 10 |
| 7b. Artist representation of multibeam sonar.....                     | 11 |
| 8. Cruise tracks of R/V Nathaniel B. Palmer.....                      | 12 |
| 9a. Fledermaus 30 meter bins.....                                     | 14 |
| 9b. Fledermaus 50 meter bins.....                                     | 14 |
| 9c. Fledermaus 100 meter bins.....                                    | 14 |
| 9d. Fledermaus composite (different scales).....                      | 14 |
| 10. Composite fixed scale Fledermaus image.....                       | 15 |
| 11a. Fledermaus edit area.....  | 16 |
| 11b. Cube editor in Fledermaus.....                                   | 16 |
| 11c. Anomalous high spike in Fledermaus.....                          | 16 |
| 11d. Anomalous high spike in cube editor.....                         | 16 |
| 12a. Hillshade of study area.....                                     | 17 |
| 12b. Broad Bathymetric Pixel Index (BBPI).....                        | 17 |
| 12c. Fine Bathymetric Pixel Index (FBPI).....                         | 18 |
| 12d. Overlay of FBPI on BBPI.....                                     | 18 |
| 13. BPI value grid.....   | 19 |
| 14a. Numbered individual cones.....                                   | 20 |
| 14b. Cross sections of individual cones.....                          | 20 |
| 15. Excel profile graphs.....   | 21 |

|  |    |
|--|----|
| 16. Vent alignment parameters and Cone axial ratio.....        | 24 |
| 17. BBPI-FBPI overlay.....                                     | 26 |
| 18. Ridge segment histogram.....                               | 28 |
| 19. Fledermaus view from E-W.....                              | 29 |
| 20. Fledermaus view from N-S.....                              | 30 |
| 21. Fledermaus view from WSW-ENE.....                          | 31 |
| 22. Percent change in slope map.....                           | 33 |
| 23. Polygon outlines of cone bases.....                        | 34 |
| 24. Ellipse long axis histogram.....                           | 35 |
| 25. Cone alignment histogram.....                              | 35 |
| 26. Cone ellipses with long and short axis.....                | 37 |
| 27. Ellipses with cone alignments.....                         | 38 |
| 28. Cone and ridge alignments.....                             | 39 |
| 29. Shear stress diagram.....                                  | 43 |
| 30. Numbered cone alignments and ridge alignment segments..... | 44 |
| 31. Geo-referenced research area and fault map.....            | 45 |
| 32. Magnified ridge and mapped fault area.....                 | 46 |

## List of Tables

|   |    |
|---|----|
| 1. Cruise data files .....                  | 12 |
| 2. Cone alignment reliability criteria..... | 23 |
| 4. Cone slopes.....                         | 32 |
| 3. Cone alignment grades.....               | 36 |

## Introduction

Understanding the effects of stress on the Earth's crust is important for a large range of geologic processes. Crustal stresses can give us insights into current geologic processes and into past events that shaped the world we see today. The primary methods for the determination of crustal stresses are from earthquake seismology and borehole measurements ([http://dc-app3-14.gfz-potsdam.de/pub/stress\\_data/stress\\_data\\_frame.html](http://dc-app3-14.gfz-potsdam.de/pub/stress_data/stress_data_frame.html)). However it is difficult to acquire stress data in Antarctica by these methods due to environmental factors, such as the harsh environment, limited field season and logistics, and geologic factors such as a low recorded seismic activity and very limited borehole drilling.

An effort to obtain crustal stress data in Antarctica involving the analysis of volcanic vent or cone alignments is underway (Paulsen and Wilson, 2009; Paulsen and Wilson, 2010). The widespread occurrence of Cenozoic volcanics in the West Antarctic Rift System (WARS) provides the opportunity to study volcanic fields and map volcanic vent alignments. The alignment of volcanic cones can be used to show radial and hourglass dike patterns around volcanoes that delineate tectonic stress directions [Nakamura et al., 1977]. Indicators of tectonic stresses in a rift setting can include normal faulting, opening-mode fractures and magmatic fissures. Crustal stresses cause the elongation and lineation of volcanic vents and cones (Figure 1).

The focus of this research is to analyze the alignment and elongation of volcanic cones associated with a submarine ridge in the Adare Basin, Antarctica. This research complements similar studies in the Adare region (Rosenbeck, 2013; Barr, 2014) which, together, will allow a better understanding of regional stresses within the crust of the Ross Sea region and the WARS.



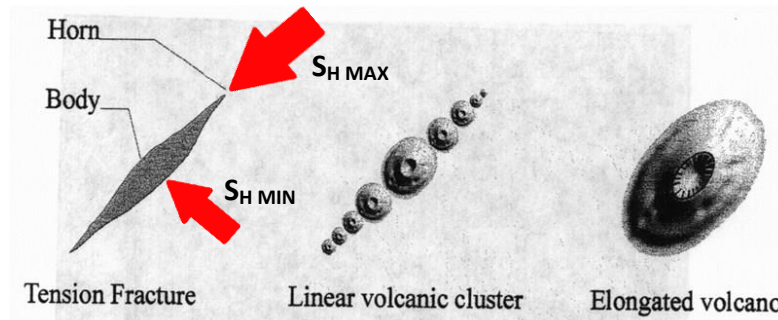


**Figure 1.** Orientation of crustal stresses relative to volcanic fissures. (Adiyaman et. al. 1998)

## Geologic Setting

The study area lies within the submarine Adare Basin, the westernmost rift basin in the West Antarctic Rift System (WARS) [Cande et al., 2000]. The WARS encompasses the Ross Sea and is bordered by the Transantarctic Mountains, separating the East Antarctic craton from younger block assemblages in West Antarctica [Elliot 1992, Heimann et al. 1994]. Rifting occurs where tensional forces in the crust cause normal faulting, which thins the lithosphere, commonly associated with magmatism and volcanic eruptions (Figure 2). The West Antarctic Rift System has experienced many episodes of rifting and is the result of the complex interaction of the Pacific, Australia, Lord Howe Rise, West Antarctic and East Antarctic Plates [Cande et al. 2006]. The WARS in the Ross Embayment (Figure 3) is composed of a series of rift basins that date back to the Jurassic, with the presence of continental flood basalts along the Transantarctic Mountains indicating the earliest rifting and oldest evidence for the breakup of Gondwanaland [Heimann et al., 1994]. The total extension in the WARS is difficult to calculate, but is believed to be on the order of 400 km [Fitzgerald, 2002]. From the late Cretaceous and into the late Cenozoic, a series of rift basins with a N-S orientation developed in the Ross Embayment (Figure 2), including the Victoria Land Basin, Northern Basin, Central Trough, and Eastern Basin [Granot et al. 2010].

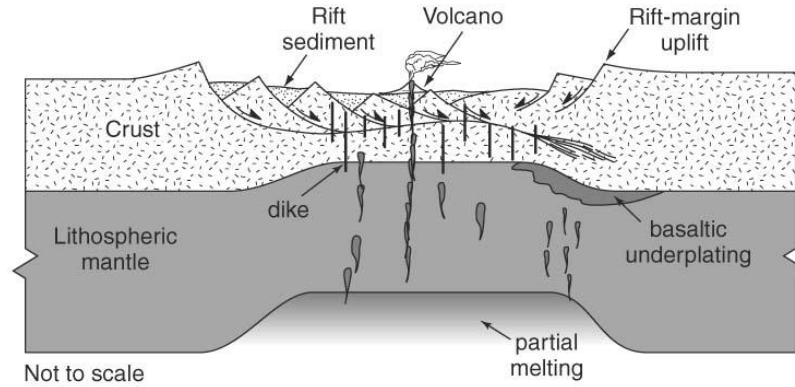


**Figure 2.** A cross-sectional diagram of an active rift zone [Van der Pluijm and Marshak, 2004]

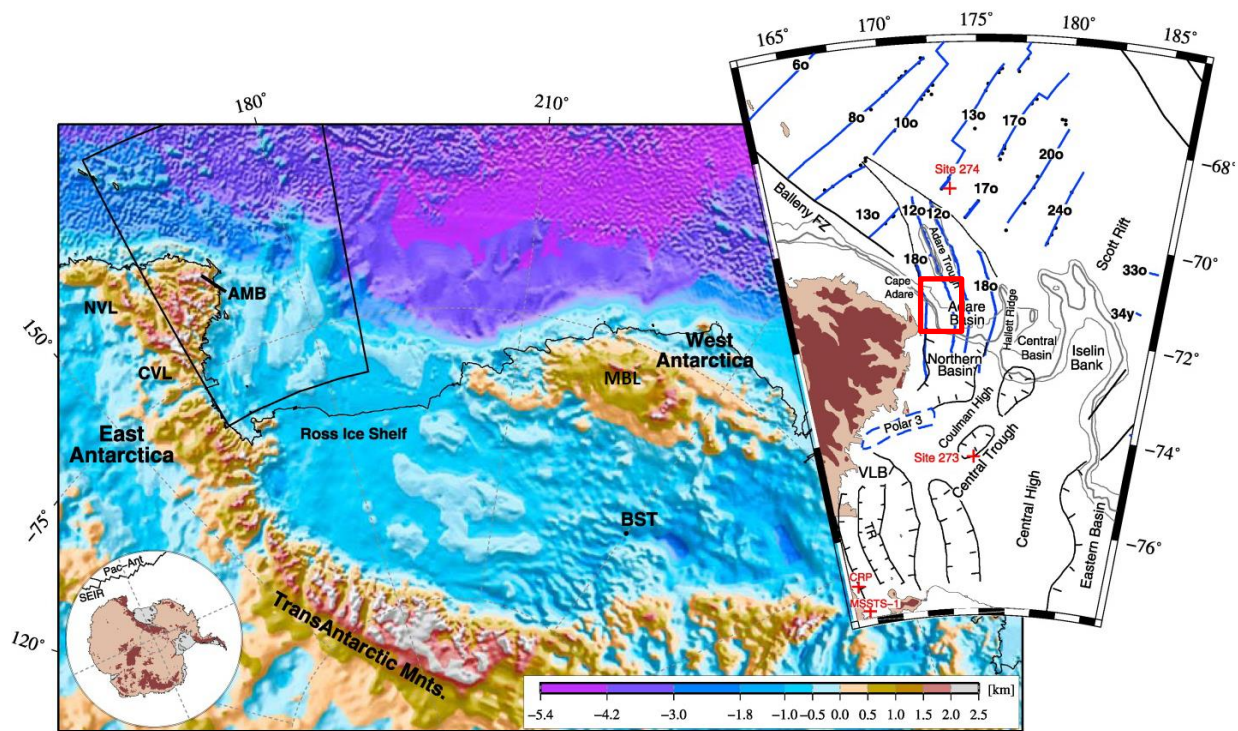


**Figure 3.** Map of the Ross Embayment region of West Antarctica where the WARS extends between the Transantarctic Mountains and the Marie Byrd Land block (MBL) in West Antarctica. The inset shows the rift basins of the Ross Sea, including the Adare Basin. The area of this study is highlighted on the inset with a red box located just south of the Adare trough. [Granot et al., 2010]

The Adare Basin is an area located off the continental shelf of Antarctica bounded to the south by the Northern Basin and to the west by Cape Adare. The Adare Basin is a spreading

center characterized by linear magnetic anomalies (Figure 3, inset) that record east-west seafloor spreading from 46–26 Ma [Cande et al 2000]. The Adare Trough is a rift that is located within the Adare Basin. According to Granot et al. [2010], the Adare Basin experienced three distinct tectonic episodes after seafloor spreading: 1) localized fault reactivation near the end of the seafloor spreading in the late Paleogene (~24 Ma) marking the onset of the Adare Trough formation, 2) an extensional event associated with normal faulting and tilted blocks in the early Miocene (~17 Ma), and 3) a period of extensive volcanism from the Pliocene to the present-day (<5 Ma) accompanied by near-vertical normal faulting. Figures 4 a and b show the Adare Trough, faults and volcanics formed by these multiple tectonic episodes.

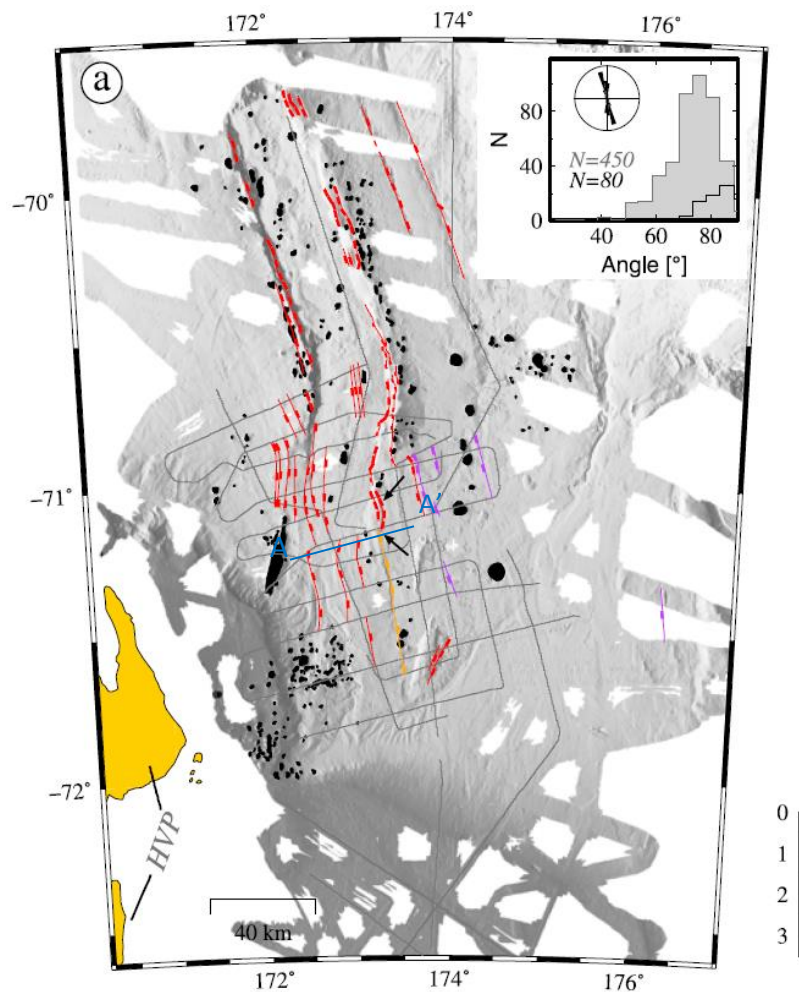


**Figure 4a.** Summary of the Adare Basin showing faults and volcanic features. The bathymetric topography was gathered from multibeam sonar data. Faults (red) were interpreted across more than one seismic profile and seafloor volcanics (black) were mapped using a combination of multibeam sonar and seismic data. The inset histogram shows the apparent dip of all 450 faults (gray) and true dip of the 80 faults mapped on multiple seismic lines (black), and shows corresponding fault strikes on the rose diagram with a maximum radius representing 30 fault segments [Granot et al. 2010].



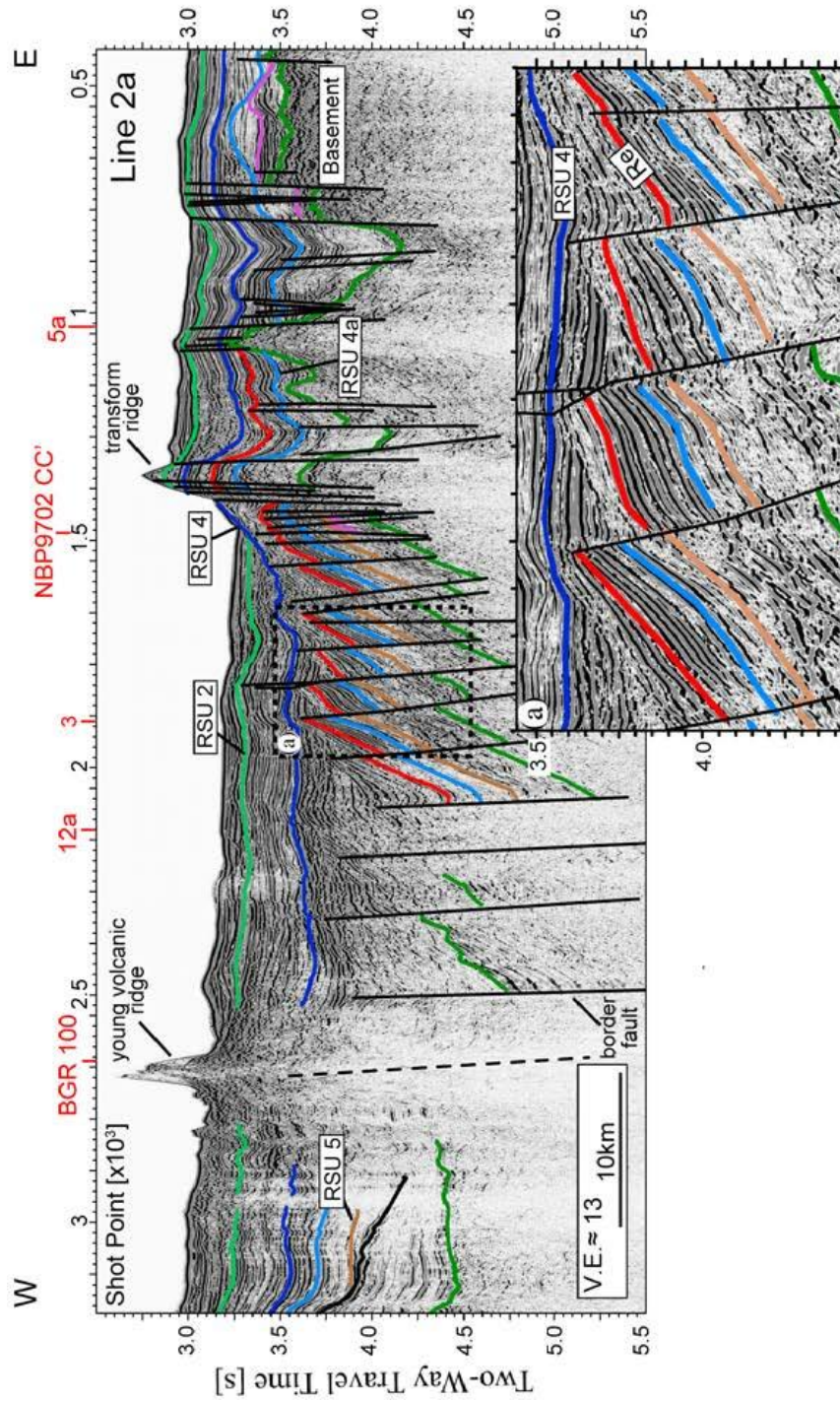


**Figure 4b.** Profile 2a shows tilted blocks with the recent to active volcanic ridge on its western side being the northern most part of the volcanic ridge studied in this research. Red lines trace the base of the Mid-Miocene and Pliocene units, respectively. Top of oceanic basement is shown by the green line. Regional location of the cross section line represented by the line A-A' on Figure 3a [Granot et al. 2010].

The late Paleogene (~24 Ma) faulting and uplift of the eastern and western flanks of the southern Adare Trough within the Adare Basin is likely a result of the reactivation of faults within the first 5 Myr after spreading had stopped [Müller et al. 2005], possibly associated with

changes in the regional stress regime [Granot et al. 2010]. This original uplift and faulting is oriented NNW-SSE forming the primary region of the Adare Trough. The early Miocene faulting (~17Ma) created half grabens bounded by east dipping normal faults that produced 3–5 km of extension. Granot et al. [2010] describes the faults between the southern end of the Adare Trough and the continental shelf near Cape Adare as having ~N-S strikes in an en echelon pattern with an overall trend of NE-SW, from just south of the Adare Trough to the Adare Peninsula (Figure 4a). According to Granot et al. (2010), these faults mark the development of a new rift axis that ran from Cape Adare northeast to the Adare Trough and then turned north-northwest along the west flank of the Adare Trough, reactivating the faults along the western flank [Granot et al. 2010]. The most recent tectonic activity in the Adare Basin / Northern Basin region is represented by widespread volcanic activity and near vertical normal faulting, interpreted to cause little extensional strain [Granot et al., 2010]. Volcanism formed hundreds of individual cones (seamounts) and also formed an elongate volcanic ridge (Figure 4a) located offshore of Cape Adare, oriented NE toward the Adare Trough, which is the focus of this study.

The seafloor faulting events of the Adare Basin are linked with faulting in the continental crust in northern Victoria Land (Figure 5). According to Granot et al. [2010], the landward trend of the offshore rift suggests that deformation continued beyond the Adare Basin to the southwest, probably on, or very close to, Cape Adare. Structural mapping reported in Faccenna et al. [2008] showed that a set of NE–SW striking, eastward dipping normal faults was active since the middle Miocene in the Admiralty Block, the northernmost block of Victoria Land (Figure 5). This suggests that the faulting events that created the Adare Trough are related to the faulting seen onshore in northern Victoria Land. However, the volcanic Cape Adare peninsula, inferred by Faccenna et al [2008] to be a fissure-fed volcanic complex, is oriented NNW-SSE, not parallel to

the NE-striking faults onshore and offshore, or the volcanic ridge examined in this study.

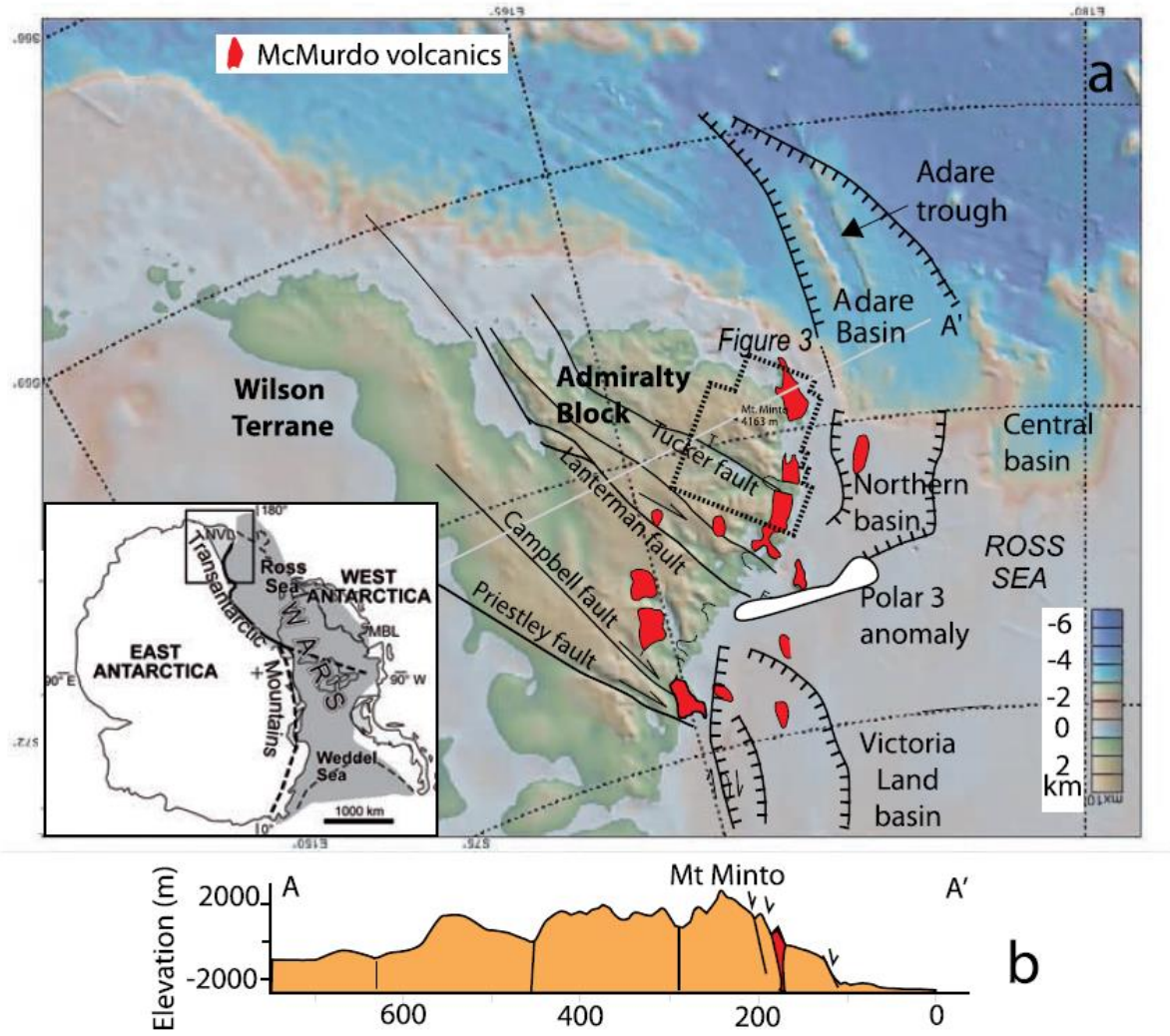


**Figure 5.** Tectonic map of the Ross Sea region showing normal faulting. The A-A' cross section shows down-to-the-east faults of northern Victoria Land to the continental margin. Red denotes onshore exposures of Neogene volcanic rocks of the McMurdo Volcanic Group [Faccenna et al. 2008]

Isotopic dating of dredged samples from volcanic seamounts within the Adare Basin and the Northern Basin (Figure 6) shows an age range of 15.93 Ma to 0.14 Ma for the seafloor volcanics [Panter and Castillo, 2007; Panter, personal comm. 2014]. The age of the dredged rocks from the western scarp of the Adare Trough coincides with the mid-Miocene tectonic event of Granot et al. (2010). Dating of volcanic rocks on the Adare Peninsula shows that the



volcanism in that onshore region is Late Miocene to Early Pliocene in age, from about 12 Ma to 2.2 Ma [Smellie et al. 2011]. The comparison of the ages between the submarine Adare Basin and the continental Adare Peninsula shows volcanism of similar ages indicating a coeval generation, likely associated with the same tectonic events.

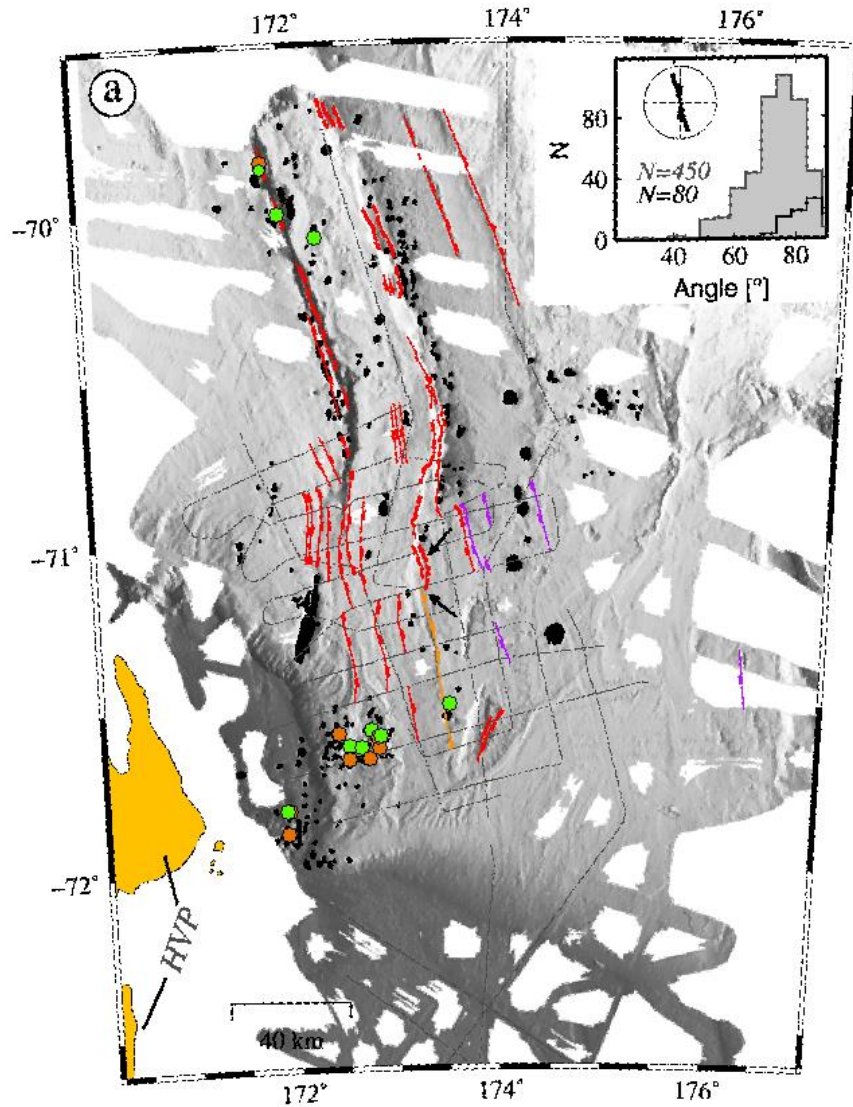


**Figure 6.** Dredge sites in the Adare Basin. Dated samples are represented by the orange dots and undated dredge sites are represented by green dots [Panter, personal comm. 2014].

## **Methods**

### ***Determining Crustal Stress through Volcanic Alignment***

Hydraulic pressure in the Earth's crust can be generated by magma, driving the process of volcanic eruption and resulting in fractures within the host rock. Regional stresses in the crust at the time of the fracturing control the orientation of volcanic features such as magmatic dikes and volcanic vents, including subaerial cones and seamounts [Nakamura et al. 1977]. The effect of the magmatic hydraulic pressure on the regional stress in the crust can result in opening-mode fractures, forming subsurface dikes and surface fissure eruptions, commonly marked by alignments of volcanic vents. The dikes and alignments are oriented perpendicular to the minimum horizontal stress, and parallel to the maximum horizontal stress [Anderson et al. 1951]. Both the orientation of elongate volcanic cones and the lineation defined by multiple cones provide means by which the crustal stresses can be inferred. The trends of these volcanic surface features can be attributed to subsurface feeder dikes aligned with the crustal stresses at the time of formation [Nakamura et al., 1977].

### ***Bathymetric Analysis and Processing***

Bathymetry is a term previously used to describe ocean depth but has since come to describe the topography of the seafloor [NOAA, 2014]. In order to measure the bathymetry of an area of the seafloor accurately, sonar is required. A sonar system makes use of echo sounders, each emitting sound waves, sound velocity sensors, used to receive the return sound signal reflected from the seafloor, and thermosalinographs, monitoring surface water temperature and salinity. The use of these three instruments gives us the ability to determine depth to the seafloor and to map the topography (Figure 7b). This study uses data acquired by multibeam sonar mounted on the hull of a research vessel, the R/V *Nathaniel B. Palmer* (Figure 7a). Multibeam



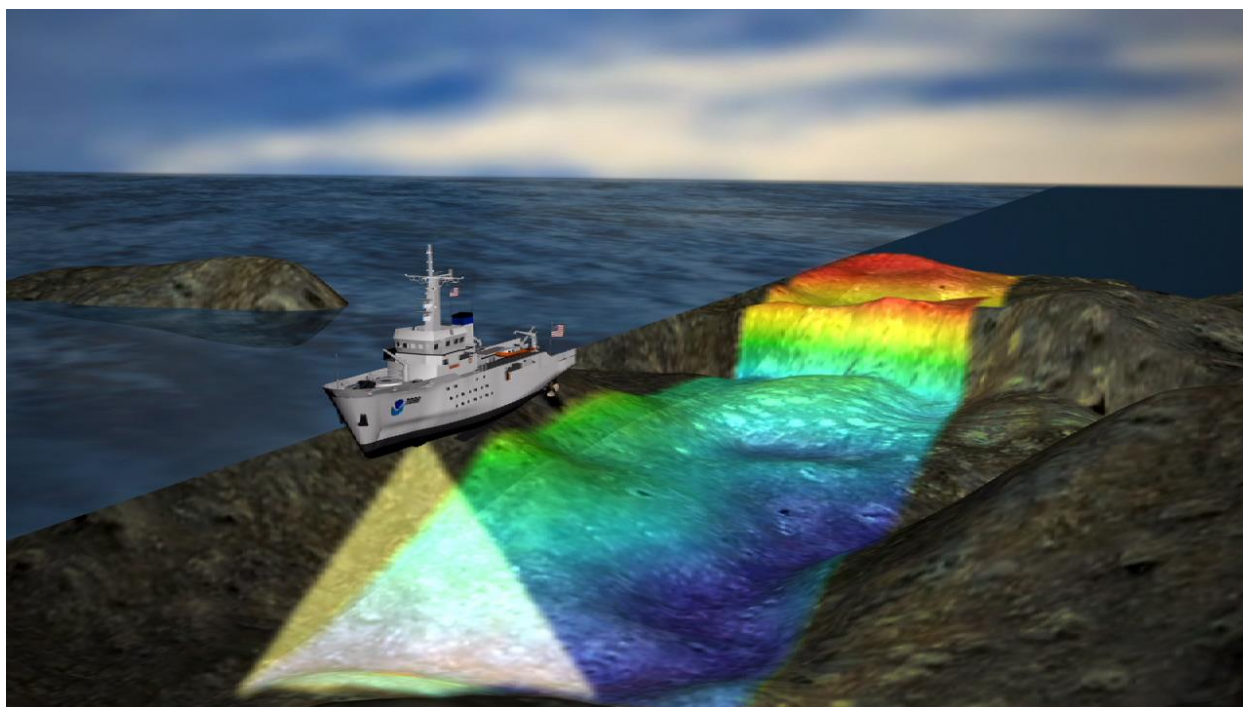
sonar refers to the use of an array of echo sounders mounted on board the vessel, which allows mapping a swath of the seafloor as the ship moves ahead. As the vessel makes a pass over the desired area, the multibeam sonar emits sound waves that travel through the water, bounce off the solid seafloor, and reflect back to the vessel where receivers record the returning signals. Signals are then processed for the travel time of the sound waves from time emitted to time received, using measured variables like seawater temperature and salinity, acquired via the thermosalinographs, to calculate depth to the seafloor. Processed signals can in turn be used to generate a seafloor topographic map by using the data from many ship passes within an area. Anomalies within the data can occur due to the change of salinity or temperature at depth, pitch and roll of the ship, or angle of the signal transmitter in relation to the submarine features.

The data used in this thesis were obtained on board the R/V *Nathaniel B. Palmer* in the northwest Ross Sea off the coast of the Adare Peninsula located in north Victoria Land, and supplemented by data from the International Bathymetric Chart of the Southern Ocean (IBCSO) program. All cruise data from the *Palmer* are archived through the Southern Antarctic Ocean Portal



**Figure 7a (Left)** The R/V Nathaniel B. Palmer in 2012  
[<http://photolibrary.usap.gov/>]

**Figure 7b (Below)** An artist representation of the way sonar is used to map the seafloor topography  
[<http://www.hydropalooza.noaa.gov/>]



(SAOP), associated with the Marine Geoscience Data System (MGDS) [<http://www.marine-geo.org/portals/antarctic/>]. The MGDS's GeoMapApp 3.3.0 was utilized to locate the cruises of the R/V *Nathaniel B. Palmer* that coincided with the area of research (Figure 8 and Table 1). GeoMapApp is an “application [that] provides direct access to the Global Multi-Resolution Topography (GMRT) compilation that hosts high resolution (~100 m node spacing) bathymetry from multibeam data for ocean areas” [<http://www.geomapapp.org/index.htm>]. The MGDS data were downloaded in an MBSystems format. The IBCSO data were downloaded as a .tif that could be implemented directly into ArcGIS. The MBSystems data needed to be converted to ASCII format, representing the latitude, longitude and depth (xyz), using the MBSystems software package on a Linux-based computer. The ASCII data were then uploaded into Fledermaus software from QPS. Fledermaus is a 3-D geo-spatial analysis and editing software that allows the user to view and edit the ASCII data in a 3-D environment.

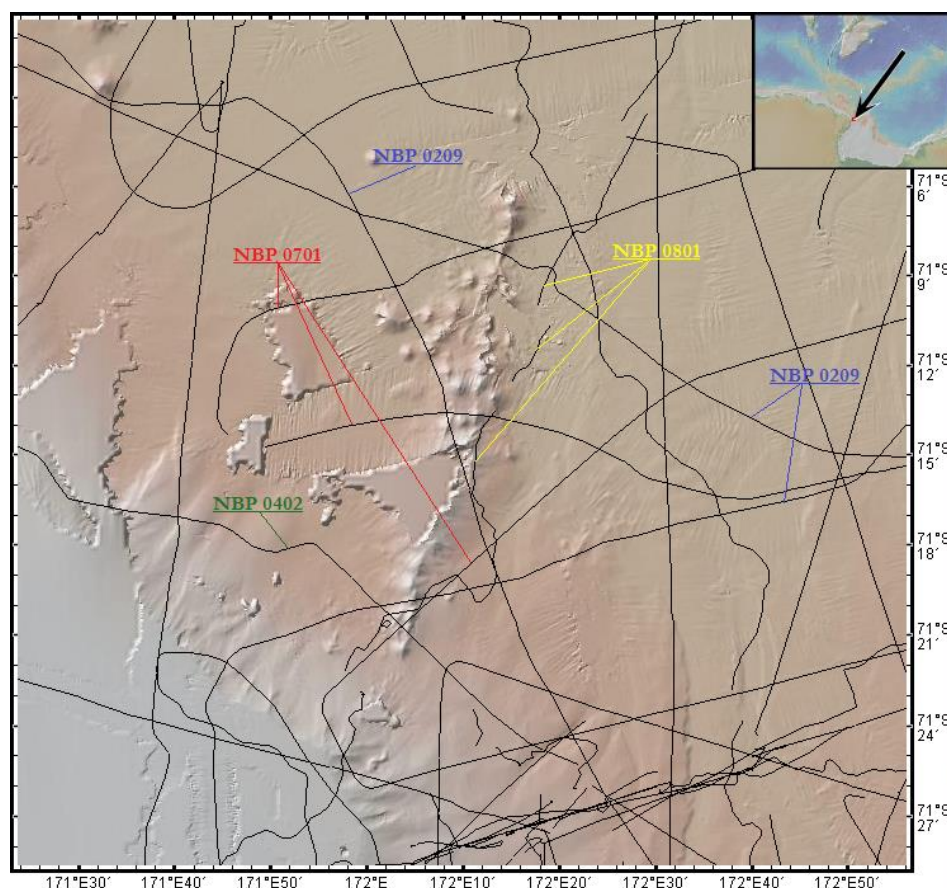


**Figure 8.** Cruise paths of the R/V Nathaniel B. Palmer within the research area, labeled cruise paths were the source of data for the research.

**Table 1.** Individual data files used from each specific cruise.

| Data files utilized from the R/V <i>Nathaniel B. Palmer</i> cruises |         |         |         |
|---|---------|---------|---------|
| NBP0209   | NBP0402 | NBP0701 | NBP0801 |
| 0234  | 0686    | 0261    | 0123    |
| 0268  | 0687    | 0262    |         |
| 0269  | 0689    | 0263    |         |
| 0270  | 0690    | 0264    |         |
| 0300  | 0691    | 0267    |         |
| 0301  |         | 0268    |         |
|   |         | 0269    |         |
|   |         | 0512    |         |
|   |         | 0513    |         |
|   |         | 0514    |         |

The first steps within Fledermaus required that the optimal resolution of the data, or bin sizes between depth readings, be determined for each cruise to produce the best detail with the

least distortion. For this I determined that three different bin sizes were required, due to the poor data coverage in some areas. These bin sizes were 30 meters, 50 meters and 100 meters (Figures 9a, 9b and 9c respectively). With each bin size determined, I created a single image composite of the three regions with a customized color-depth scale that was consistent with all bin sizes (Figure 10). After the map was generated I was able to begin processing the data by removing any data that were not vital to the study. This included cleaning up the edges of the cruise data, removing portions of the cruise data that lay outside the study area, and deleting anomalous data where depths clearly did not match the surrounding terrain.

Problematic data were associated with the pitch and roll of the ship, making it difficult to collect consistent sonar travel times. When the ship advanced too quickly while collecting sonar data, gaps lacking data formed along the sonar swaths. Sudden changes in the ship's course also result in bad data; all of these sources of poor data are attributed to the inability of the ship to capture the return signal or causing sensors to capture the return signal at a different angle than emitted. The presence of a so-called railroad artifact is also visible as two lines in the center of the swath track parallel to the line of the cruise path. The artifact is attributed to the sensors along the centerline of the ship's hull and always creates downward spikes in the surface. The railroad artifact is still prevalent in my data due to the possibility of losing some geologic data with the removal of the artifact. Similarly, removal of other noisy data that would have resulted in a cleaner image was not done, because it would have limited data coverage of the research area. Poor data included false features such as 3-D spikes that could rise, or fall in the case of the railroad artifact, hundreds of meters at a single data point (Figure 11). Bad data were removed using the 3-D editor in Fledermaus called cube edit, which allowed for the isolation of each data



point as a cube which could then be deleted, thereby removing the corresponding spurious feature spike.

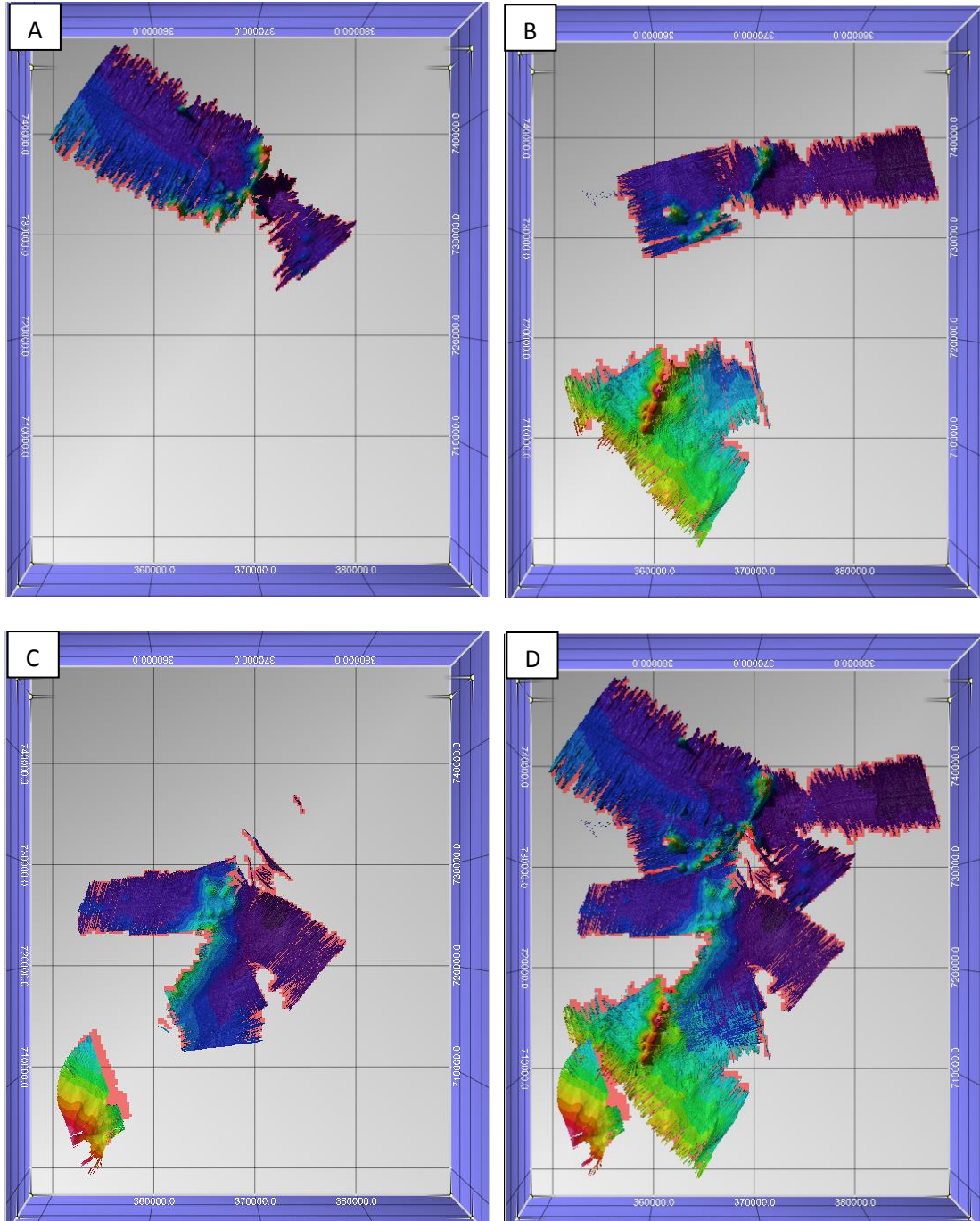


**Figure 9.** Cruise data as displayed in Fledermaus with the three different bin sizes (a) 30 meter, (b) 50 meter and (c) 100 meter. The last image (d) shows the composite of the three data sets prior to a fixed color scale.

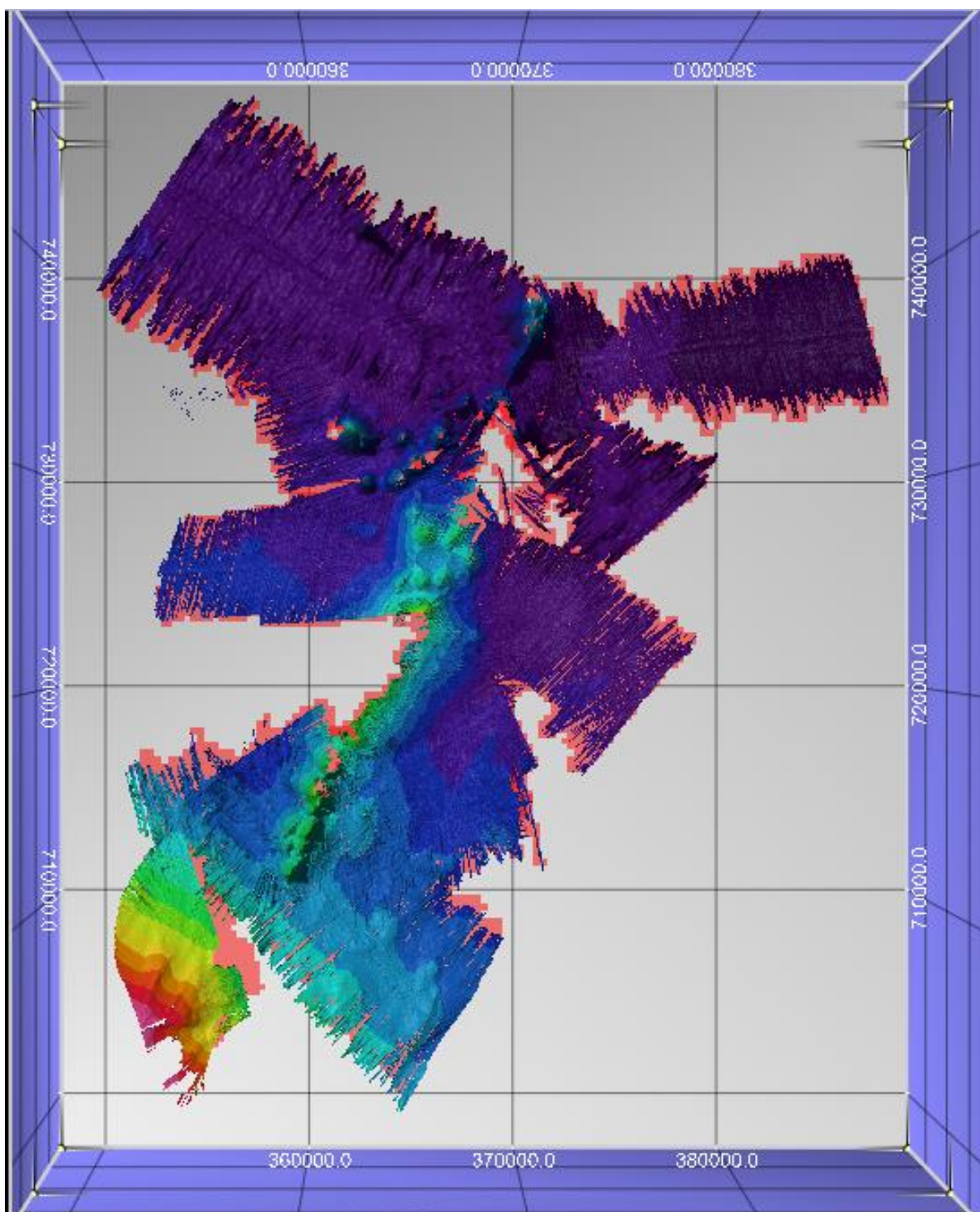


**Figure 10.** A composite map of all bin sizes and a fixed color scale to create a single unified map.

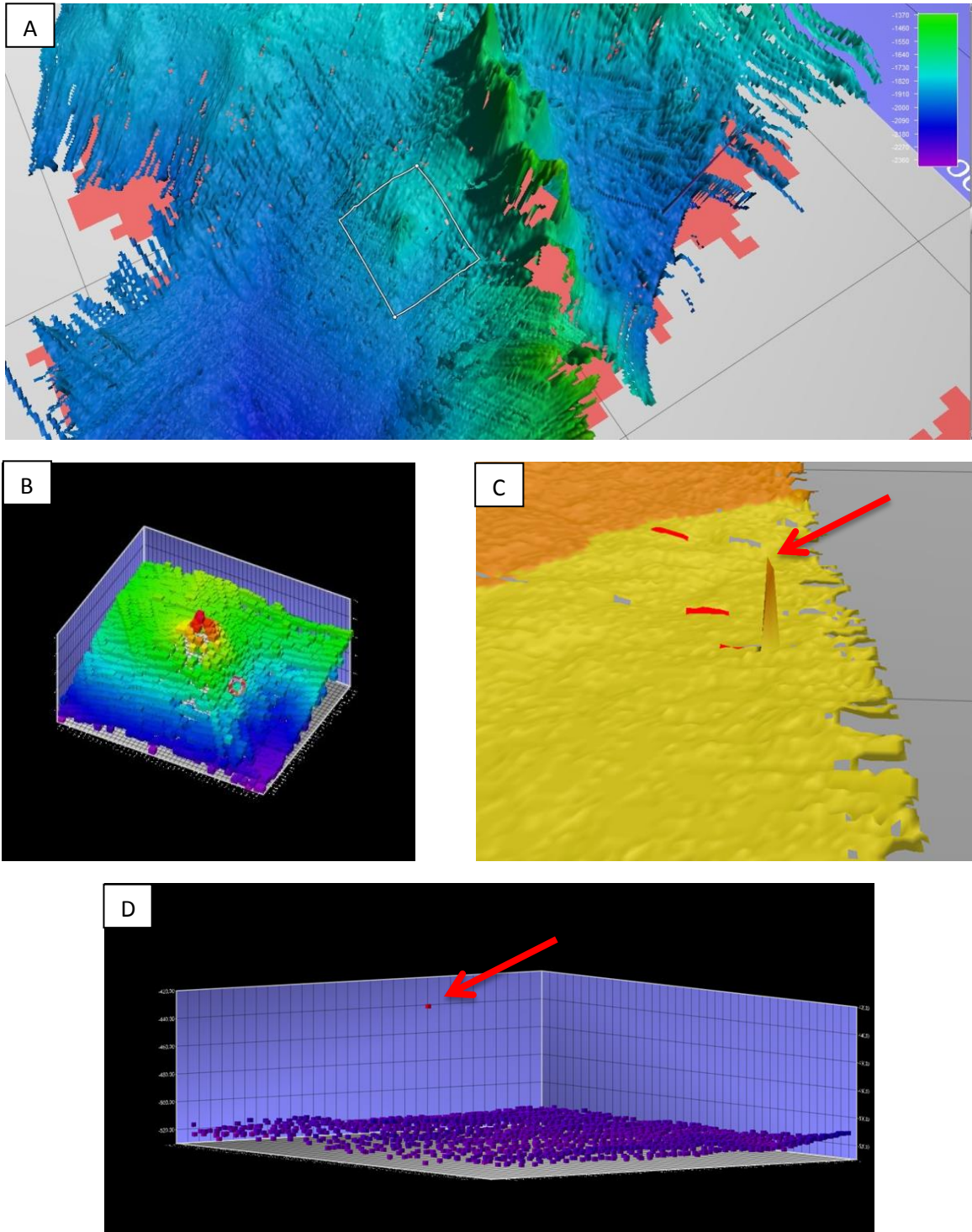


**Figure 11.** (a) Portion of the Fledermaus map showing a selected area to the left of the ridge and rough data along portions of cones and the ridge that could not be removed, (b) selected portion from above as seen in the Fledermaus cube editor. (c) Example of the 3-D spike for anomalous data and (d) the corresponding cube in the editor.



### *Analysis of Cone Slope*

The compiled and cleaned bathymetric data were transferred into the ArcGIS 10.1 program. The MGDS and IBCSO data were combined to create a single mosaic. Whereas the MGDS data were gridded in 30 m, 50 m and 100 m bin sizes, the IBCSO project data are much coarser resolution, with 500 m bin size. The IBCSO bin size is too large to give any data in the detail required for this mapping project, but the IBCSO data were used to fill in gaps in the MGDS multibeam data and assist in a better understanding of the study area overall. A final composite mosaic with MGDS and IBSCO data was regrided at 30 m bin size.

ArcGIS functions were used to generate slope and hillshade maps (Figure 12a) to portray the shape and degree of slope for the area.

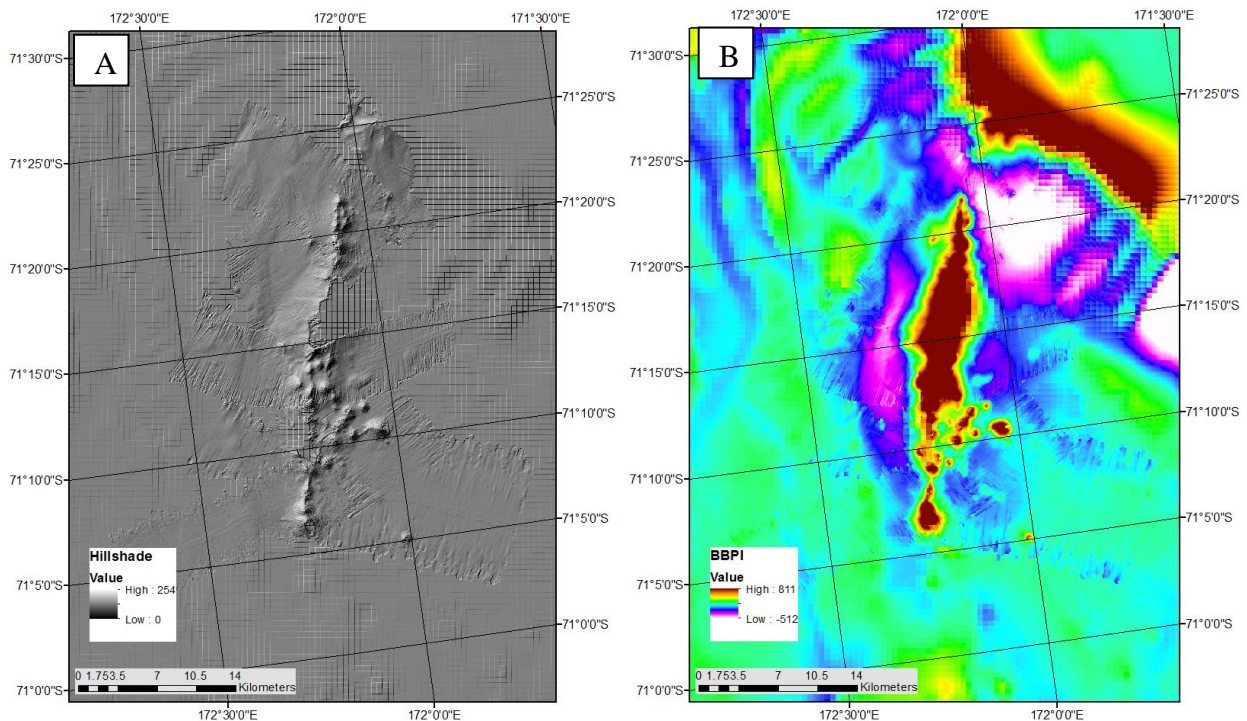
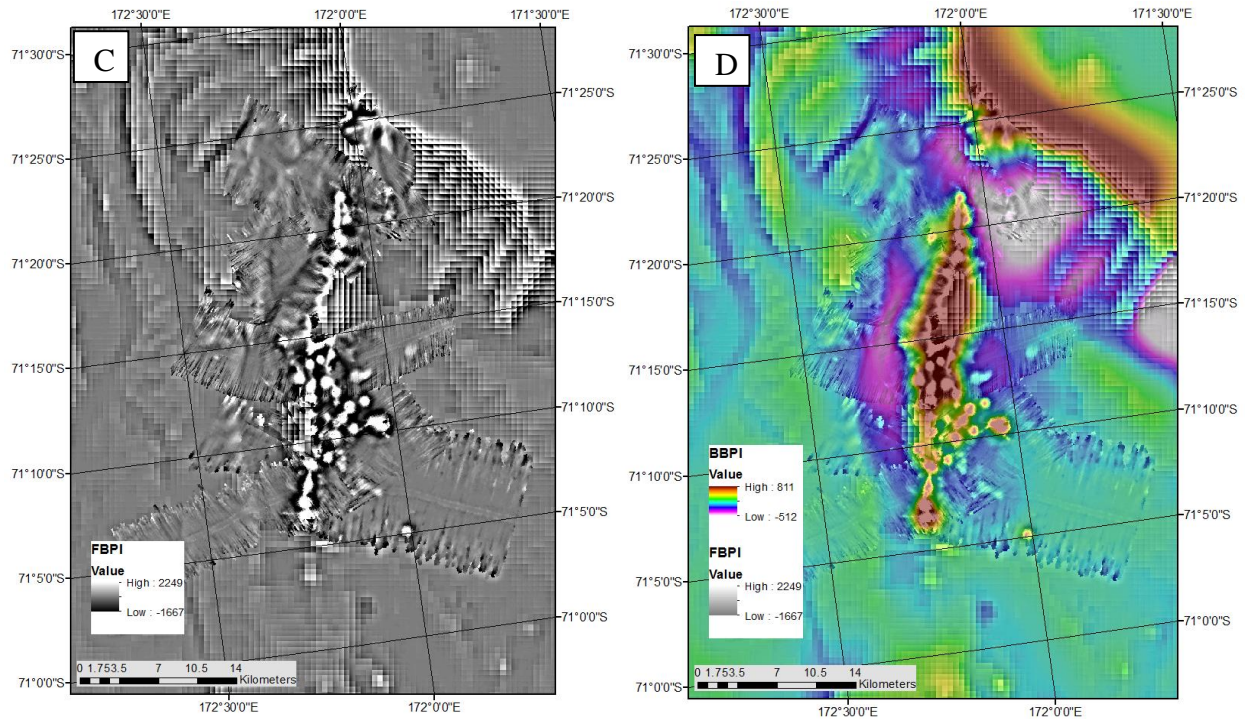


**FIGURE 12.** (a) Hillshade of the study area with an illumination azimuth of 315 degrees and angle above the horizon of 30 degrees. (b) The BBPI showing regional features, (c) the FBPI showing more specific features representing individual cones, and (d) a composite overlay of the FBPI onto the BBPI with the FBPI at 50% transparency.





The Benthic Terrain Modeler Toolbox (BTMT), an add-on module for ArcGIS, contained tools called the Broad Bathymetric Pixel Index (BBPI) and Fine Bathymetric Pixel Index (FBPI). As explained in the Benthic Terrain Modeler tutorial

[<http://www.arcgis.com/home/item.html?id=b0d0be66fd33440d97e8c83d220e7926>]: “The Bathymetric Position Index (BPI) is a derivative of the input bathymetric data set, and is used to define the location of specific features and regions relative to other features and regions within the same data set.” The Broad Bathymetric Pixel Index (BBPI) delineates long wavelength landscape features where the Fine Scale Bathymetric Pixel Index (FBPI) captures more detailed features [Lanier et al. 2007] (Figure12c-d). According to Lundblad et al. [2006], the output slopes (raster grids) are derived from the maximum rate of change between that cell and its neighbor, an evaluation of the elevation difference between the focal point and the surrounding cells within a defined circle. The evaluation is scaled in one number increments resulting in a numbered grid where a ‘0’ represents no change between neighbors, positive numbers represent

a higher neighbor (ridge) and negative numbers show a lower neighbor (valleys) (Figure 13).

The inner and outer radii used for the analysis were default values of 25m and 250m,

respectively, for the BBPI and 3m and 25m, respectively, for the FBPI.

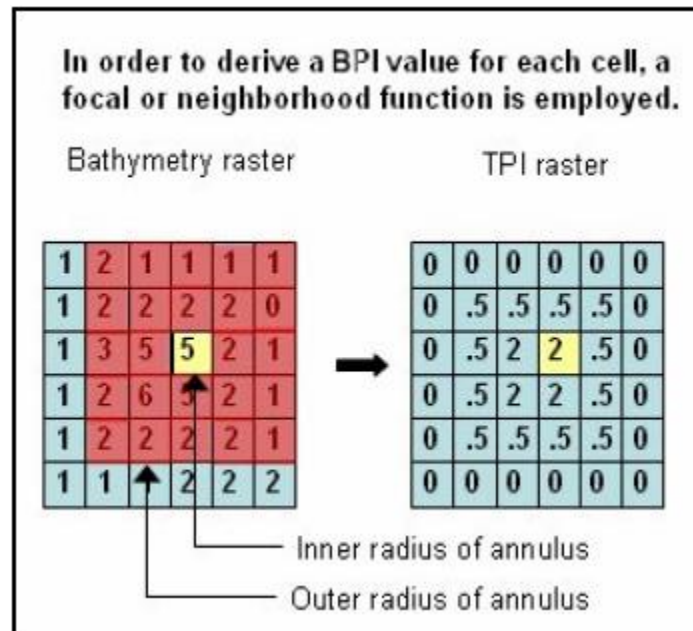


**Figure 13.** A BPI grid showing an example of the comparison of a cell value to the elevations of cells within a defined outer radius and the resulting output raster [Rinehart et al. 2004].

Each identified cone was given a number. 2-D profiles were taken of each cone using the 3-D analyst profile graph tool. This allowed for quantitative measurement of the cone slope angles, including the cone flanks, the break in slope between the flank and the sediment apron and between the sediment apron and the seafloor. With the 2-D profile slope angles, values for the break in slope between the flank slope and the apron slope were determined. This break in slope was used to more map the shape of the base of each cone accurately, eliminating possible distortions from accrued sediments and physical connections to adjacent ridges. A total of 31 cones from this region were analyzed for the flank slope, apron slope, and seafloor slope (Figure 14 and Appendix).

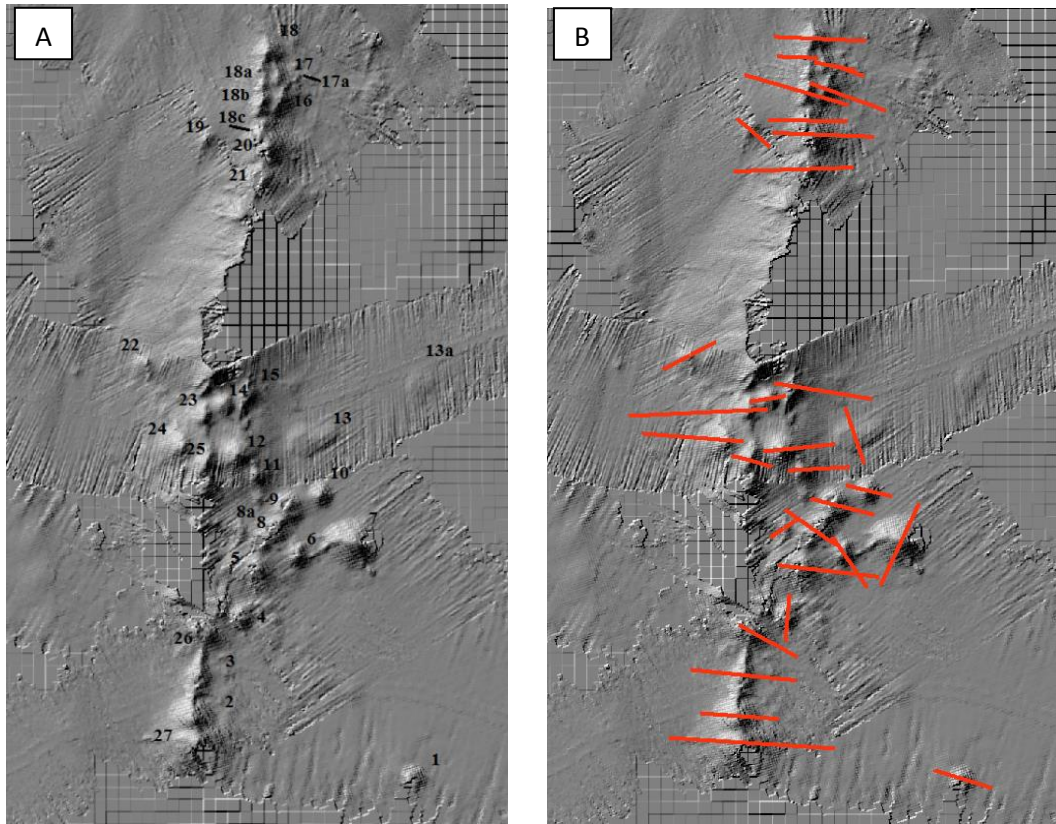


**Figure 14.** (a) Numbered individual cones within the study area. (b) The red lines represent the profile lines for each cone used to determine slope data.

Each profile acquired through the ArcGIS 3-D analyst profile graph tool was exported as a Microsoft Excel spreadsheet. Within Excel, a scatter plot was generated for each cone using smooth lines to show the profile with the x-axis representing distance in meters and the y-axis representing elevation in meters. The slope was then analyzed for a change or break in slope; this break in slope provides information such as boundaries where the true slope meets with the apron and where the apron meets the seafloor. Once the boundaries of the flank, apron and seafloor were determined, trend lines were added to each section of the cone to get a corresponding average slope angle of each portion with a simple rise-run analysis (Figure 15). Some cones were deemed to have only one usable profile side due to either lack of data or influence of the ridge altering the cone shape. All cone profiles are provided in Appendix A.

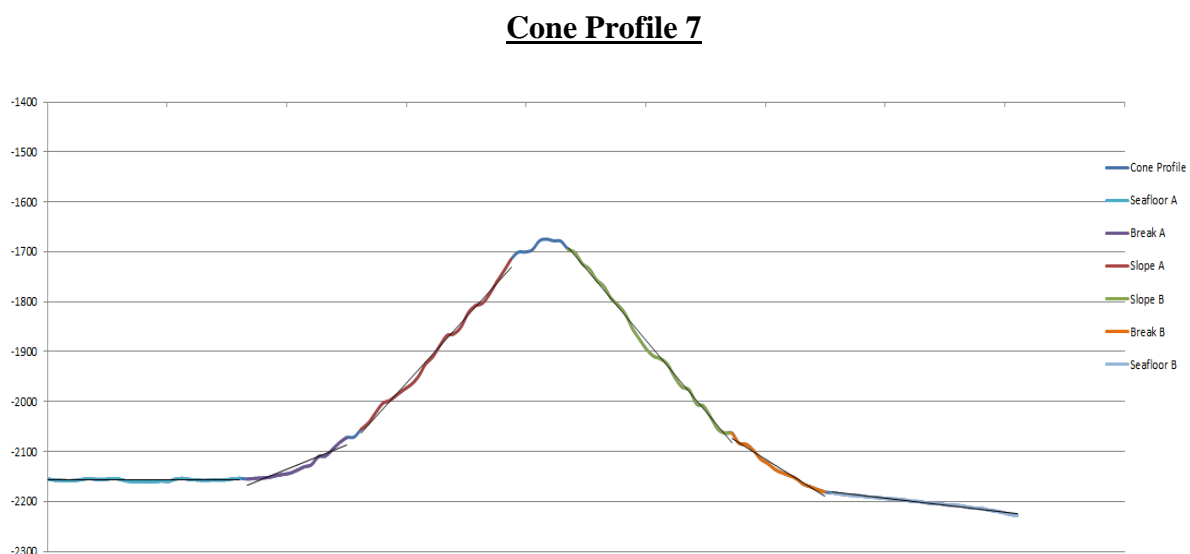
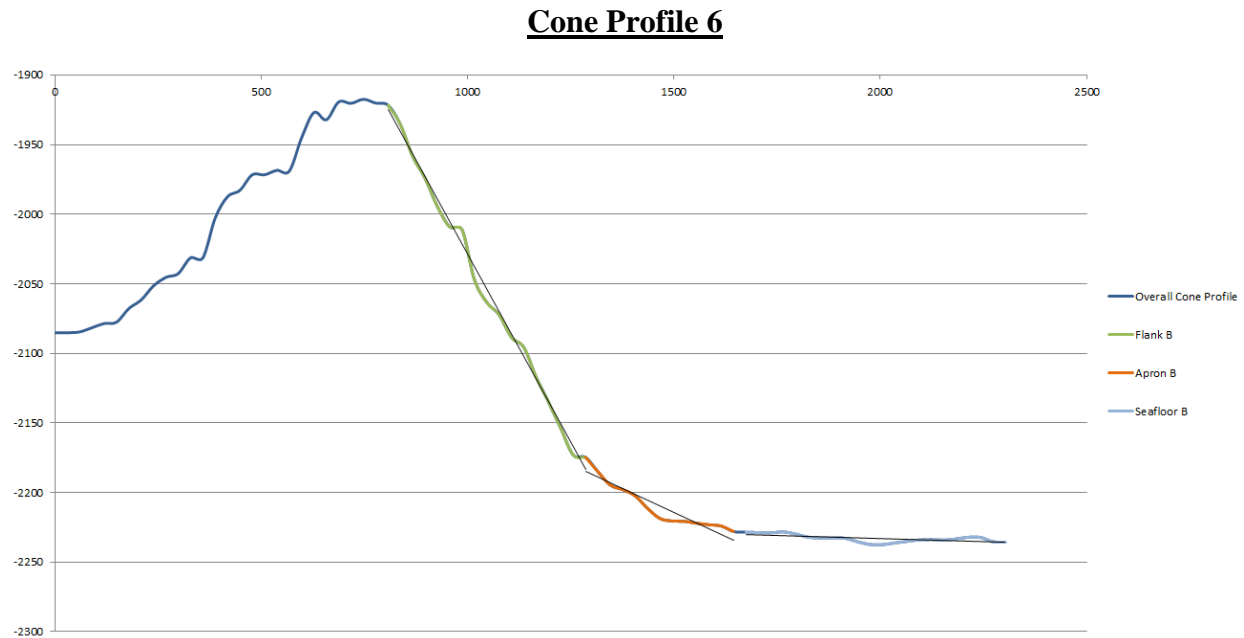


**Figure 15.** Profiles graphs of cones 6 and 7 created using Microsoft Excel with corresponding trend lines for each slope portion. Those labeled A represent eastern slopes and B represent western slopes.

### ***Charting of Cones and Determination of Ellipsoidal Shape***

With known averages for the cone flanks, aprons and seafloor, a delineation of the cone bases was made using a gradient color scale in ArcGIS. The utilization of a gradient color scale allows for the break in slope between the flank and the apron to be visualized on the maps. The

gradient color scale used contains colors divided to represent certain values of percent slope rise, with the cooler colors, greens and blues, representing low percent rise and the warmer colors, reds and oranges, representing areas of high percent rise. Based on the slope analysis, the transition from flank to apron is designated by the transition from green to yellow.

A new cone base shapefile was created in ArcCatalog to represent the cone bases as polygons created in ArcMap. Each polygon was created using the polygon construction tool to create a cone base shapefile. The next step required finding the center point for each polygon. This was done by adding fields for X and Y coordinates to the attribute table of the cone base shapefile. Using the EasyCalculate tool in ArcMap, the X and Y coordinate locations in meters were populated for the respective attribute fields. The meter coordinates were then converted by adding new fields of latitude and longitude to the cone base attribute table. Using the Calculate Geometry tool within the attribute table, the properties were converted from X and Y meter coordinates to the corresponding decimal degrees for latitude and longitude by referencing the WGS 1984 Antarctic Polar Stereographic coordinate system. The attribute table was then exported as a text (.txt) file. Microsoft Excel was used to edit the exported text file to include the feature ID, latitude and longitude attributes and then converted to a delimited CSV (.csv) file. By accessing the .csv file in the ArcCatalog tab of ArcMap, a Create Feature Class from XY Table tool was utilized by importing the data from the edited excel file to be converted to a center point shape file. The center point shape file was then added to Arc Map for visual representation.

All following data were generated by utilizing the Create Features tool within the Editor toolbox. The shape files for ellipses, rectangles, long axis and short axis were created in the same manner as the cone base polygon shape file, with the exception that any line-based shape file used a polyline form and a line construction tool for generation. A best fit ellipse or circle was



generated for each cone from the newly created center points. After the completion of the ellipses and circles, each ellipse or circle was bounded by a rectangle or square. The bounding rectangle or square aided in the addition of the short and long axis to each ellipse or circle; the rectangle and the vertex of the ellipse give a greater accuracy for axis positions and lengths.

### ***Cone Alignment and Selection of Reliability***

The determination for quality and reliability of the alignment of volcanic cones within the research area was done using the Paulsen and Wilson [2010] method as described in Table 2. The method uses a graded system from A to D with an A representing the most reliable grade. As seen in Table 2 there are five criteria which go into determining the reliability grade. The criteria are as follows: Number of vents per alignment, standard deviation of the vent centers from the best fit line, vent elongation index (includes the number of elongate vents and the ratio of long axis to short axis of those vents), standard angular deviation of vent long axis as compared to vent alignment and average vent spacing distance along the alignment (Figure 16). By grading the cone alignments using these criteria, the confidence in each lineation can be determined. A high level of confidence implies that the volcanic alignment can be used to map crustal stresses.

**Table 2.** System created to determine reliability of vent alignments. [Paulsen & Wilson 2010]

| Reliability grade | # vents | Standard deviation best-fit line distance (m) | Index of vent elongation   | Standard angular deviation vent long axes (°) | Average vent spacing distance (m)         |
|-------------------|---------|---|--|---|---|
| A                 | ≥4      | ≤125  | 1 cleft cone -or-<br>1 fissure ridge -or-<br>2 ≥ 1.6 -or-<br>1 ≥ 1.6 and 1 ≥ 1.4 | ≤30   | No limit                                  |
| B                 | ≥5      | ≤100  | No shape data  | No shape data                                 | ≤600 <sup>a</sup> or ≤800 <sup>b</sup>    |
|                   | ≥3      | ≤150  | 1 ≥ 1.6 -or-<br>2 ≥ 1.4 -or-<br>1 ≥ 1.5 and 2 ≥ 1.2                              | ≤35   | No limit                                  |
| C                 | ≥4      | ≤125  | No shape data  | No shape data                                 | ≤600 <sup>a</sup> or ≤800 <sup>b</sup>    |
|                   | ≥2      | ≤175  | 1 ≥ 1.4 -or-<br>2 ≥ 1.2  | ≤40   | No limit                                  |
| D                 | ≥3      | ≤150  | No shape data  | No shape data                                 | ≤800 <sup>a</sup> or ≤1000 <sup>b</sup>   |
|                   | ≥2      | > 175   | 1 ≥ 1.2  | > 40  | No limit                                  |
|                   | ≥3      | > 150   | No shape data  | No shape data                                 | > 800 <sup>a</sup> or > 1000 <sup>b</sup> |

A cone alignment polyline shape file was created in the same manner as previous shape files. Alignment lines were drawn using the editor tool. Each alignment created was tested using the criteria of the Paulsen and Wilson method. The cone elongation index was determined by computing the ratio of long axis to the short axis lines, with the length of the lines found using the Calculate Geometry tool. The azimuth of cone long axis and the cone alignments were created using the EasyCalculate tool in ArcMap. Distance between cones was found using the ArcMap measure tool. The resulting information from these measurements was used to determine the reliability of each cone alignment.

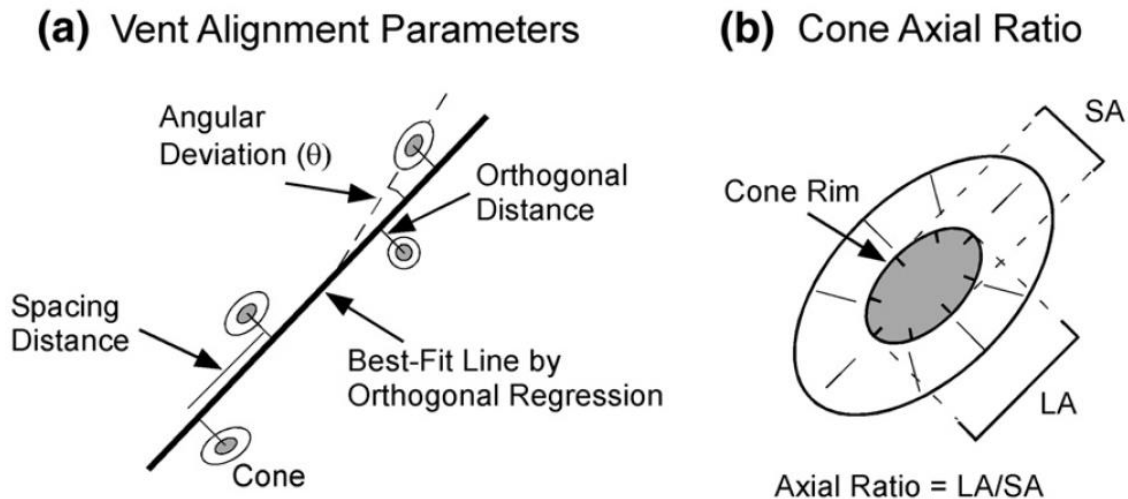


**Figure 16.** Attributes used for characterization and assessment of vent shapes and alignments. (a) The orthogonal distances of the vent center points from the best-fit line, the angular deviation of elongate vent long axes from the trend of the best-fit line, and the spacing distance between vents are used along with the types and numbers of elongate vents (i.e., the elongation index) to assess the reliability of individual alignments (Table 1). The best-fit line for an alignment is calculated by minimizing the orthogonal distances from points to the line (i.e. orthogonal linear regression). The angular deviation of fissure ridges, cleft cones, and elongate vents from the best-fit line is measured as the acute angle separating the long axis of the elongate vent and the best-fit line. Vent spacing distance is defined as the distance that separates adjacent vents found along the trace of the best-fit line. (b) The axial ratio of an elongate vent is the long axis length divided by the short axis length of the cone base. LA: long axis; SA: short axis [Modified from Paulson & Wilson 2010].

## **Results**

### ***Morphologic Provinces***

The use of the BBPI and FBPI was a great aid in the analysis of the volcanic ridge and associated cones (Figure 17). The BBPI image aided in showing other large features associated with the ridge such as the boundaries between low- and high-resolution data areas and the deep basin features that flank the left and right sides of the ridge. The moat represents a depression that may be due to crustal flexure caused by the weight of the ridge itself. The image generated from the FBPI was helpful in determining cone base polygon boundaries for cones that were connected with the ridge and each other.

Morphologic analysis of the bathymetric data shows that the regional volcanic ridge has a depth below sea level ranging from roughly 1300 meters near the continental shelf at the southern end to 2025 meters at the northern end of the ridge. The surrounding seafloor has a depth of 1725 meters in the south near the shelf, becoming deeper northward and reaching an average depth of approximately 2300 meters. The maximum width of the ridge is 5570 meters and the total ridge length is 19600 meters. The rise of the ridge above the seafloor becomes larger as you follow the ridge north, with the southern tip having a maximum rise of 378 meters and increasing to a maximum rise of 950 meters to the north. The top of the ridge is defined by individual cones with conical peaks and no observed craters (Figures 18, 19 and 20).

The moat-like basins that flank the ridge have a depth of 46 meters (east) and 44 meters (west) below the average seafloor surrounding them (Figure 17). The eastern basin reaches 3956 meters in width and extends 20,743 meters along the eastern flank of the ridge. The western



basin has a width of 3759 meters and a length of only 5962 meters, although there are data gaps obscuring the full extent of this region.

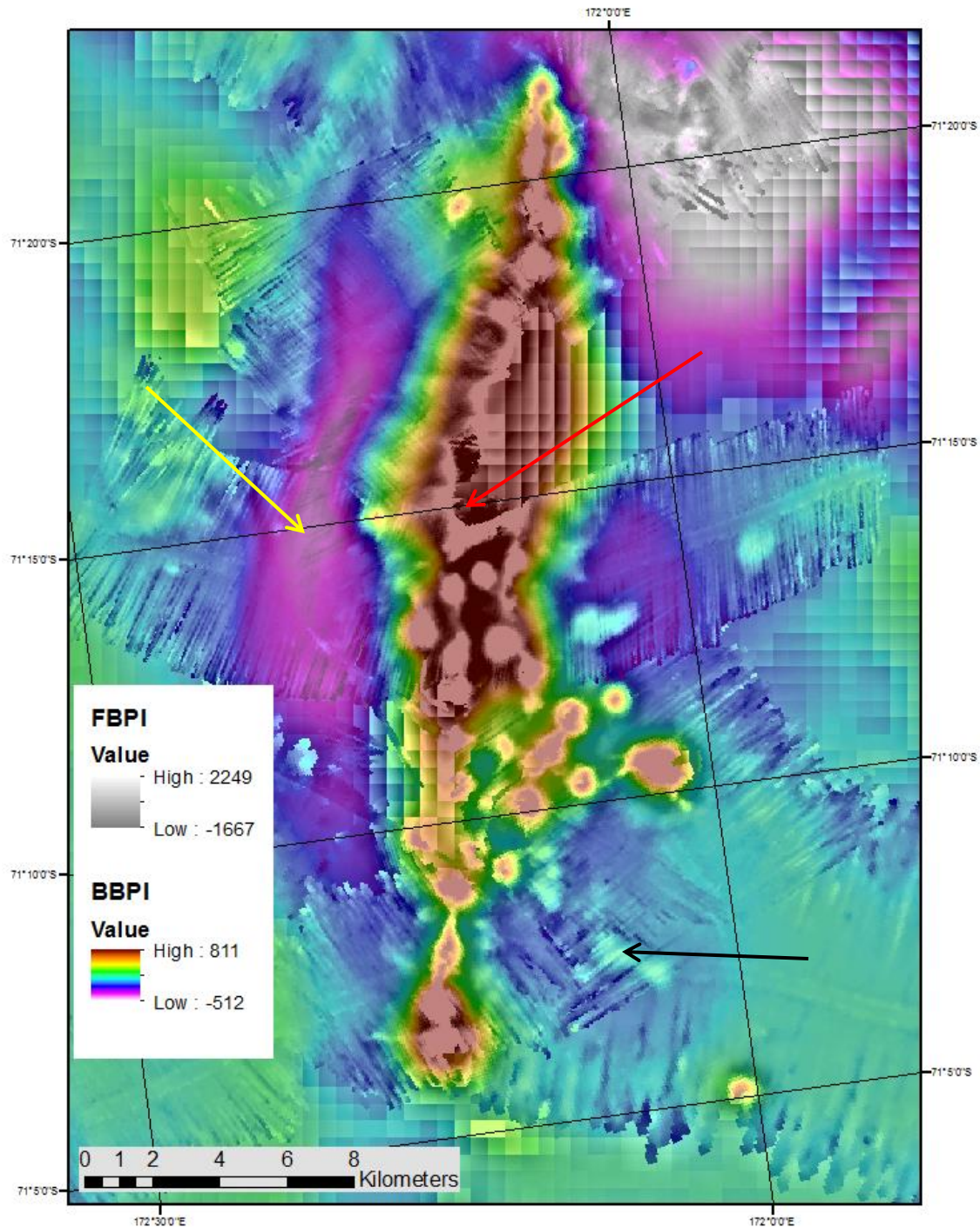


**Figure 17.** The BBPI-FBPI overlay shows the moat like depressions (yellow arrow), features with low slopes (black arrow) and boundaries between high and lower resolution data (red arrow).

### ***Ridge and Vent Morphology***

Although the volcanic ridge appears to be a straight, NE-SW trending feature when viewed on regional-scale maps, this analysis of the ridge revealed four individual ridge segments. The segments are well defined and have trends of  $195^{\circ}$ ,  $188^{\circ}$ ,  $204^{\circ}$  and  $188^{\circ}$ , from north to south (Figure 18). The average trend of  $194^{\circ}$  was used to compare ridge and cone alignments.

A total of 31 individual volcanic cone seamounts were mapped and analyzed in this study. Possible cones that were poorly covered by higher resolution bathymetry data (<50%) were omitted from this analysis. Cones are characterized by conical shapes and peaks with no visible craters (Figures 19–21). The average height of the cones above the seafloor is 542 meters with an average long dimension of 1571 meters. Analysis of individual cones allowed calculation of the maximum and minimum slopes for the flank, apron and seafloor (Table 4). The minimum and maximum angles are  $16.7^{\circ}$  and  $34.4^{\circ}$  (east flank),  $18.55^{\circ}$  and  $32.17^{\circ}$  (west flank),  $4.5^{\circ}$  and  $16.7^{\circ}$  (east apron),  $5.08^{\circ}$  and  $15.05^{\circ}$  (west apron),  $0.71^{\circ}$  and  $4.27^{\circ}$  (east seafloor) and  $0.01^{\circ}$  and  $4.78^{\circ}$  (west seafloor). Average flank slopes are between  $24.81^{\circ}$  and  $25.08^{\circ}$ , apron slopes average between  $10.12^{\circ}$  and  $10.17^{\circ}$  and the seafloor slope averages between  $1.28^{\circ}$  and  $2.09^{\circ}$  (Table 4). A map of slopes of volcanic seamounts, depicted as percent rise, is shown in Figure 20.

### ***Cone Elongations and Vent Alignments***

The shapes of the cones mapped from the slope and FBPI maps are shown in Figure 23. Of the 31 cones analyzed, 15 have an elongation ratio of the long axis to the short axis of less than 1.2, with 6 cones having a circular shape with ratio of 1.0 (Figure 24). The maximum

elongation ratio is 1.72 (Table 4). The trends of the cones range between  $111^{\circ}$  and  $242^{\circ}$  with a  $177^{\circ}$  average azimuth (Figure 25).

Nine cone alignments were defined through the analysis of the volcanic cones (Figure 27). There is an average of 2–3 elongate cones per alignment. The cone alignments have orientations ranging from  $128^{\circ}$  to  $209^{\circ}$  with an average azimuth of  $174^{\circ}$  (Figure 24). Evaluation of the cone alignments using the Paulsen and Wilson [2010] method resulted in two alignments receiving a grade of B, 4 alignments receiving a grade of C and 3 alignments receiving a grade of D (Table 4). Of the 9 cone alignments, 6 are oriented within  $\pm 15^{\circ}$  of the ridge alignment average (Figure 28).

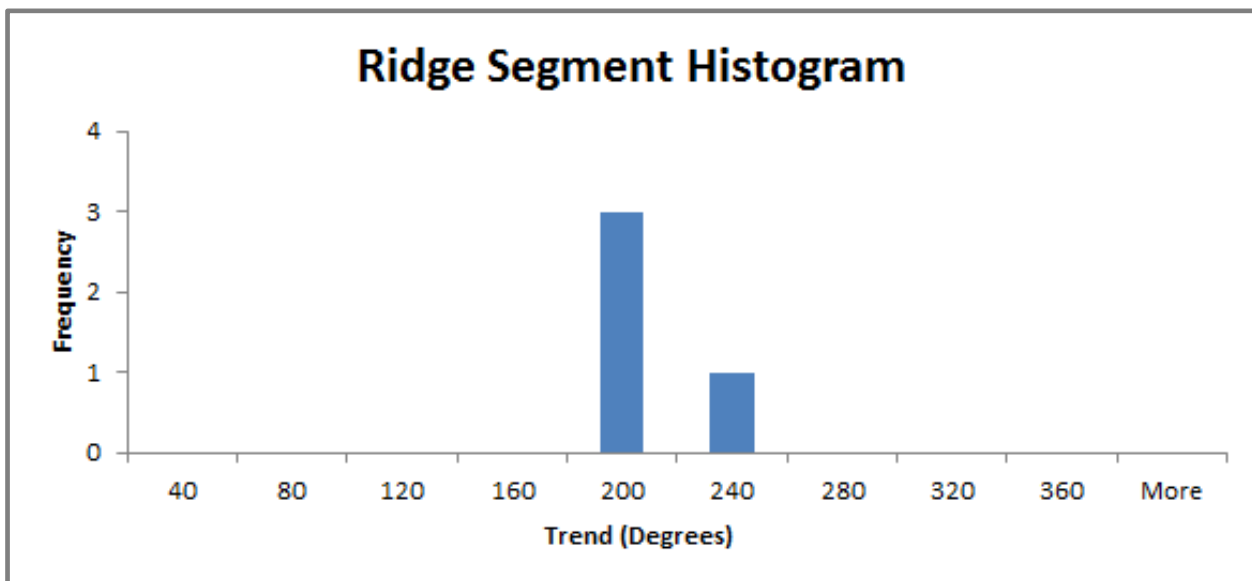


**Figure 18.** Histogram of ridge segment trends.

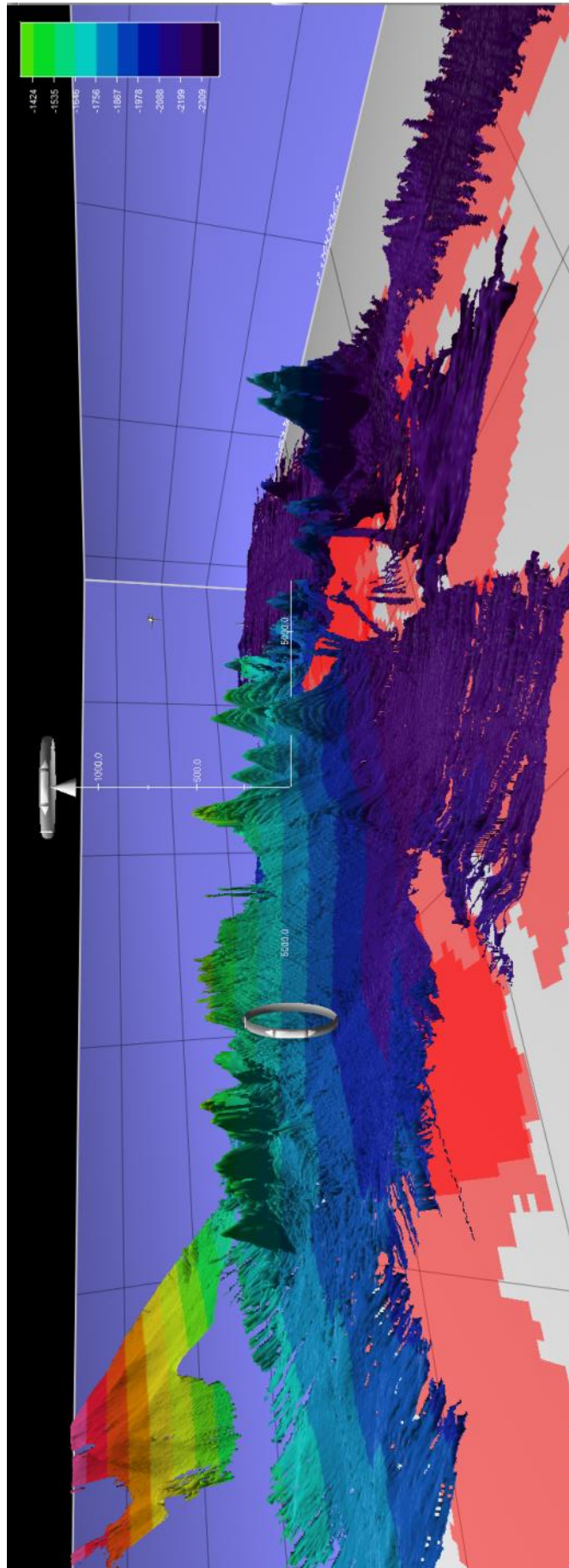
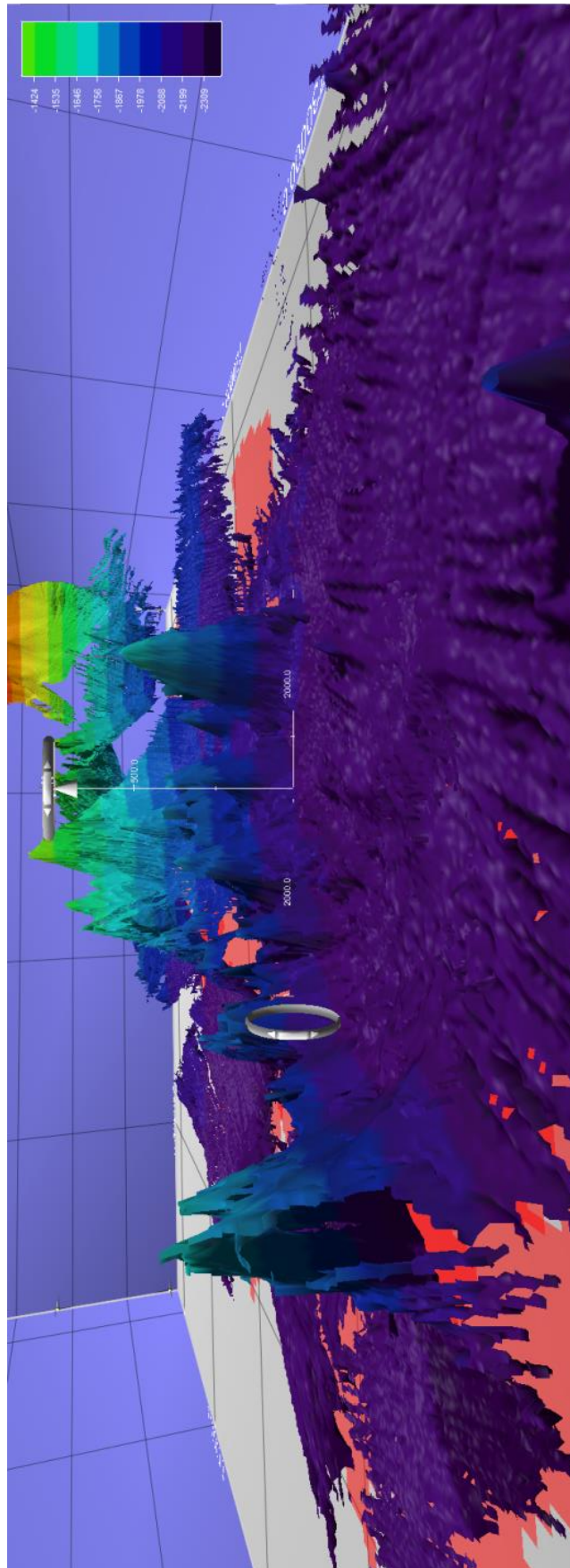
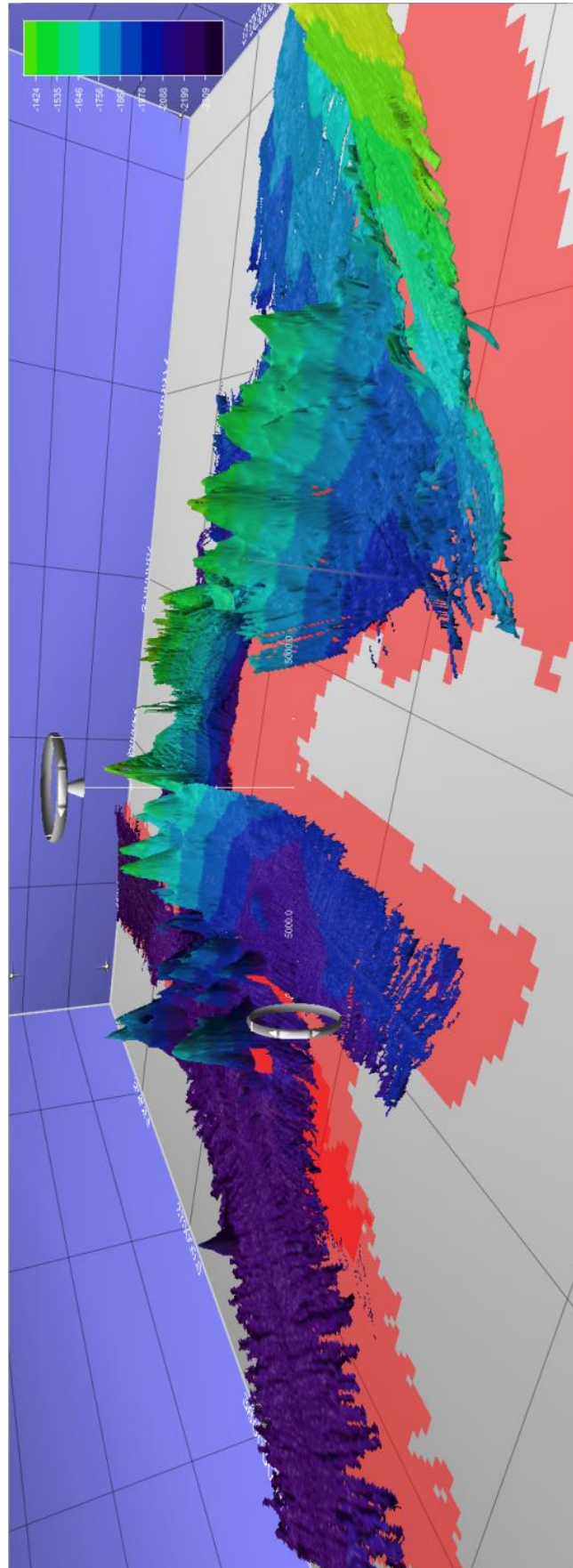


Figure 19. View of ridge from the east in Fledermaus.





**Figure 20.** Fledermaus view of ridge from the north.



**Figure 21.** Fledermaus view of the ridge from the west-southwest.

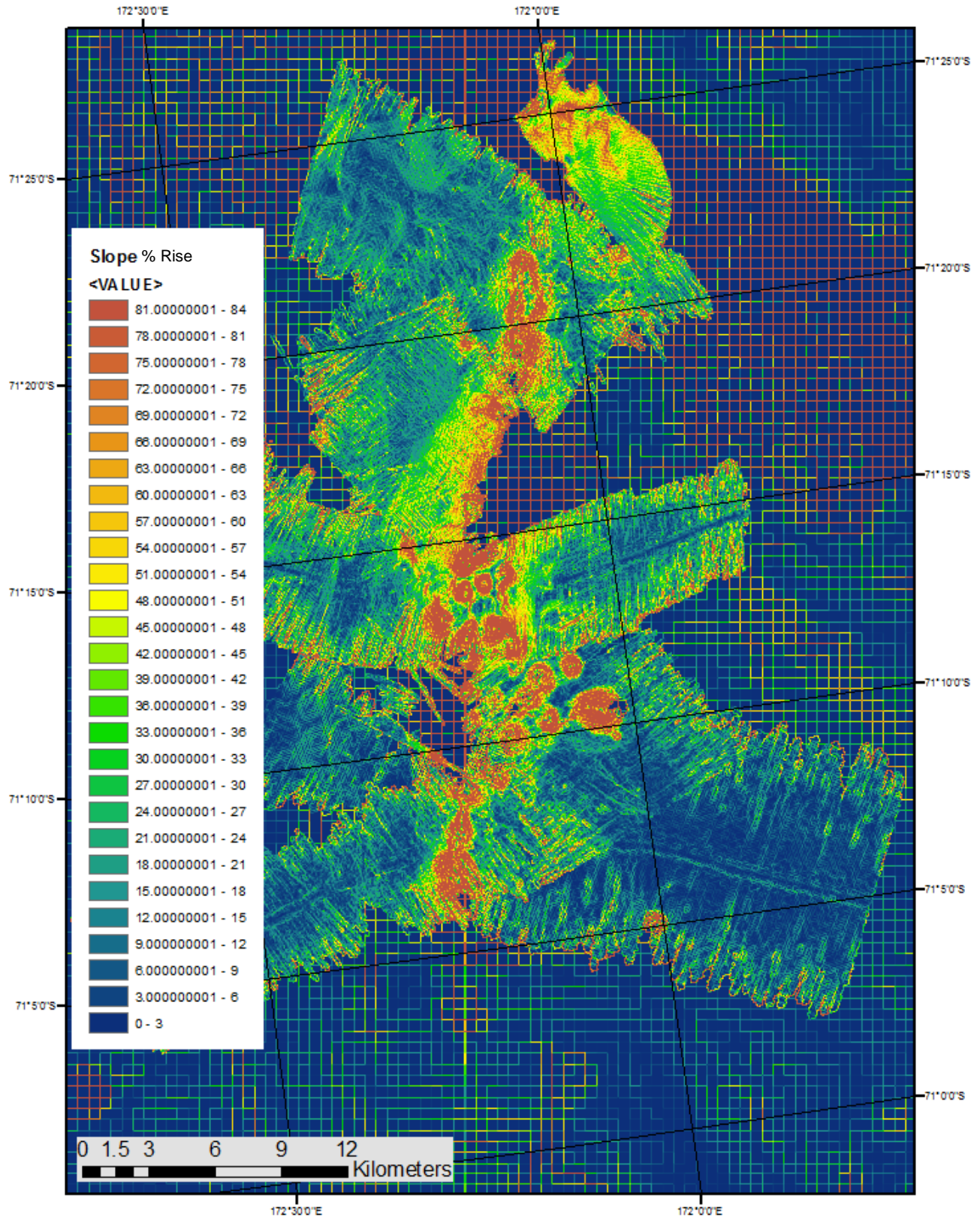
**Table 3.** Average rise/run data and average slope from the cone profile analysis.

|                                      | <u><b>Seafloor A (East)</b></u> | <u><b>Apron A</b></u> | <u><b>Flank A</b></u> |
|--------------------------------------|---------------------------------|-----------------------|-----------------------|
| <u><b>Average Rise/Run</b></u>       | 0.03647                         | 0.17937               | 0.4680                |
| <u><b>Average Degree</b></u>         | 2.089                           | 10.169                | 25.079                |
| <u><b>Average Degree Rounded</b></u> | 2.09                            | 10.17                 | 25.08                 |

|                                      | <u><b>Seafloor B (West)</b></u> | <u><b>Apron B</b></u> | <u><b>Flank B</b></u> |
|--------------------------------------|---------------------------------|-----------------------|-----------------------|
| <u><b>Average Rise/Run</b></u>       | 0.02247                         | 0.17844               | 0.46227               |
| <u><b>Average Degree</b></u>         | 1.287                           | 10.117                | 24.810                |
| <u><b>Average Degree Rounded</b></u> | 1.29                            | 10.12                 | 24.81                 |





**Figure 22.** A percent change in slope map developed to highlight the steep slopes of the cone flanks (% rise >46) to delimit the shape of the cone bases.



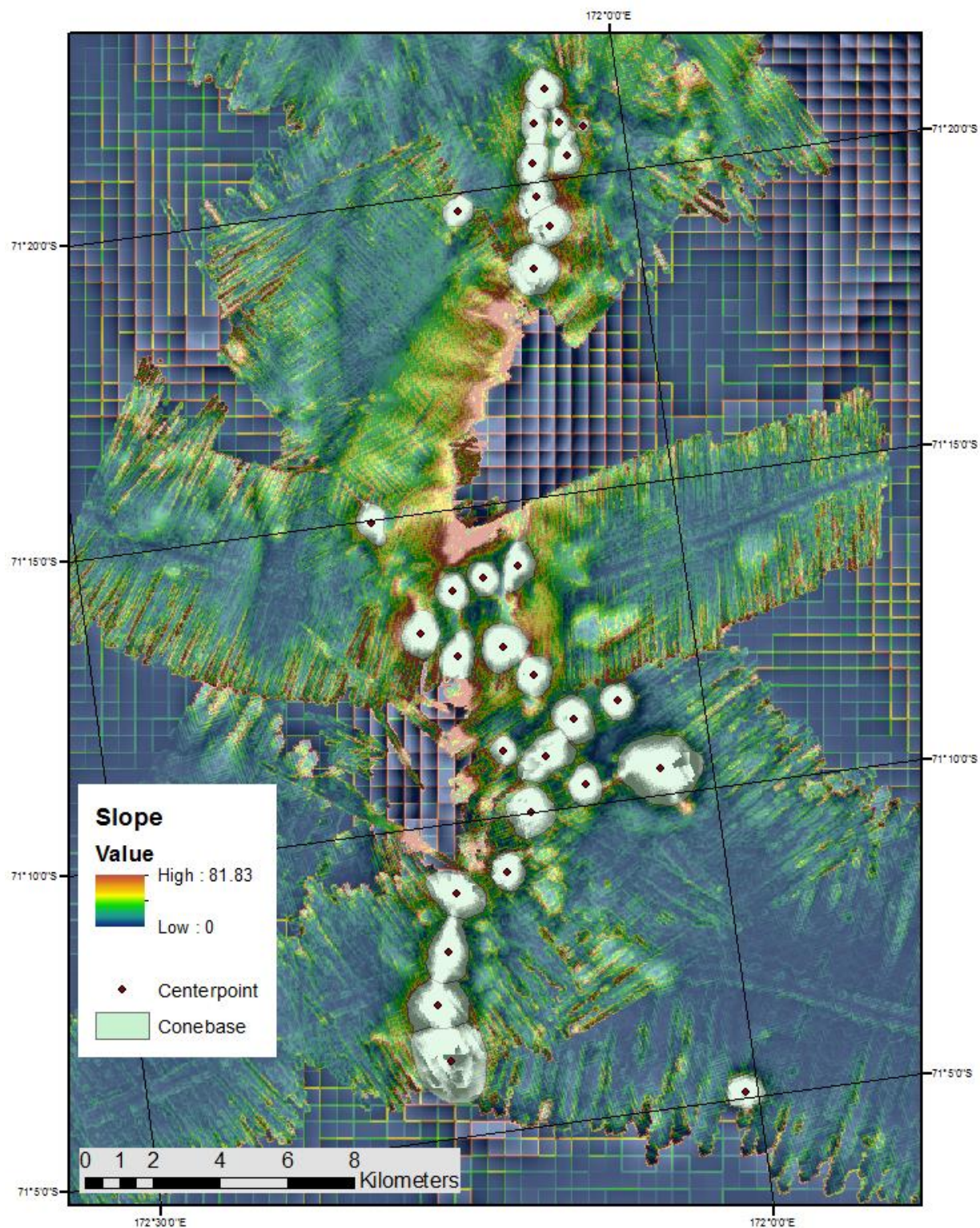


**Figure 23.** Polygons outlining the base of each volcanic cone, and their corresponding center points.

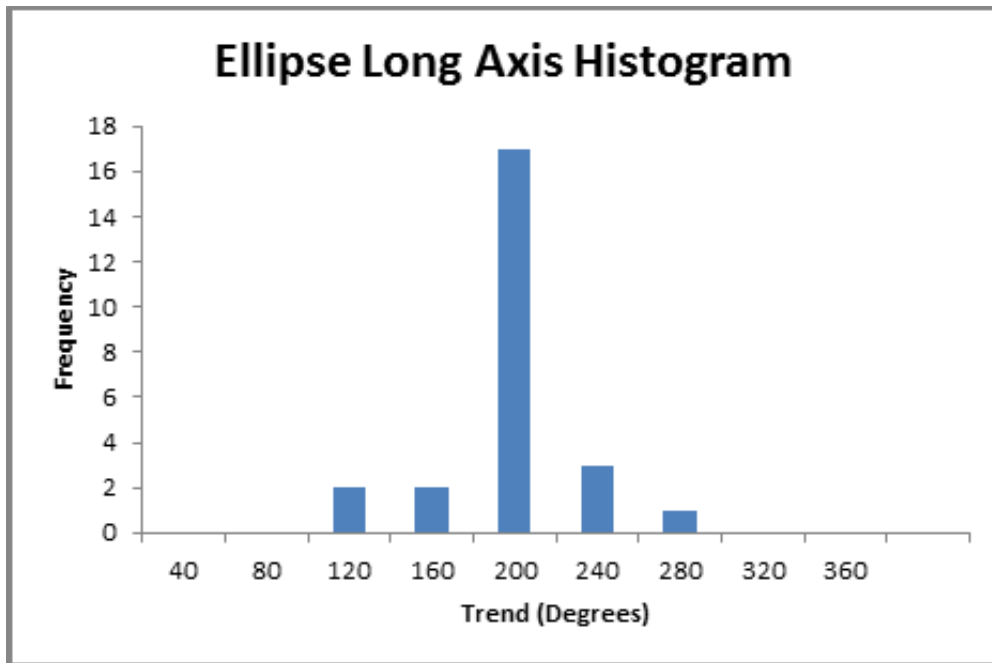


**Figure 24.** Cone long axis trend histogram

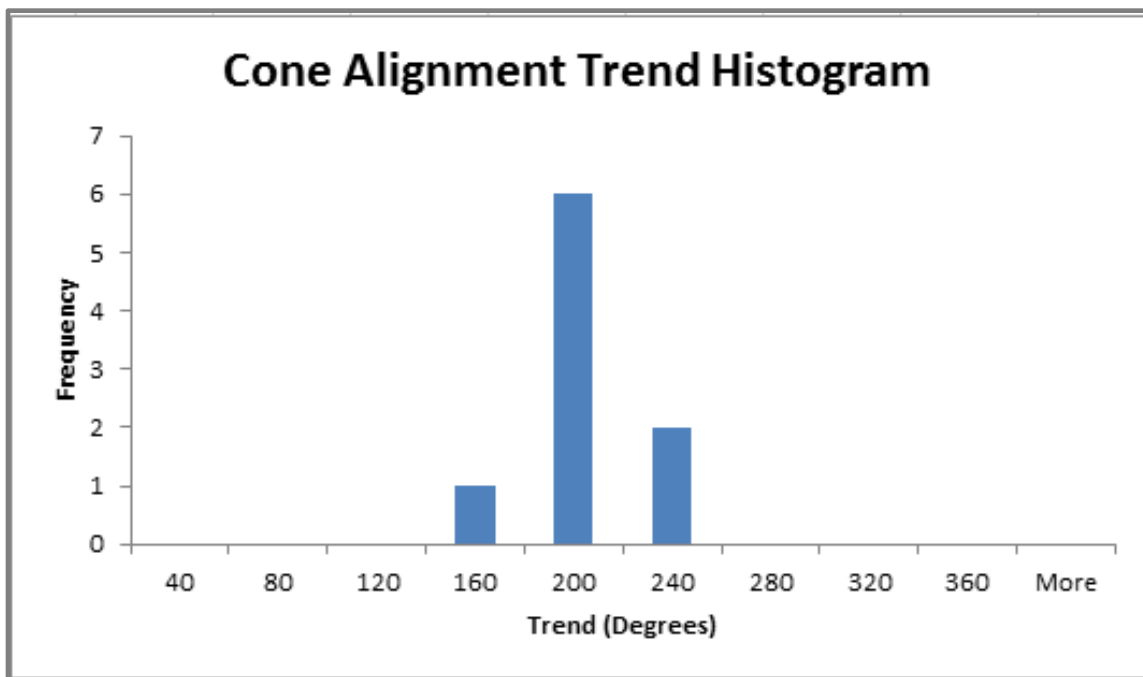


**Figure 25.** Histogram of cone alignment trends.

**Table 4.** Alignment confidence criteria were applied to the nine cone alignments along the ridge. The criteria analyzed were cone (vent) number, angle of deviation, and elongation index. The criteria for distance between cones were omitted from the chart due to all alignments having a “no limit” designation.

| <u>Alignment</u> | <u>Number of<br/>Cones</u> | <u>Alignment Azimuth<br/>(Degrees)</u> | <u>Cone(s) Azimuth<br/>(Degrees)</u> | <u>Elongation Index<br/>(LA:SA)</u> | <u>Largest Angle of<br/>Deviation (Degrees)</u> | <u>Grade</u> |
|------------------|----------------------------|--|--------------------------------------|-------------------------------------|---|--------------|
| 1                | 2                          | 190                                    | 191, 188                             | 1.72, 1.07                          | 2   | C            |
| 2                | 2                          | 202                                    | 146, 200                             | 1.6, 1.18                           | 46  | D            |
| 3                | 2                          | 157                                    | 164, 182                             | 1.15, 1.31                          | 25  | D            |
| 4                | 2                          | 159                                    | 181, 170                             | 1.7, 1.72                           | 22  | C            |
| 5                | 4                          | 176                                    | 184, 206, 176, 178                   | 1.57, 1.24, 1.4, 1.01               | 30  | B            |
| 6                | 2                          | 199                                    | 156, 235                             | 1.17, 1.6                           | 43  | D            |
| 7                | 3                          | 180                                    | 190, 191, 157                        | 1.18, 1.63, 1.4                     | 23  | B            |
| 8                | 2                          | 121                                    | 104, 151                             | 1.20, 1.34                          | 30  | C            |
| 9                | 2                          | 180                                    | 183, 200                             | 1.15, 1.55                          | 20  | C            |



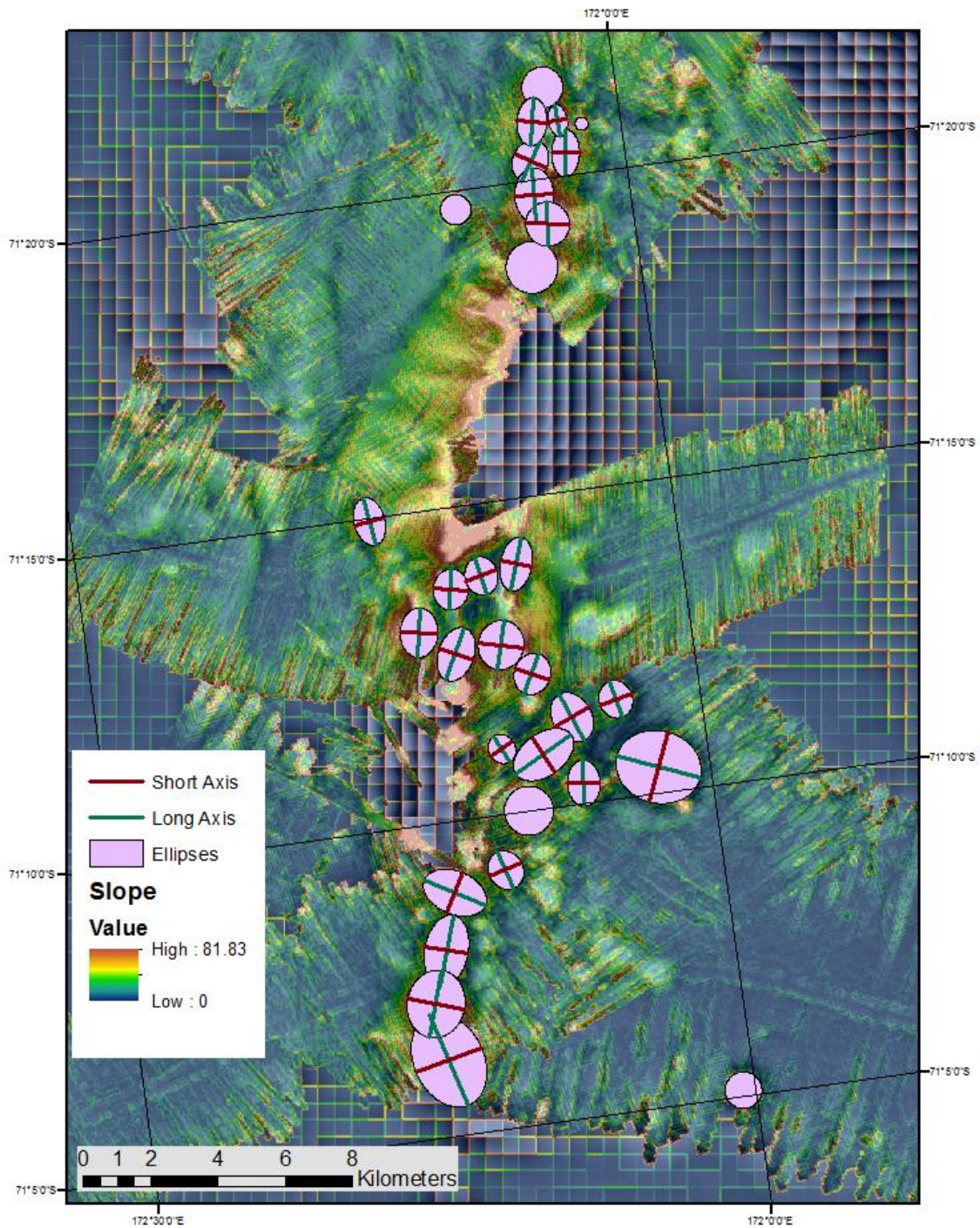


**Figure 26.** Circles or ellipses, with their respective long and short axes, fitted to each mapped volcanic cone.



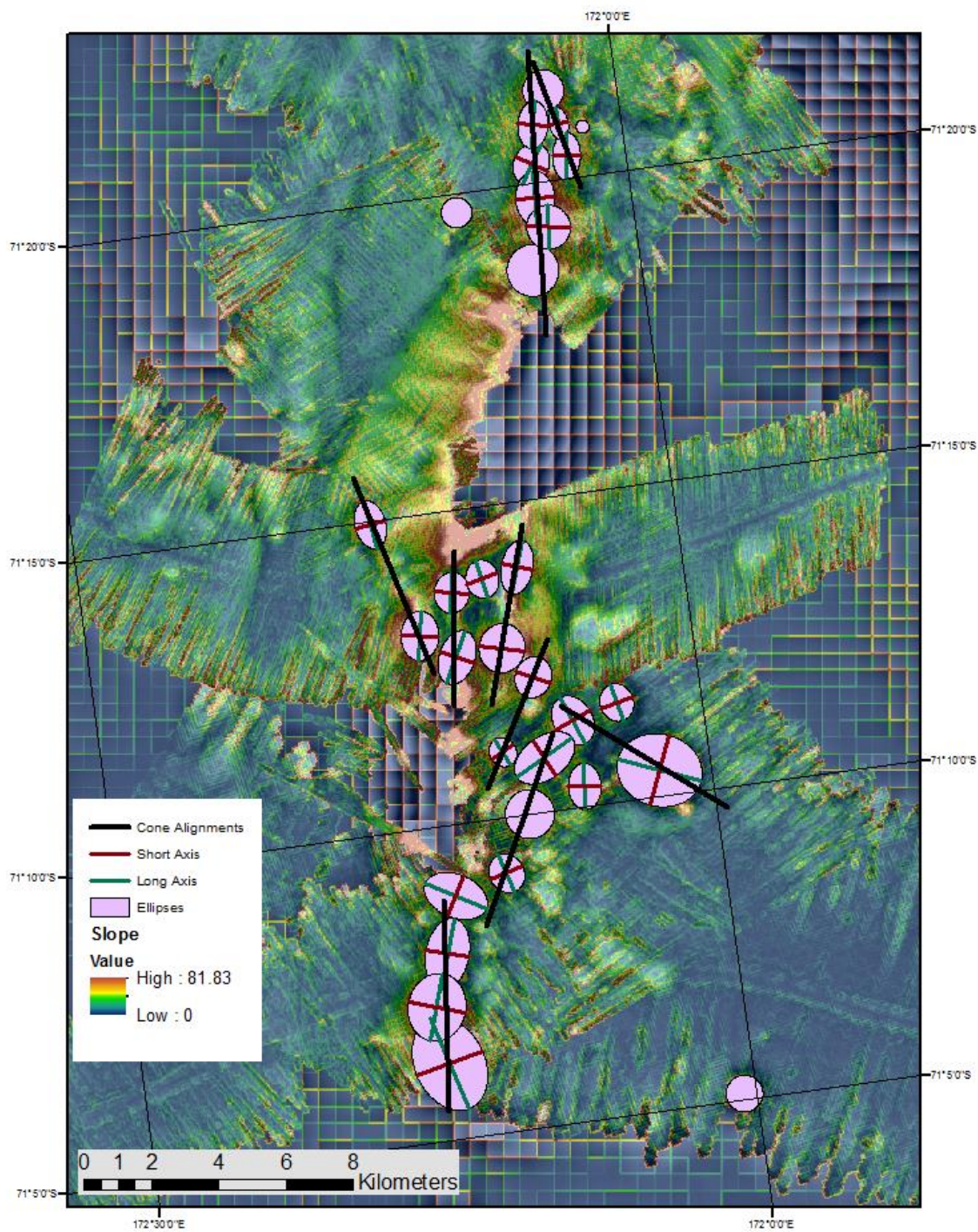


**Figure 27.** Cone alignments represented by the black lines.



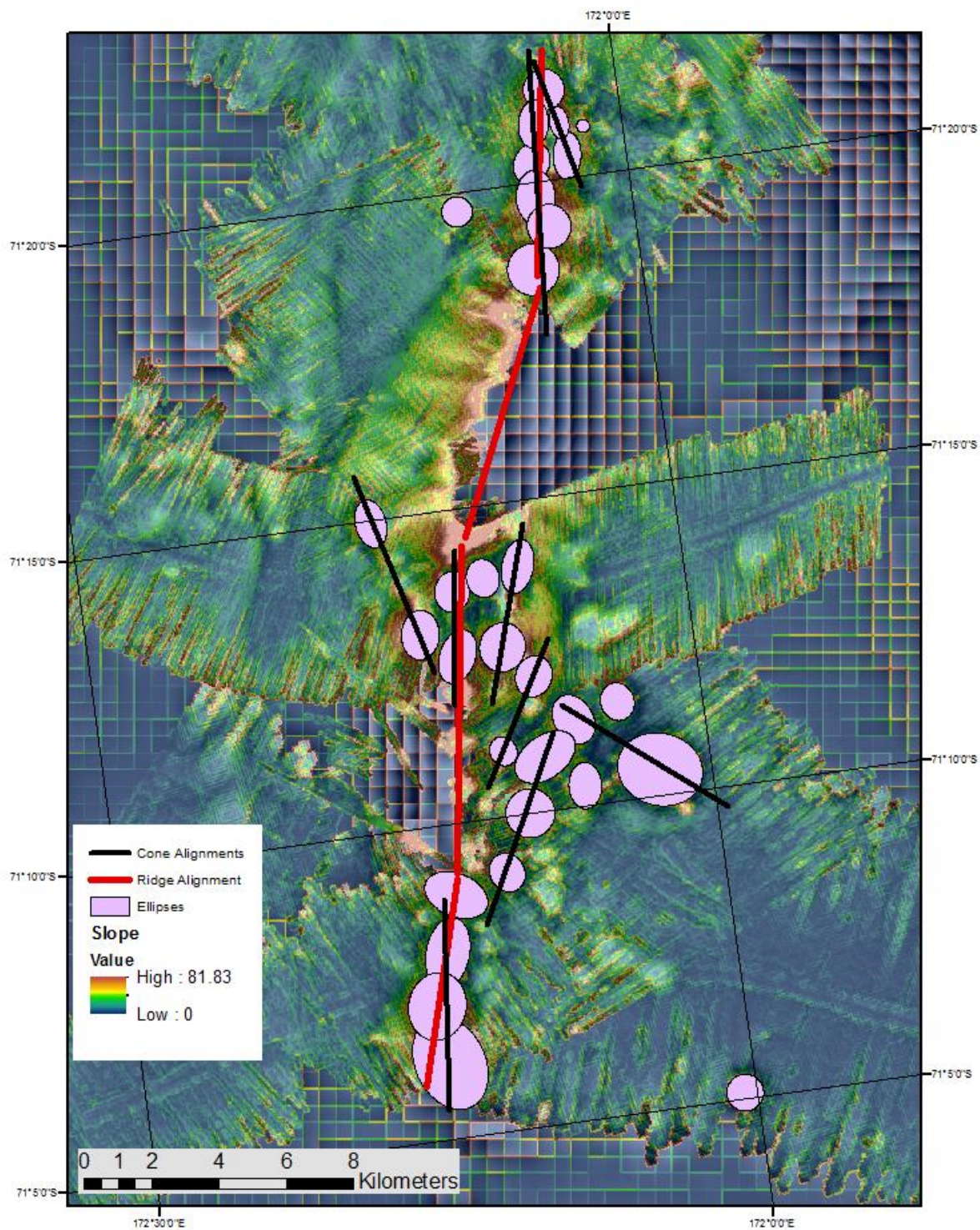


**Figure 28.** Alignments of cones (black) compared with ridge segments (red).

## **Discussion**

### ***Mapping Seafloor Terrain and Vent Alignments***

The Benthic Terrain Modeler tool (BTM) is an ArcGIS add-on that I discovered through background research. The use of the BTM to generate the BBPI and FBPI is a new method unused in previous Adare Basin research, which proved valuable in the analysis of seafloor terrain. The BBPI gave a better overall picture of the region, revealing large-scale bathymetric features such as the width and trend of the volcanic ridge as a whole and the flanking basins that border it, compared with hillshade and slope maps. The FBPI enhanced the identification of individual cones. The ability to overlay the FBPI at a 50% transparency onto other images helped to visualize individual cones superposed on the ridge. This allowed for better understanding of how the ridge influenced some of the cone slopes.

Two cone alignments yielded confidence grades of B, but most alignments yielded grades of C or lower because of the small number of cones defining the alignments. These confidence grades could indicate that the method of Paulsen and Wilson [2010], designed for terrestrial and monogenetic cinder cones, may need to be altered in order to analyze submarine volcanoes and ridges to represent the size of such features more accurately. The fairly large gaps in the high-resolution bathymetry data, primarily along one half of the dominant ridge feature and in the northern ridge section, limited the number of cones that could be clearly mapped and influenced the alignment analysis.

### ***Volcanic Ridge and Alignment Trends Relative to Regional Rift Structure***

The overall trend of the ridge shows a NE-SW orientation but, in detail, is defined by four individual segments. The four ridge segments maintain a NE-SW trend, similar to the ridge,



with a maximum difference of  $16^\circ$  from the ridge trend. Six of the nine volcanic alignments also have a NE-SW trend within  $15^\circ$  of the overall ridge trend. Volcanic alignments have orientations that parallel the ridge segments with which they are associated in several cases. Ridge section 1 and cone alignment 1, ridge section 2 and cone alignment 6, and ridge section 4 and cone alignment 8 all display a parallel relation between ridge and cone alignment trends (Figure 29). The cone alignments numbered 2, 4 and 5 show an en echelon pattern in a zone that parallels ridge segment 2 (Figure 30). Cone alignments 3 and 4 have NW-SE trends, at high angles to the ridge and the other vent alignments. The analysis of the orientation of the trends of the long axes of elongate cones shows that 20 of the 25 elongate cones have a NE-SW trend parallel to that of the cone alignments and ridges.

The dominant parallel nature of the ridge, vent alignments and cone long axes indicates that orientations of these features could have been controlled by a crustal stress field with a maximum stress ( $S_{Hmax}$ ) in the NE-SW direction and a minimum stress ( $S_{Hmin}$ ) in the NW-SE direction. There are two important exceptions to this simple interpretation.

Five elongate cones with NW-SE long axes, interpreted to define two cone alignments with the same trend, could not have formed in this stress field. Either they formed at a different time, in a stress field with  $S_{Hmax}$  oriented NW-SE and  $S_{Hmin}$  oriented in the NE-SW direction, or they formed by intrusion along pre-existing planes of weakness in the crust. Mapping by Granot et al. (2010) shows that faults curve to NNW trends, but does not show any NW-SE structures. Alignment 3 has a grade of D and may not be reliable as a crustal stress indicator. Alignment 7 has a B grade, but is closer to parallel to the average ridge and alignment trends. Given these factors, it is likely that only one stress regime was present during the volcanism that formed the ridge and cones.

The en echelon arrangement of alignments 2, 4 and 5 also suggests a variation in the stress regime. These vent alignments occur where the volcanic ridge becomes much wider. The en echelon geometry of the opening-mode magmatic fissures inferred from the alignments could indicate a component of right-lateral shear (Figure 29). The shearing motion causes opening-mode fractures in the crust between the shear zone margins. The overall ridge feature has a rhombic shape with a wider central region and thinner extensions to the north and south. The wider segment and rhombic shape could be explained by right-lateral shear along a curved pre-existing fault trend as mapped by Granot et al. [2010] (Figure 31).

The overall trend of the volcanic ridge and vent alignments parallels the fault trends mapped by Granot et al. [2010] from seismic reflection data (Figures 31 and 32). The northern tip of the volcanic ridge overlaps with an east-dipping normal fault mapped by Granot et al. [2010]. These relations suggest that the magmatic fissure system reactivated pre-existing fault structures. The changing trends of the ridge segments and cone alignments follow a curved path similar to that of the mapped faults. I interpret the ridge to have formed above a main fissure by a string of cones that merged to form a continuous ridge with the NE-SW trend. The series of smaller, en echelon fissures associated with right-lateral shear may have formed later. The location of the en echelon pattern on the widest part of the ridge reinforces the idea that the ridge was formed by multiple fissures associated with shear stress reactivation. The presence of two NW-SE cone alignments indicates that there may be at least one fissure that is oriented in that direction.

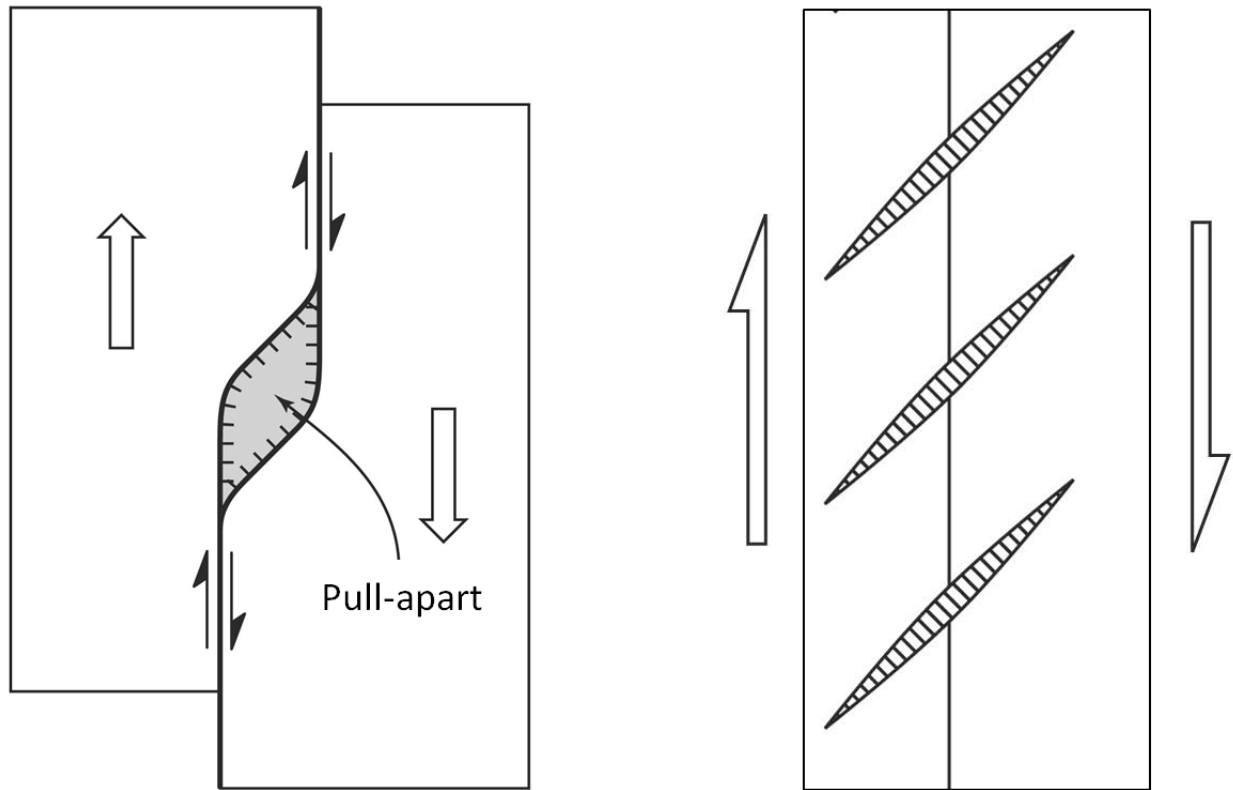


**Figure 29.** Opening mode fracture associated with shear stress and en echelon geometry at a shear boundary [van der Pluijm and Marshak 2004].

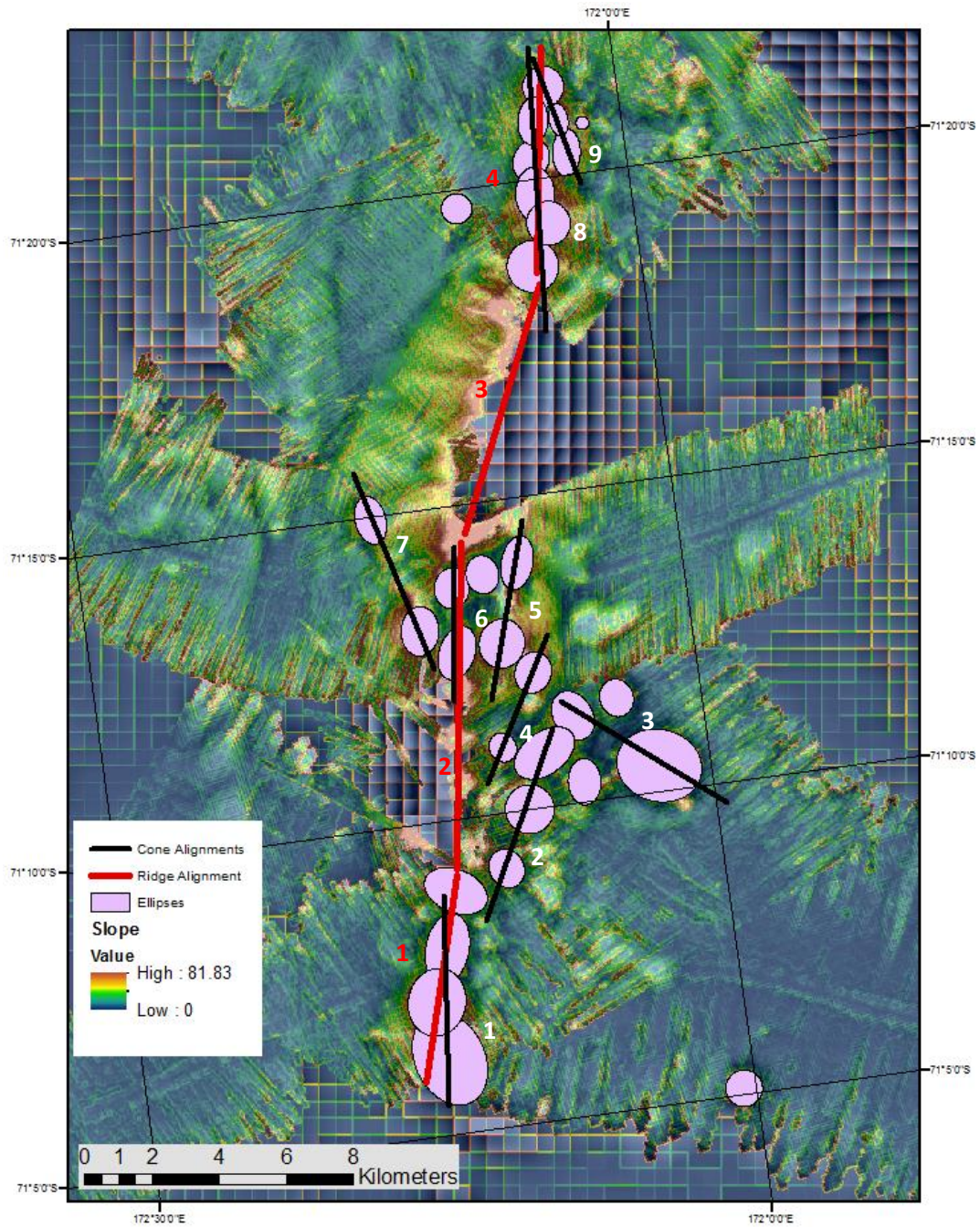


**Figure 30.** Numbered cone alignments and ridge segments.

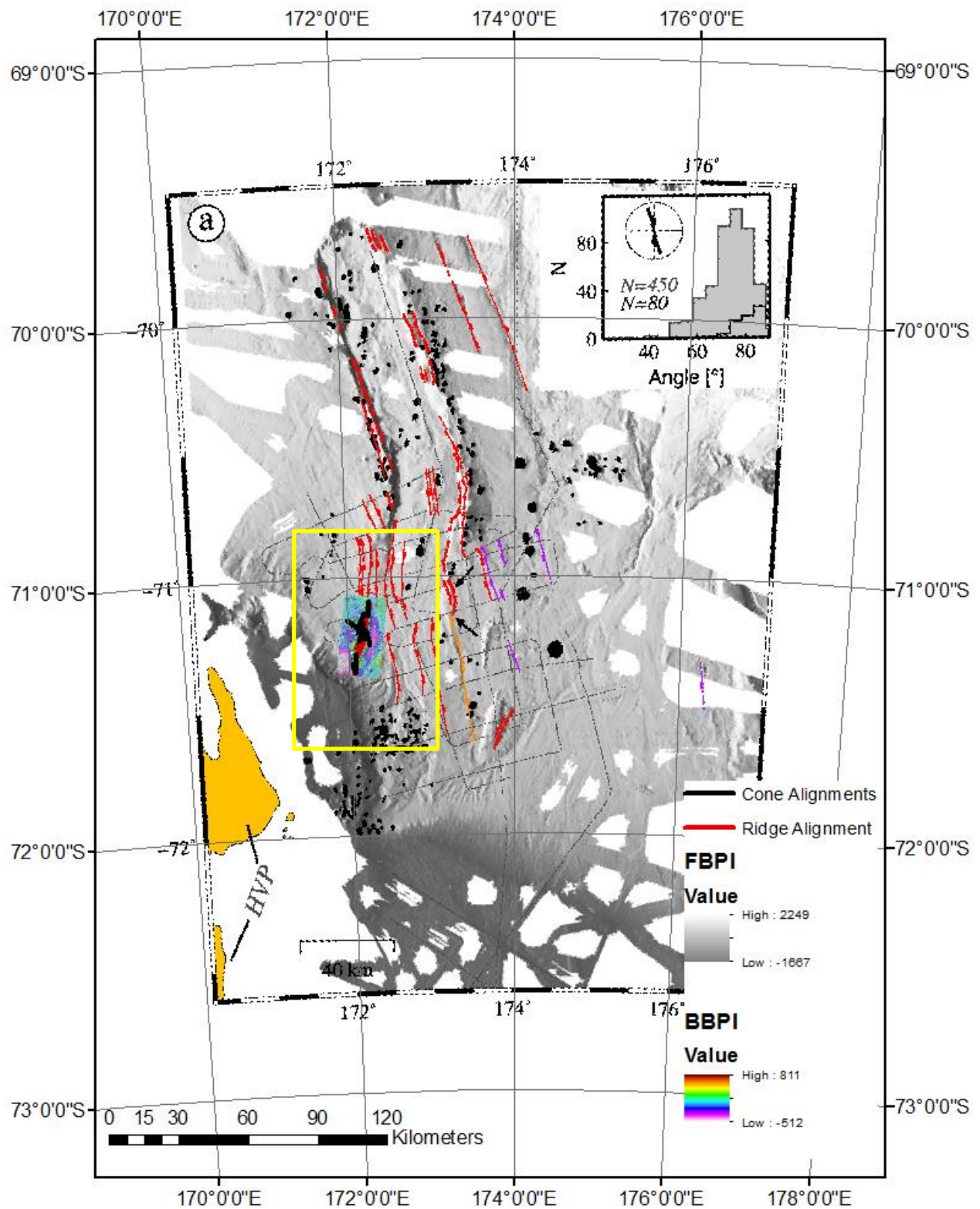


**Figure 31.** Geo-referenced overlay of ridge and vent alignments mapped in this study on fault map from Granot et al. [2010]. Figure 32 designated by the yellow box.



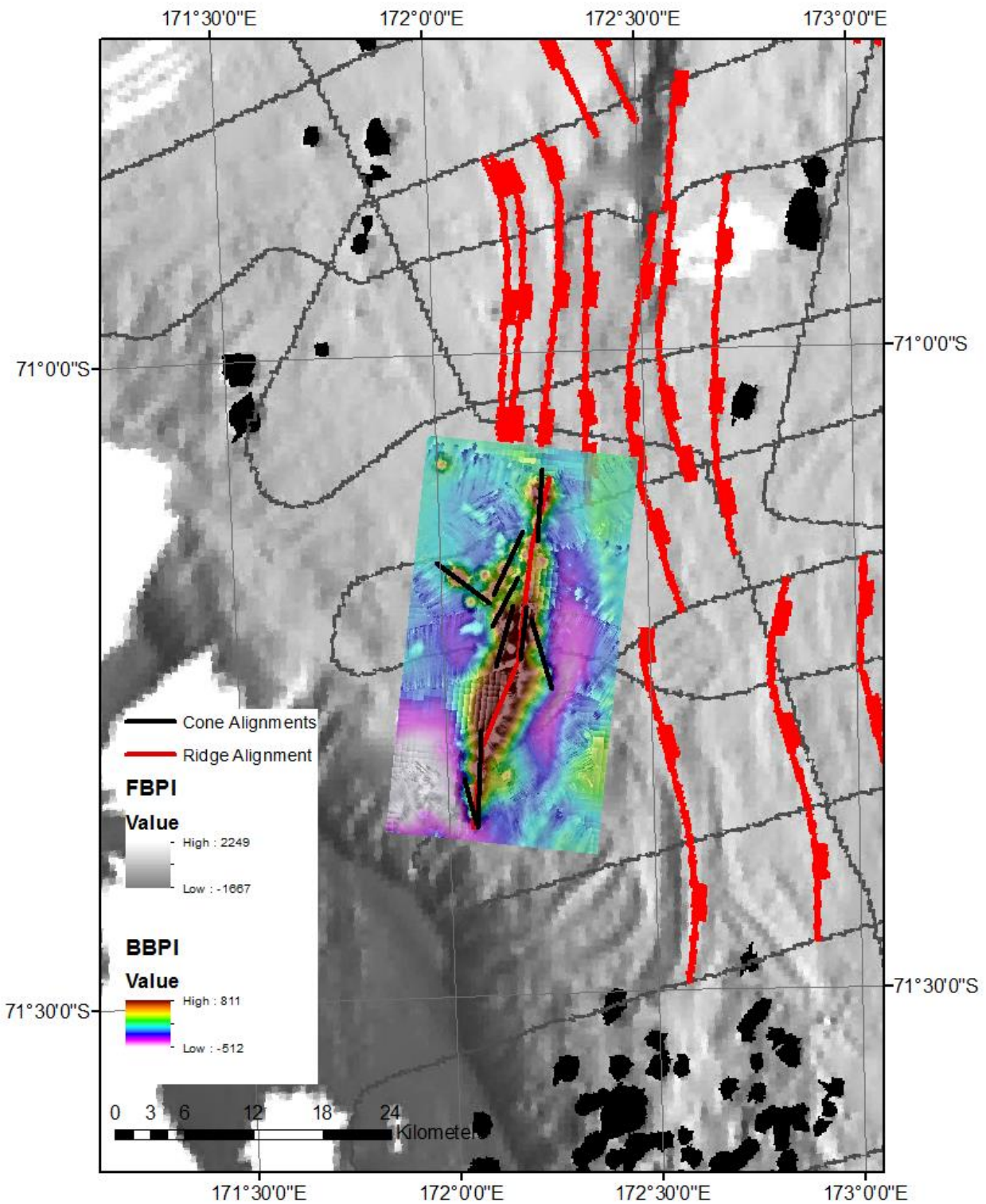


**Figure 32.** Geo-referenced BBPI-FBPI overlay of research area, cone alignment trends (black lines) and ridge trends (red lines) on fault map from Granot et al. [2010]

## **Conclusions**

The methods used in this research were developed by Paulsen and Wilson [2010] to study terrestrial volcanoes. The submarine ridge and cones examined in this study have larger dimensions than the terrestrial scoria cones, so the method is not scaled for this volcanic environment. The use of new bathymetric terrain analysis tools, the BBPI and FBPI, enhanced the visualization of both regional and local terrain features in the study area.

Four individual ridge segments were defined. The average length of the ridge segments is 7597 meters and they have an average azimuth of  $196^{\circ}$ . Nine cone alignment trends were defined and show a predominant NE-SW trend of  $170^{\circ}$  and an average length of 5758 meters. The long axes of 31 individual cones have an average azimuth of  $177^{\circ}$  and an average length of 1571 meters. The NE-SW trend of the ridge, the associated volcanic cone alignments and the individual elongated volcanic cones indicate a maximum horizontal stress in the NE-SW direction and a NW-SE minimum horizontal stress. Lack of dating on the volcanic rocks makes it difficult to relate the volcanic ridge formation to specific stages of the Adare Basin and Trough evolution. However faults mapped by Granot et al. [2010], assigned to a 16–17 Ma rifting event, are oriented parallel to the ridge. It is likely that magmatism utilized the pre-existing rift faults as conduits to the surface.

## **Suggestions for Future Research**

A study of the ages of the seafloor volcanic rocks through dredging and isotopic age dating would reveal a clearer picture of their time of formation, and provide insight into the association with the structural evolution of the region. A more detailed look at cones of low profile and those with only partial high resolution data coverage could increase the reliability of

the vent alignment analysis. A study of the moat-like features through wavelength analysis of the ridge and flanking basins could verify if the basins formed due to crustal flexure from the weight of the volcanic ridge. A comparison of the vent alignment trends from this study and those mapped by Rosenbeck [2013] and Barr [2014] could reveal the regional stress patterns in the Adare Basin region. A further comparison between these studies of cone shape and dimensions, from the continental shelf into the deep water, could give new information about volcanic eruptions at depth and the effect of the depth and pressure on submarine cone formation.

## References Cited

- Adiyaman, Ö., Chorowicz, J., Köse, O., (1998). Relationship between volcanic patterns and neotectonics in Eastern Anatolia from analysis of satellite images and DEM. *Journal of Volcanology and Geothermal Research*. 85: pp.17-32.
- Anderson, E.M. (1951). *The Dynamics of Faulting and Dyke Formation with Applications to Britain*, 2<sup>nd</sup> Edition, Oliver and Boyd, Edinbough, p. 206.
- Barr, D. (2014). A Morphological Investigation of Submarine Volcanic Cones and their Relation to Crustal Stress, Adare Basin, Antarctica. Senior Thesis, The Ohio State University. pp. 1-43.
- Cande, S.C., J.M. Stock, R.D. Müller, and T. Ishihara (2000). Cenozoic motion between East and West Antarctica. *Nature*, 404, 145-150.
- Cande, S. C., and J. M. Stock (2006), Constraints on the timing of extension in the Northern Basin, Ross Sea, in *Antarctic Contributions to Global Earth Science*, edited by D. K. Fütterer et al., pp. 317–324, Springer, Berlin.
- Elliot, D. (1992). Jurassic magmatism and tectonism associated with Gondwanaland break-up: an Antarctic perspective. *Geological Society, London, Special Publications*, 68(1), pp.165-184.
- Faccenna, C., F. Rossetti, T. W. Becker, S. Danesi, and A. Morelli (2008), Recent extension driven by mantle upwelling beneath the Admiralty Mountains (East Antarctica). *Tectonics*. 27, TC4015, doi:10.1029/2007TC002197
- Fitzgerald, P. (2002). Tectonics and landscape evolution of the Antarctic plate since the breakup of Gondwana, with an emphasis on the West Antarctic Rift System and the Transantarctic Mountains. *Royal Society of New Zealand Bulletin*. 35, pp. 453-469.
- Granot, R., Cande, S., Stock, J., Davey, F. and Clayton, R. (2010). Postspreading rifting in the Adare Basin, Antarctica: Regional tectonic consequences. *Geochemistry, Geophysics, Geosystems*, 11(8), pp. 1-29.
- Heimann, A., T. Fleming, D. Elliot, and K. Foland (1994), A Short Interval of Jurassic Continental Flood - Basalt Volcanism in Antarctica as Demonstrated by <sup>40</sup>Ar/<sup>39</sup>Ar Geochronology. *Earth Planet. Sci. Lett.*, 121(1-2), 19-41.
- Lanier, A., Romsos, C. and Goldfinger, C. (2007). Seafloor Habitat Mapping on the Oregon Continental Margin: A Spatially Nested GIS Approach to Mapping Scale, Mapping Methods, and Accuracy Quantification. *Marine Geodesy*, 30(1-2), pp.51-76.
- Lundblad, E., Wright, D., Miller, J., Larkin, E., Rinehart, R., Naar, D., Donahue, B., Anderson, S. and Battista, T. (2006). A Benthic Terrain Classification Scheme for American Samoa. *Marine Geodesy*, 29(2), pp.89-111.

- Müller, R., Cande, S., Stock, J. and Keller, W. (2005). Crustal structure and rift flank uplift of the Adare Trough, Antarctica. *Geochemistry, Geophysics, Geosystems*. 6(11), pp. 1-16
- Nakamura, K. (1977). Volcanoes as possible indicators of tectonic stress orientation – principle and proposal. *Journal of Volcanology and Geothermal Research*. 2, pp. 1-16.
- Oceanservice.noaa.gov, (2014). *What is bathymetry?*. [online] Available at: <http://oceanservice.noaa.gov/facts/bathymetry.html> [Accessed 8 Nov. 2014].
- Panter, K.S. & Castillo P. (2007) Petrogenesis and source of lavas from seamounts in the Adare Basin, Western Ross Sea: Implications for the origin of Cenozoic magmatism in Antarctica. *U.S. Geological Survey and the National Academies*. 1047, pp.1-4.
- Paulsen, T. S., & Wilson, T. J. (2009). Structure and age of volcanic fissures on Mount Morning: A new constraint on Neogene to contemporary stress in the West Antarctic Rift, southern Victoria Land, Antarctica. *Geological Society of America Bulletin*. 121(7-8), 1071-1088.
- Paulsen, T. S., & Wilson, T. J. (2010). Evolution of Neogene volcanism and stress patterns in the glaciated West Antarctic Rift, Marie Byrd Land, Antarctica. *Journal of the Geological Society*. 167(2), 401-416.
- Rinehart, R., D. Wright, E. Lundblad, E. Larkin, J. Murphy, and L. Cary-Kothera. (2004). ArcGIS 8.x Benthic habitat extension: Analysis in American Samoa. In Proceedings of the 24th Annual ESRI User Conference. San Diego, CA, August 9–13. Paper 1433.
- Rosenbeck, L. (2013). A morphometric and alignment analysis of volcanic seamounts to determine stress directions, northwestern Ross Sea, Antarctica. Senior Thesis, The Ohio State University. pp.1-41.
- Smellie, J., Rocchi, S., Gemelli, M., Di Vincenzo, G. and Armienti, P. (2011). A thin predominantly cold-based Late Miocene East Antarctic ice sheet inferred from glaciovolcanic sequences in northern Victoria Land, Antarctica. *Palaeogeography, Palaeoclimatology, Palaeoecology*, 307(1-4), pp.129-149.
- Van der Pluijm, B., and Marshak, S.,(2004) *Earth Structure*. New York, NY: W.W. Norton & Company Ltd.



## Appendix A

|      | EAST (Degrees) |         |         | WEST (Degrees) |         |            |
|------|----------------|---------|---------|----------------|---------|------------|
| Cone | Seafloor A     | Apron A | Flank A | Flank B        | Apron B | Seafloor B |
| 1    | 3.02           | 7.7     | 21.34   | 18.91          | 8.53    | 0.43       |
| 2    | 1.8            | 15.67   | 30.96   | 28.26          | 14.56   | 2.54       |
| 3    | 1.51           | 7.71    | 28.07   | 21.43          | 5.12    | 1.1        |
| 4    | -              | -       | -       | -              | -       | -          |
| 5    | -              | -       | 19      | 23.25          | 5.08    | 0.05       |
| 6    | -              | -       | 16.7    | 27.75          | 8.46    | 0.67       |
| 7    | 3.32           | 16.7    | 28.26   | 28.5           | 11.5    | 0.05       |
| 8    | 1.02           | 8.11    | 18.5    | 18.55          | 9.38    | 3.51       |
| 8a   | 1.18           | 5.02    | 18.92   | 19.82          | 5.98    | 0.13       |
| 9    | -              | 7.54    | 19.37   | 19.87          | 5.16    | 1.38       |
| 10   | 0.77           | 4.5     | 22.18   | 26.68          | 6.15    | 0.12       |
| 11   | -              | -       | 30.67   | 26.33          | 15.05   | 1.88       |
| 12   | -              | -       | 28.46   | 27.46          | 12.36   | 0.24       |
| 13   | -              | -       | -       | -              | -       | -          |
| 14   | -              | 13.68   | 28.21   | 32.17          | 14.29   | -          |
| 15   | -              | -       | -       | 26.87          | 11.81   | 0.01       |
| 16   | -              | -       | -       | 24.45          | 9.29    | 0.81       |
| 17   | -              | -       | -       | 21.06          | -       | -          |
| 17a  | -              | -       | -       | 21.35          | 5.39    | 0.98       |
| 18   | 3.31           | 6.74    | 28.53   | 25.36          | 11.33   | 1.62       |
| 18a  | -              | -       | -       | -              | -       | -          |
| 18b  | 1.25           | 8.54    | 26.76   | 25.72          | -       | -          |
| 18c  | 1.98           | 11.23   | 34.43   | 20.88          | 12.83   | 0.91       |
| 19   | -              | -       | -       | 21.43          | -       | -          |
| 20   | 4.27           | 13.64   | 24.39   | 27.73          | 11.34   | 3.92       |
| 21   | -              | -       | 14.7    | 21.85          | 11.61   | 4.78       |
| 22   | 2.02           | 10.32   | 22.42   | 28.07          | -       | -          |
| 23   | 2.75           | 11.1    | 27.44   | 30.65          | 14.14   | -          |
| 24   | 2.4            | 15.37   | 30.32   | 25.65          | -       | -          |
| 25   | -              | -       | 28.95   | 29.12          | -       | -          |
| 26   | -              | -       | -       | 22.61          | 11.04   | 0.76       |
| 27   | 0.71           | 8.3     | 23.92   | 22.73          | 11.76   | 1.08       |

| Ridge Segment | Length (meters) | Azimuth (Degrees) |
|---------------|-----------------|-------------------|
| 1             | 6226            | 195               |
| 2             | 9738            | 188               |
| 3             | 7735            | 204               |
| 4             | 6690            | 188               |

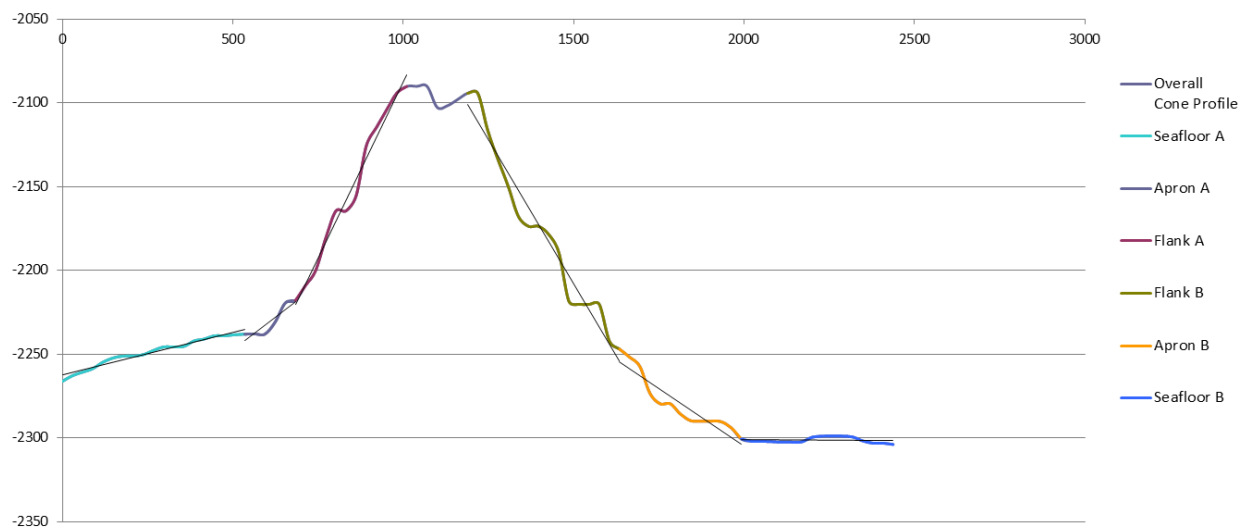
| Cone Number | Short Axis Length<br>(meters) | Long Axis Length<br>(meters) | Long Axis Azimuth<br>(Degrees) |
|-------------|-------------------------------|------------------------------|--------------------------------|
| 1           | Circle                        |                              |                                |
| 2           | 1730                          | 2043                         | 197                            |
| 3           | 1316                          | 2144                         | 198                            |
| 4           | 1032                          | 1205                         | 163                            |
| 5           | Circle                        |                              |                                |
| 6           | 986                           | 1382                         | 185                            |
| 7           | 2155                          | 2555                         | 111                            |
| 8           | 1270                          | 2033                         | 242                            |
| 8a          | 795                           | 892                          | 153                            |
| 9           | 1173                          | 1567                         | 158                            |
| 10          | 992                           | 1135                         | 167                            |
| 11          | 1071                          | 1265                         | 207                            |
| 12          | 1382                          | 1476                         | 195                            |
| 14          | 975                           | 1152                         | 169                            |
| 15          | 946                           | 1624                         | 198                            |
| 16          | 833                           | 1429                         | 188                            |
| 17          | 574                           | 976                          | 177                            |
| 17a         | Circle                        |                              |                                |
| 18          | Circle                        |                              |                                |
| 18a         | 906                           | 1423                         | 191                            |
| 18b         | 1048                          | 1296                         | 213                            |
| 18c         | 1177                          | 1637                         | 183                            |
| 19          | Circle                        |                              |                                |
| 20          | 1302                          | 1317                         | 185                            |
| 21          | Circle                        |                              |                                |
| 22          | 938                           | 1475                         | 171                            |
| 23          | 1060                          | 1224                         | 190                            |
| 24          | 1138                          | 1469                         | 189                            |
| 25          | 1072                          | 1662                         | 207                            |
| 26          | 1286                          | 1983                         | 120                            |
| 27          | 2075                          | 2911                         | 164                            |

| Cone Alignment | Alignment Length (meters) | Azimuth (Degrees) |
|----------------|---------------------------|-------------------|
| 1              | 6273                      | 187               |
| 2              | 6100                      | 206               |
| 3              | 5817                      | 128               |
| 4              | 4778                      | 209               |
| 5              | 5437                      | 197               |
| 6              | 4587                      | 187               |
| 7              | 6345                      | 164               |
| 8              | 8485                      | 183               |
| 9              | 3999                      | 166               |

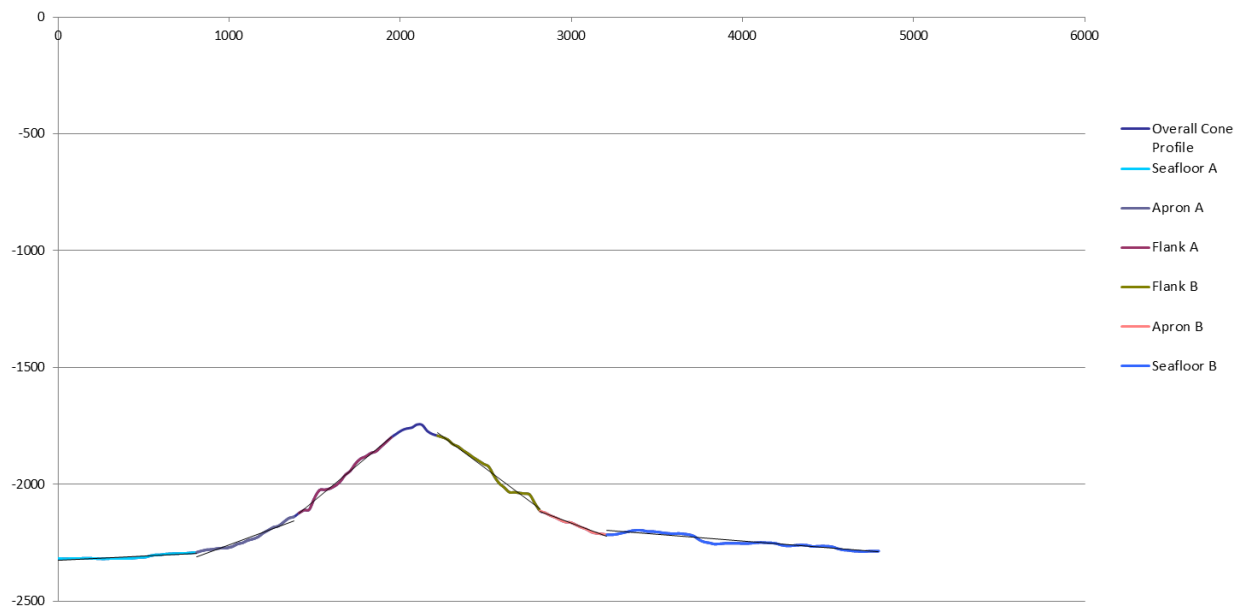
### **Excel Cone Profiles**

The following figures are the profiles for each cone analyzed for break in slope. All figures have an x axis of distance in meters and a y axis of depth in meters.

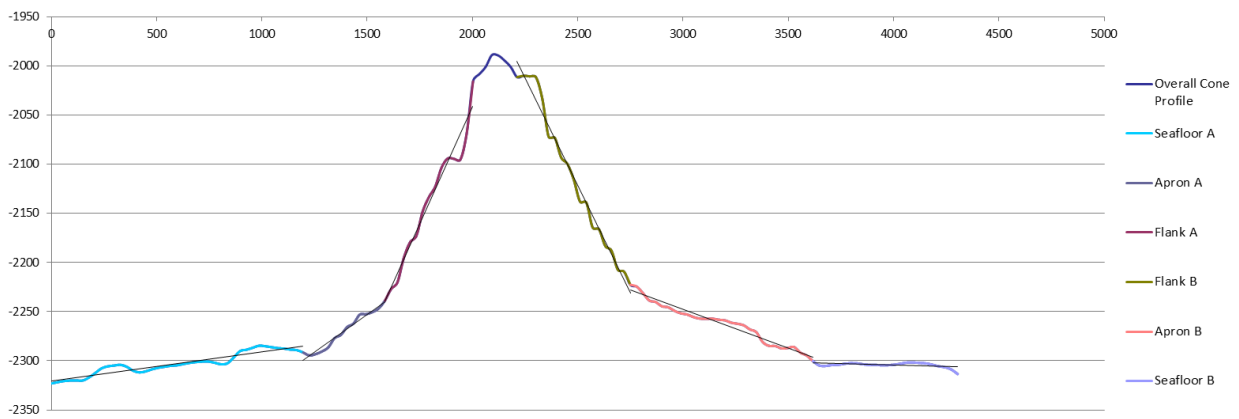
#### **Cone 1**



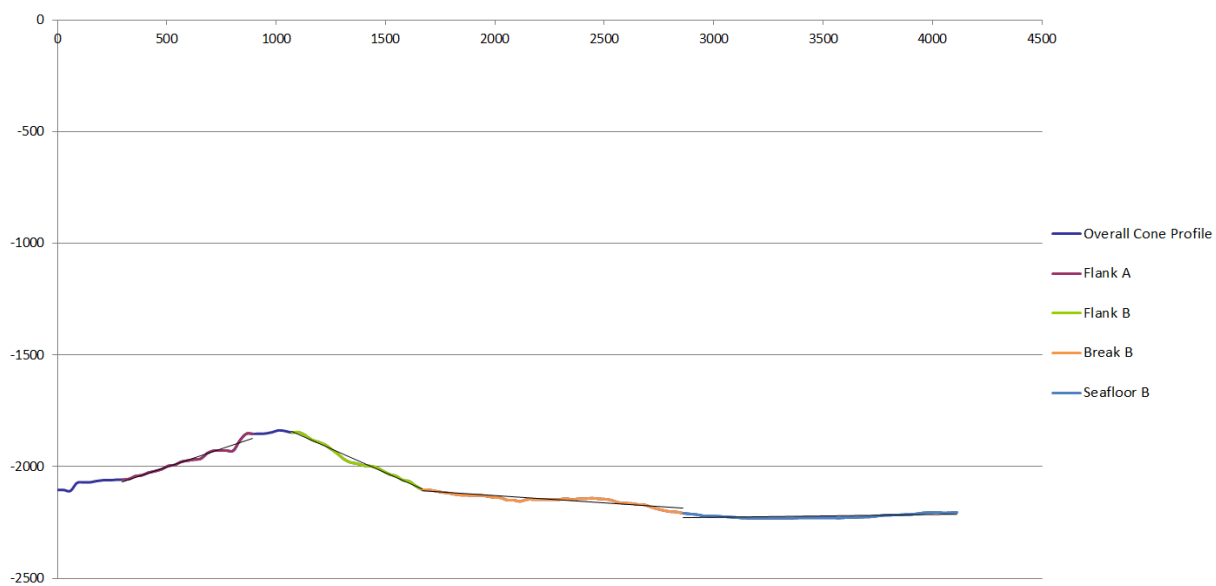
## Cone 2



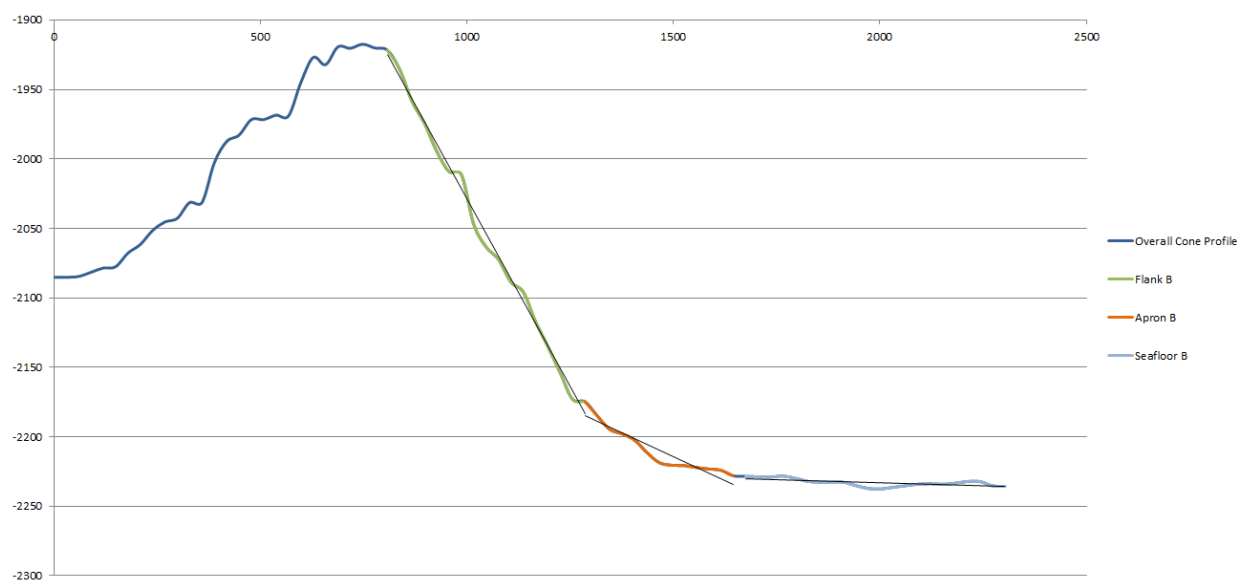
## Cone 3



## Cone 5

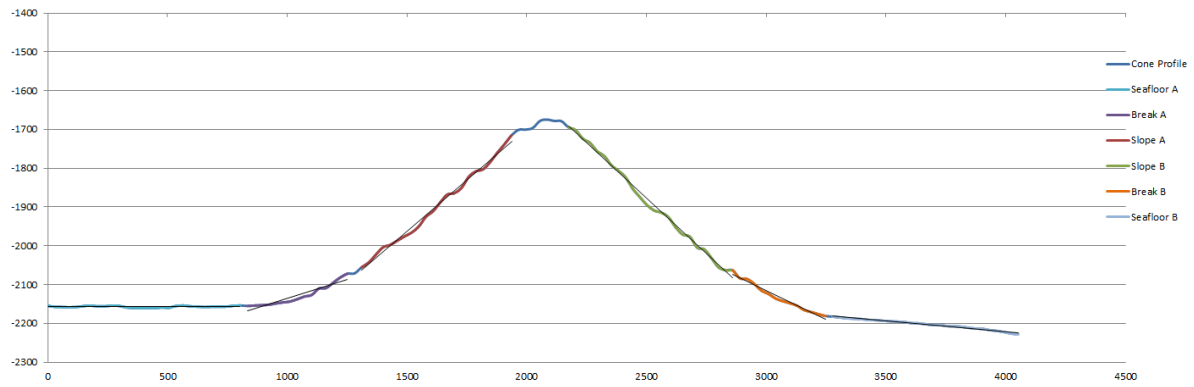


## Cone 6

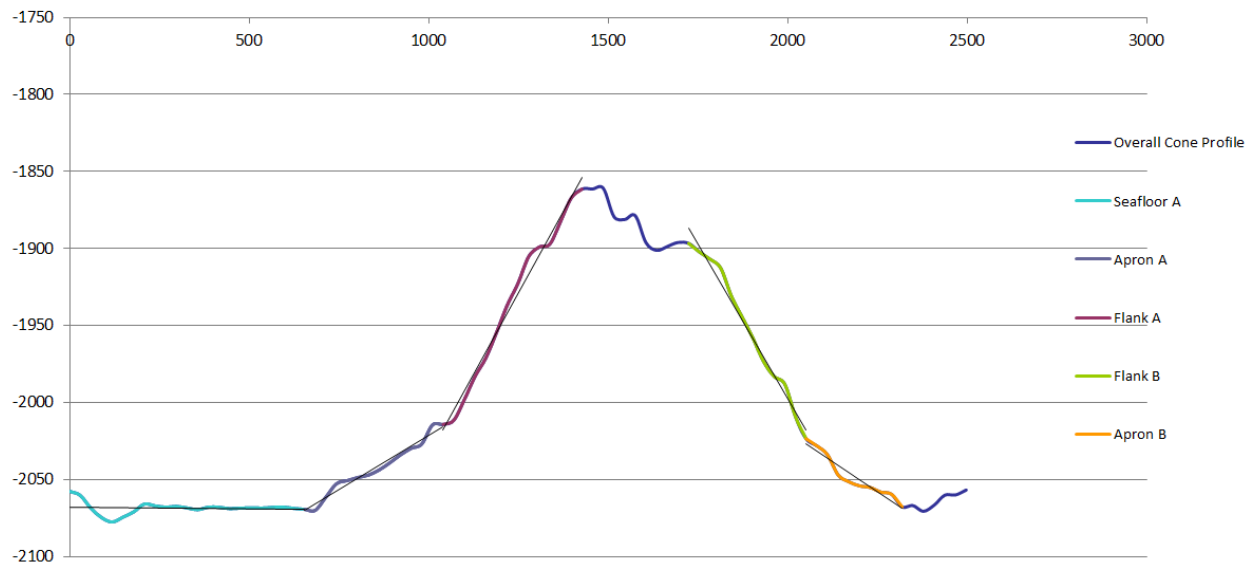




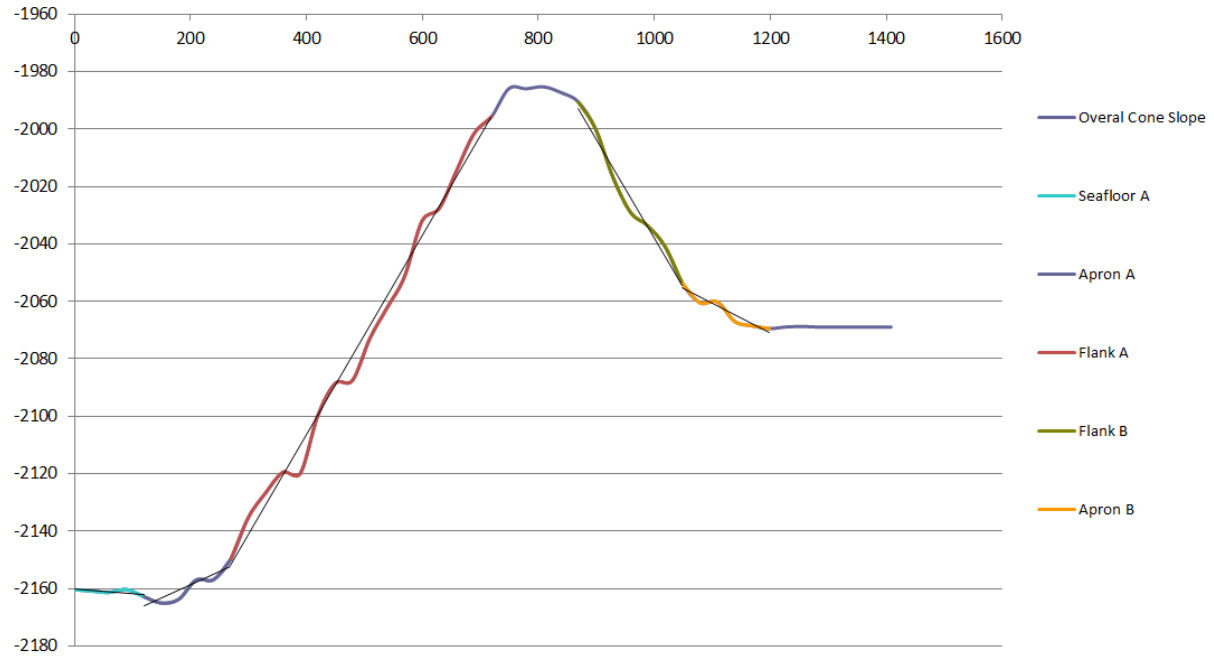
## Cone 7



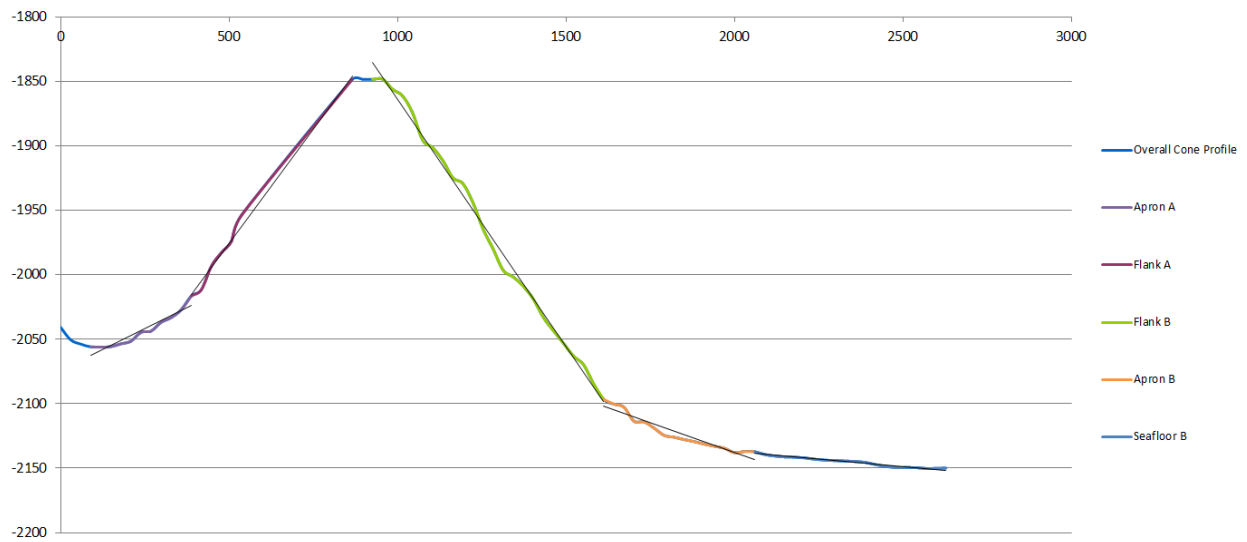
## Cone 8



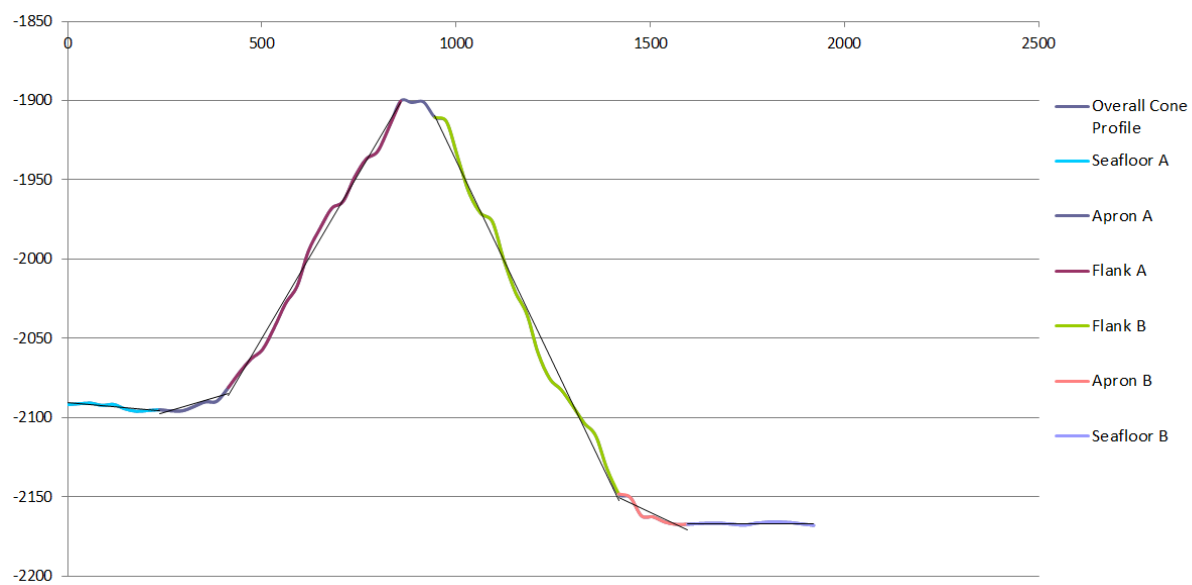
## Cone 8a



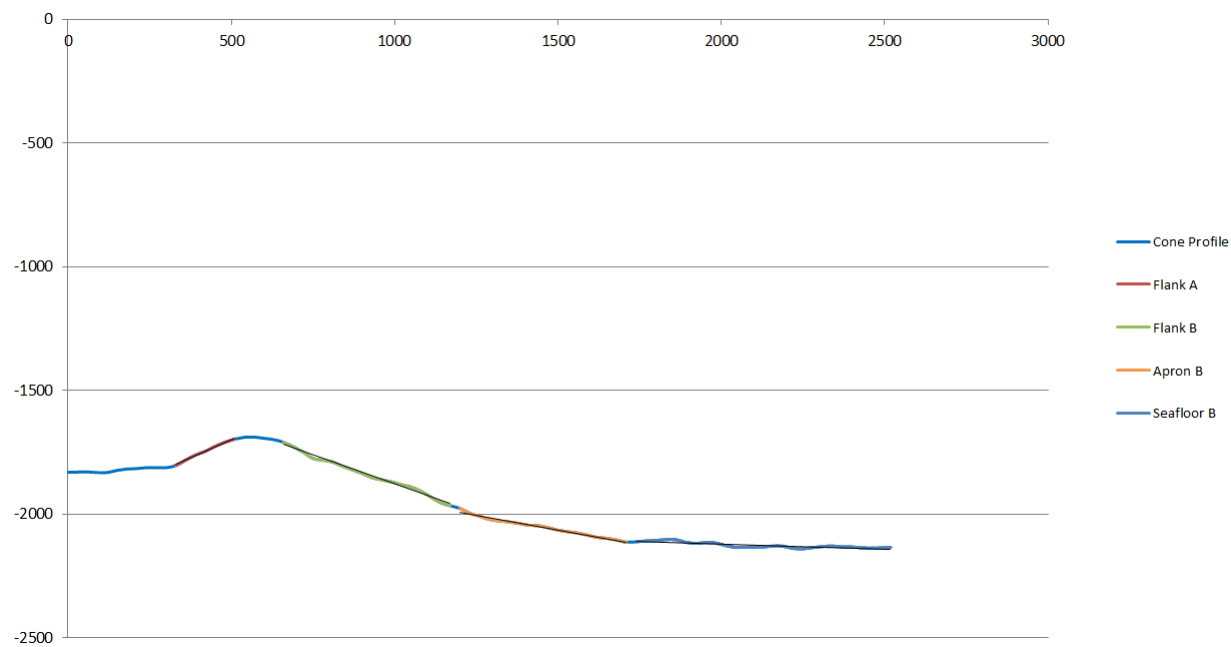
## Cone 9



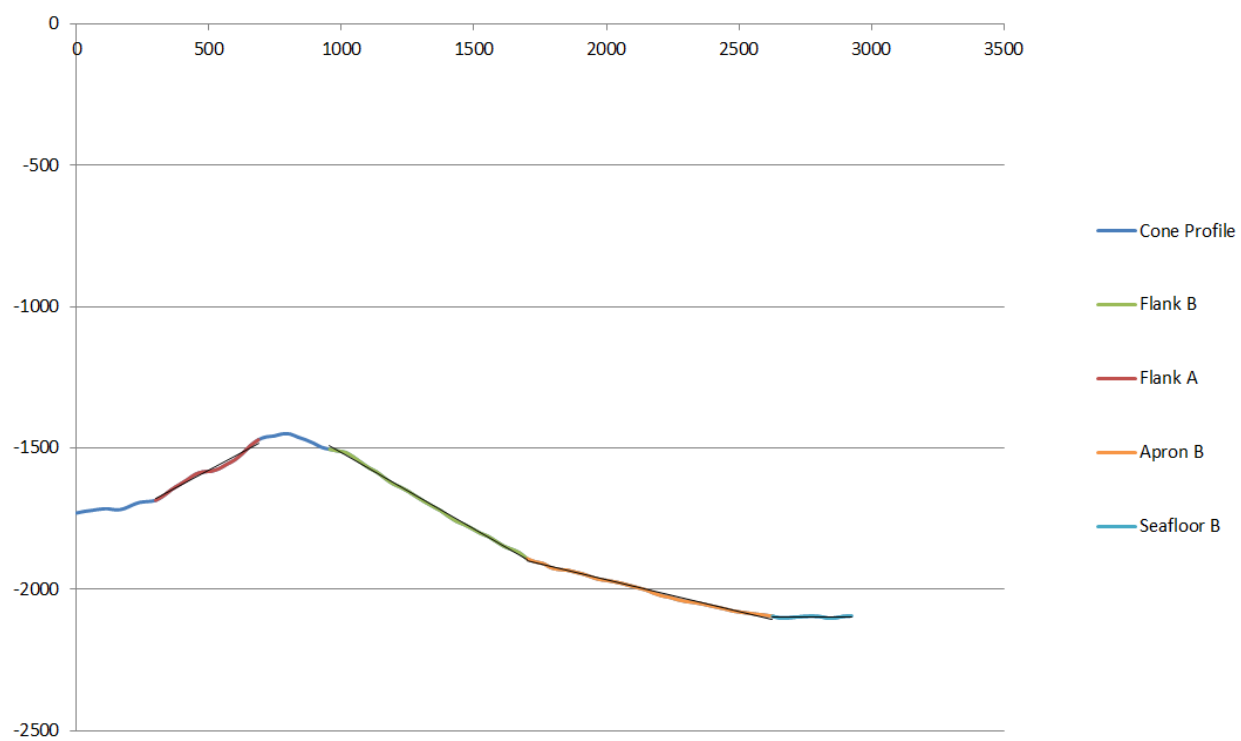
## Cone 10



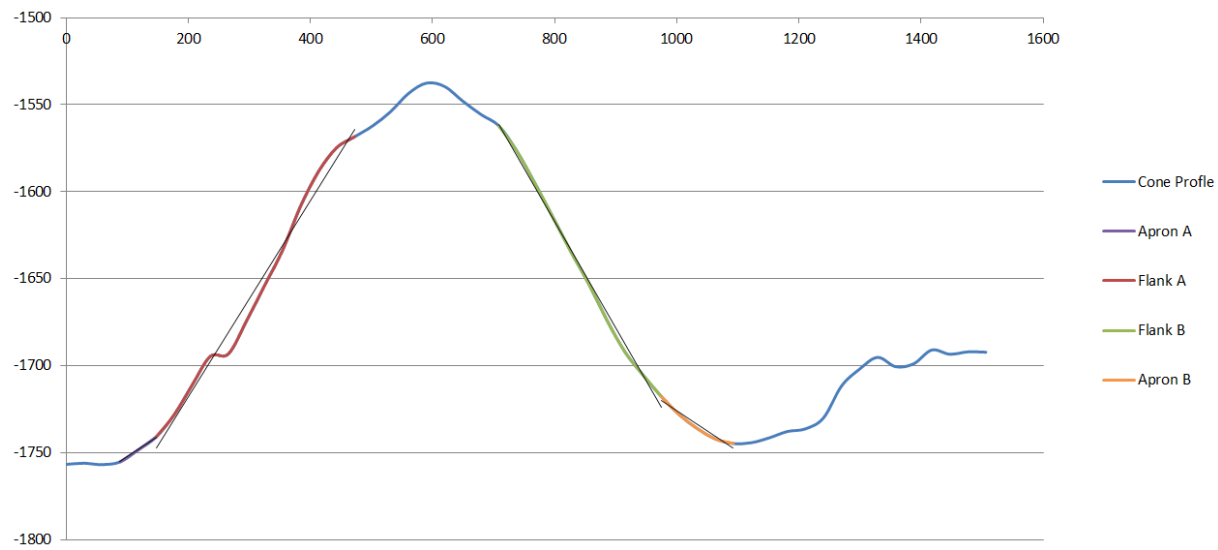
## Cone 11



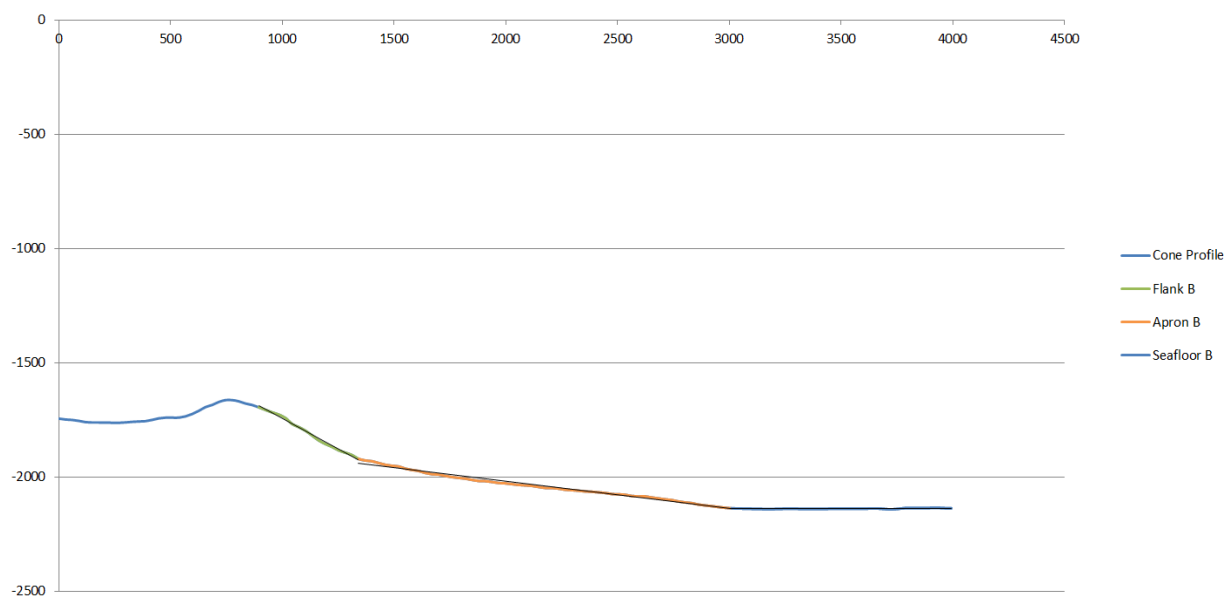
## **Cone 12**



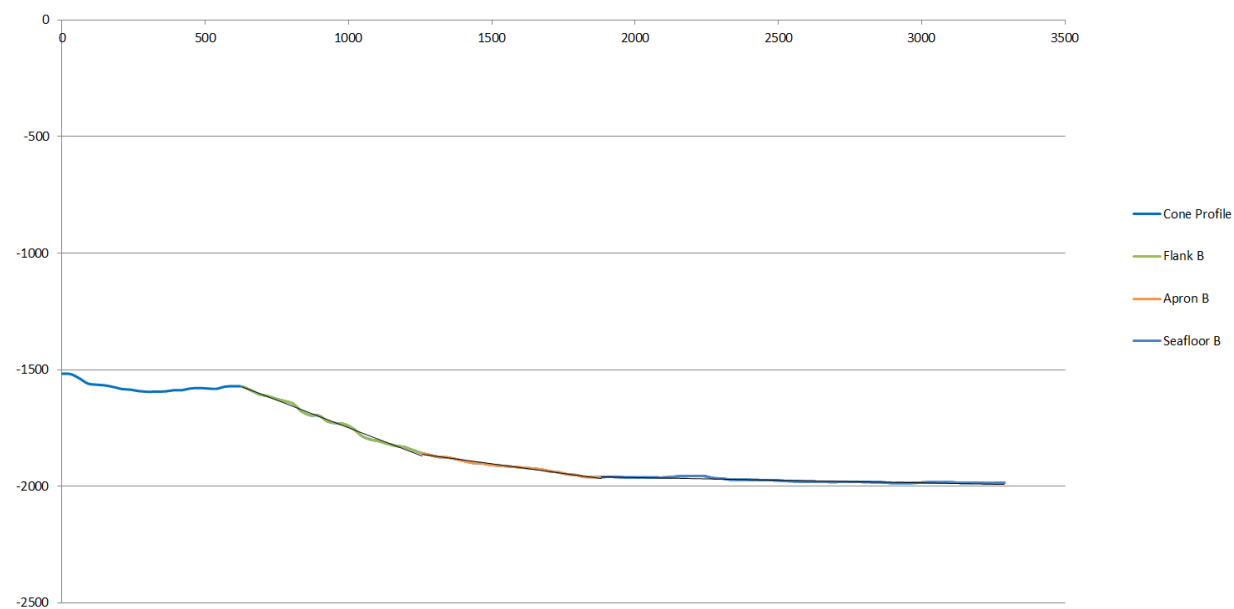
## **Cone 14**



## Cone 15

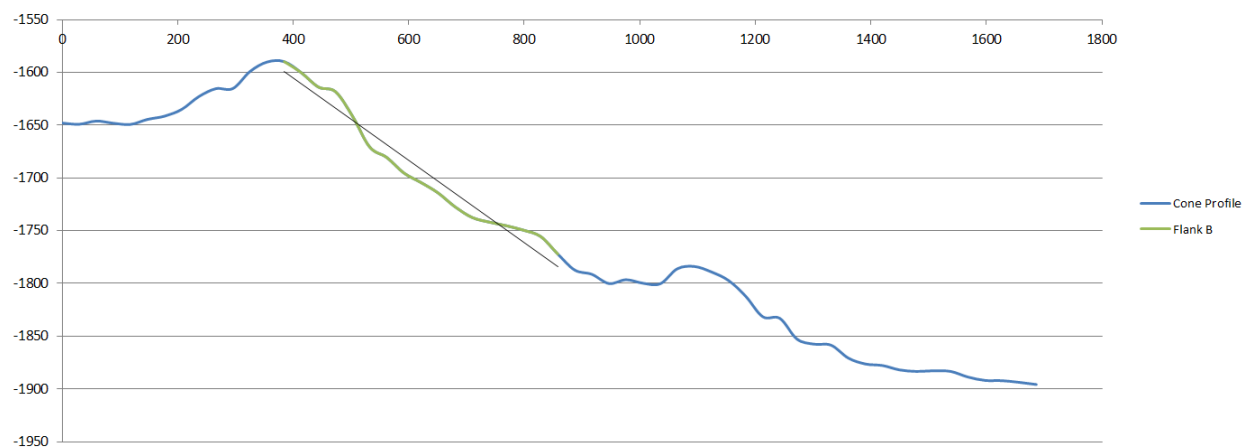


## Cone 16

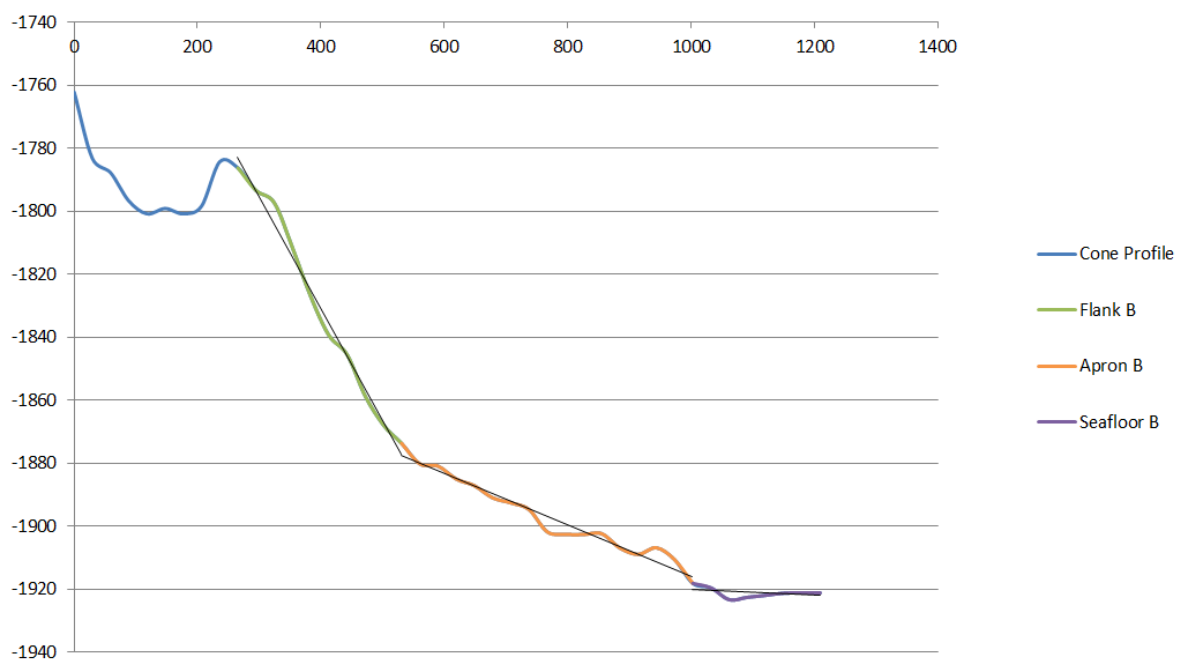




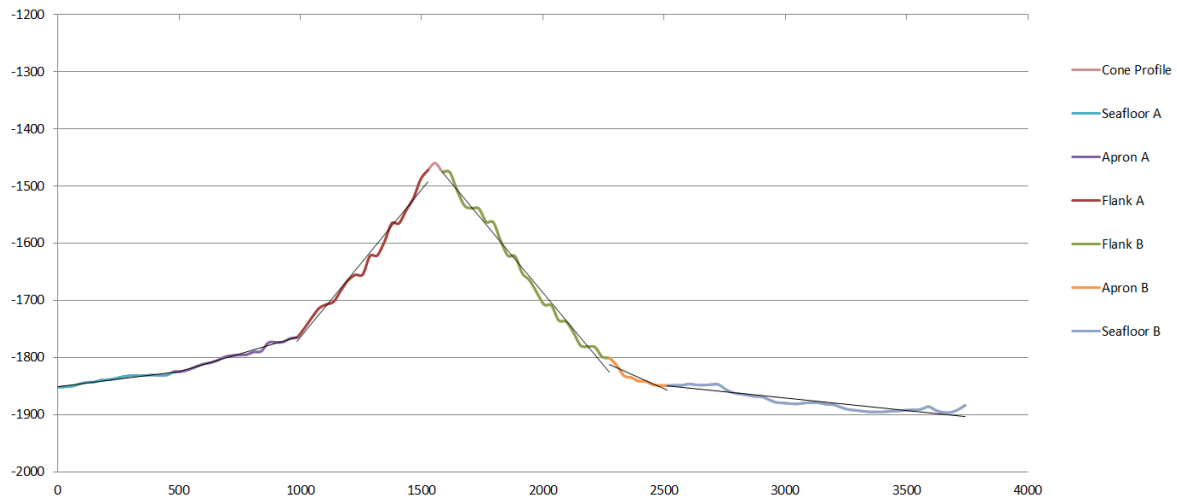
## **Cone 17**



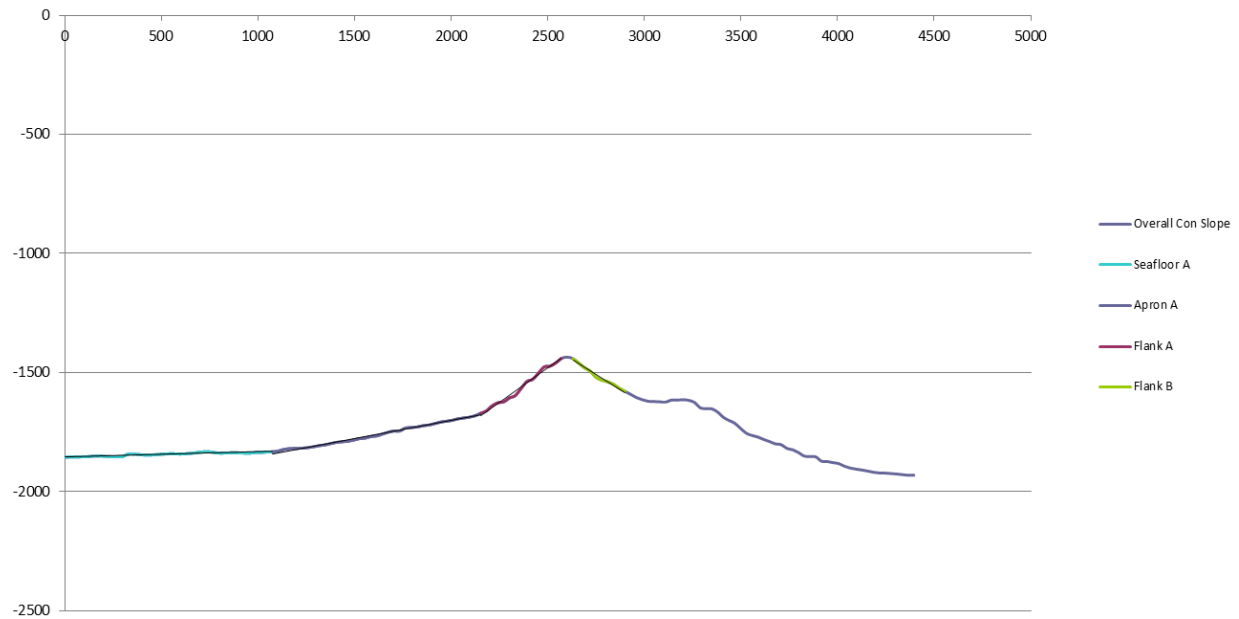
## **Cone 17a**



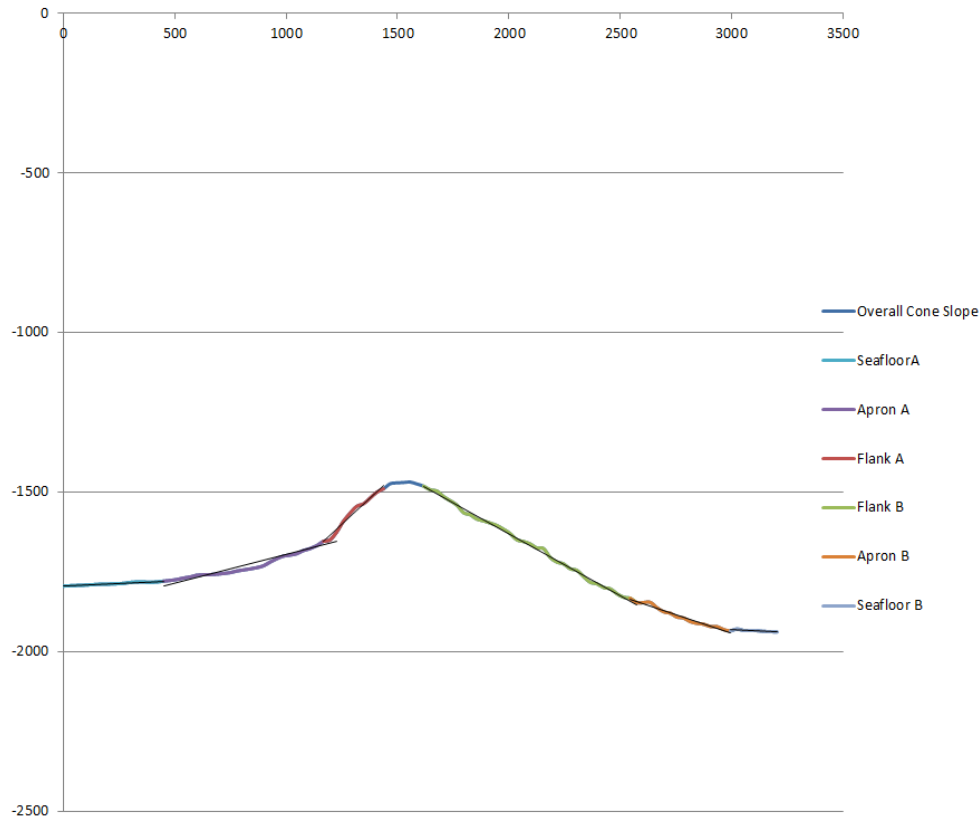
## Cone 18



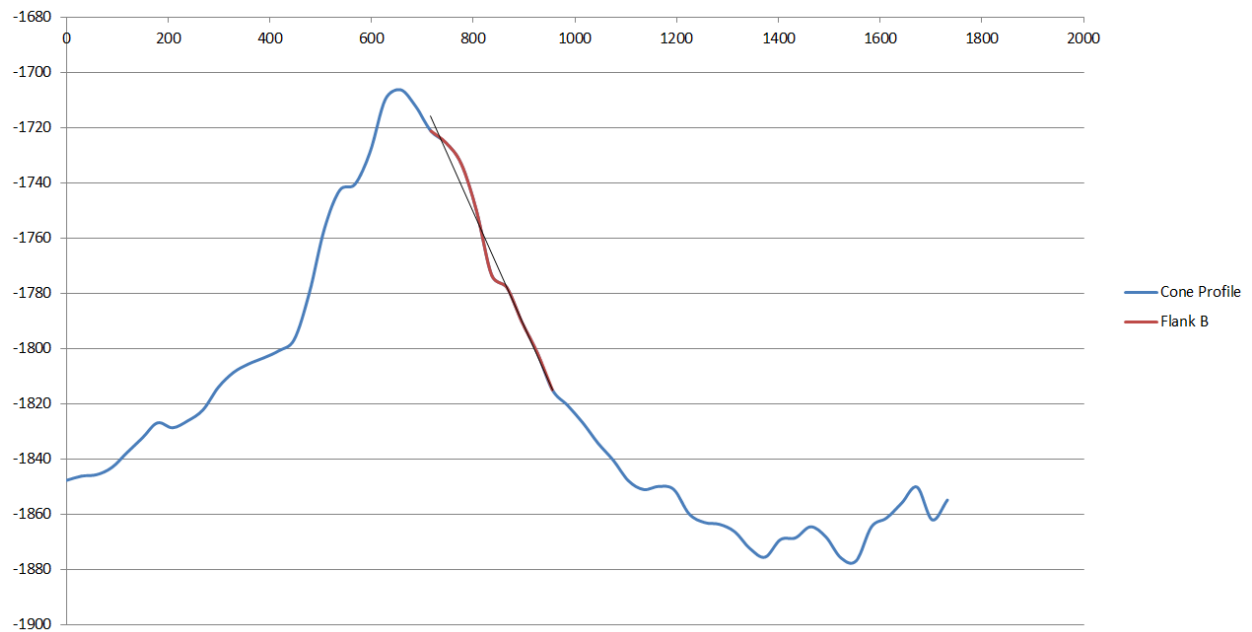
## Cone 18b



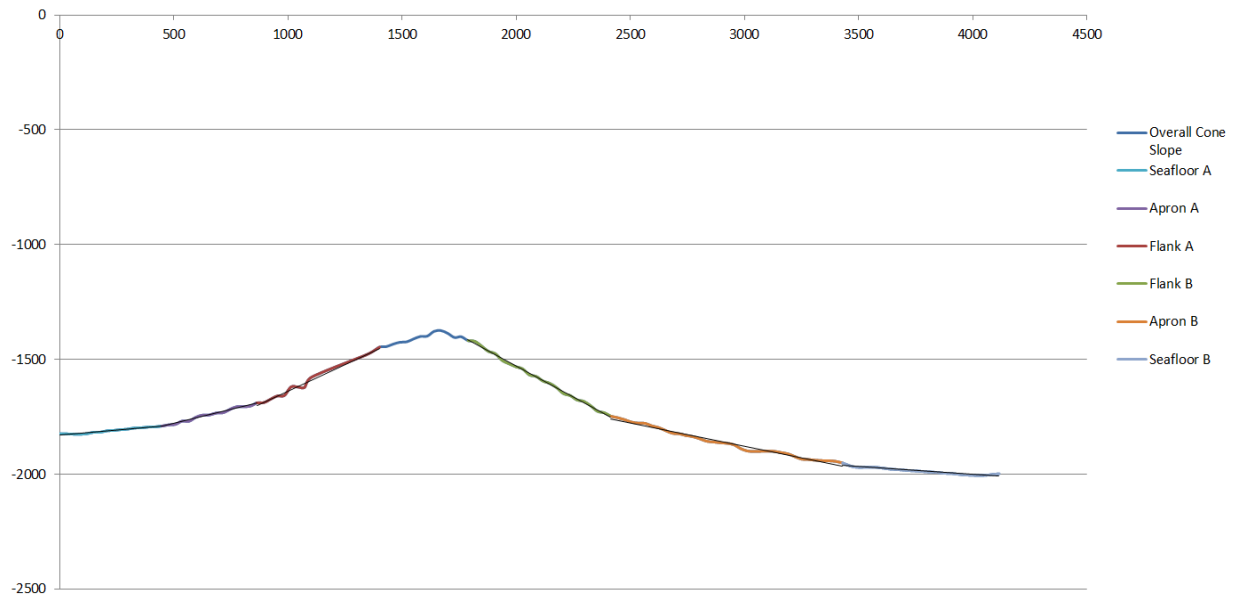
## Cone 18c



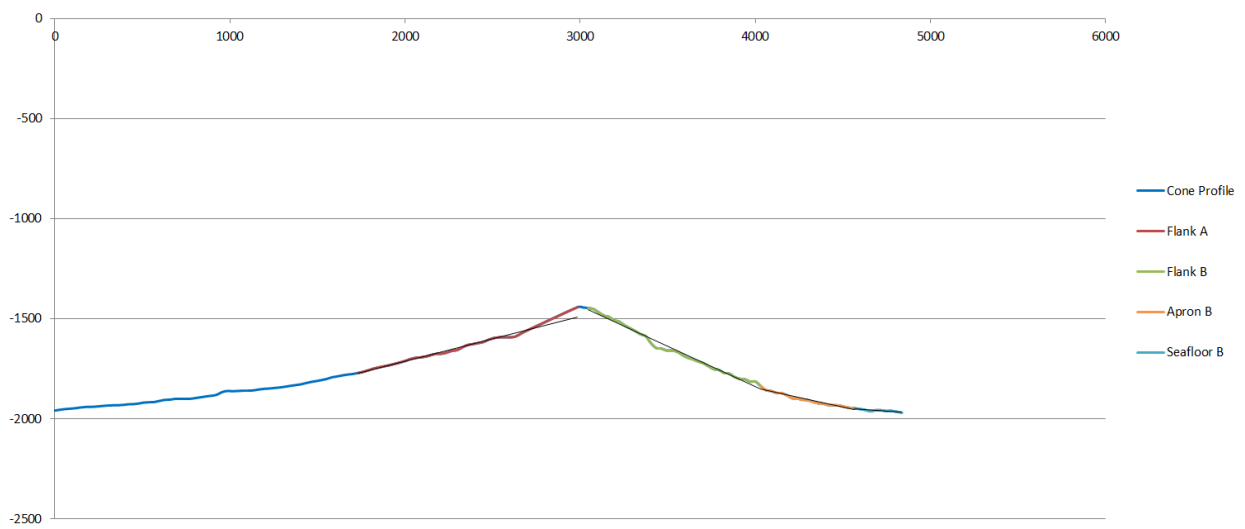
## Cone 19



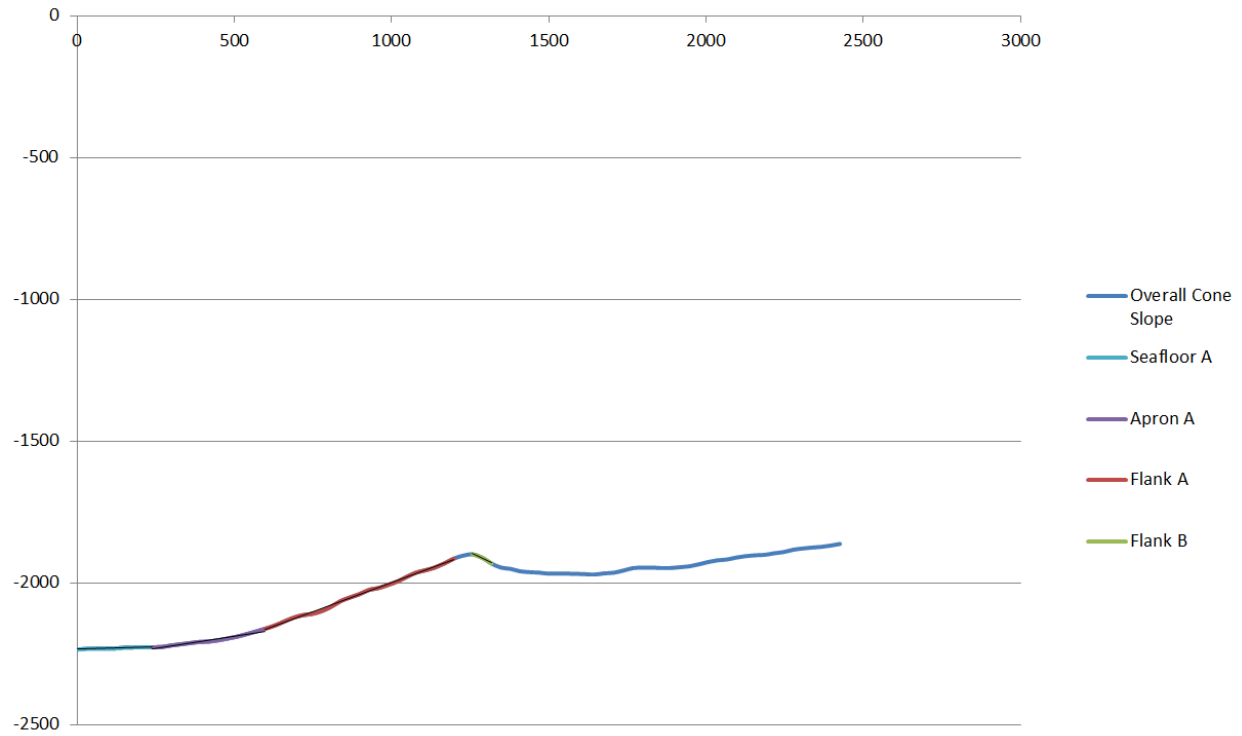
## Cone 20



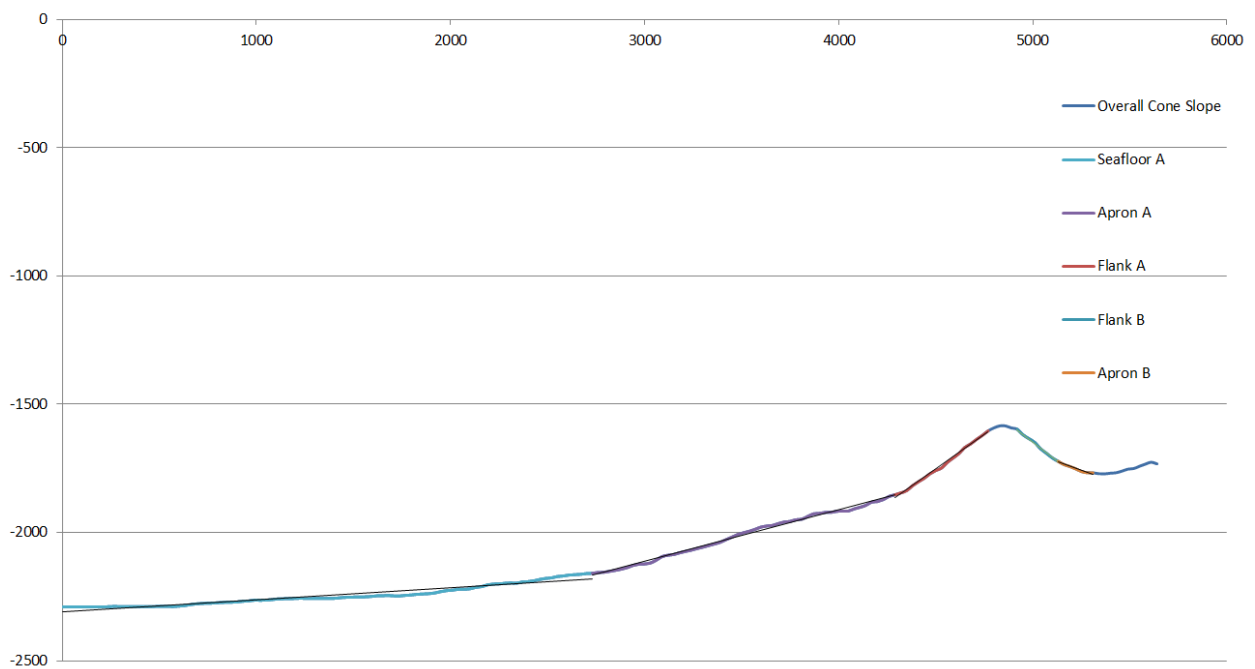
## Cone 21



## Cone 22

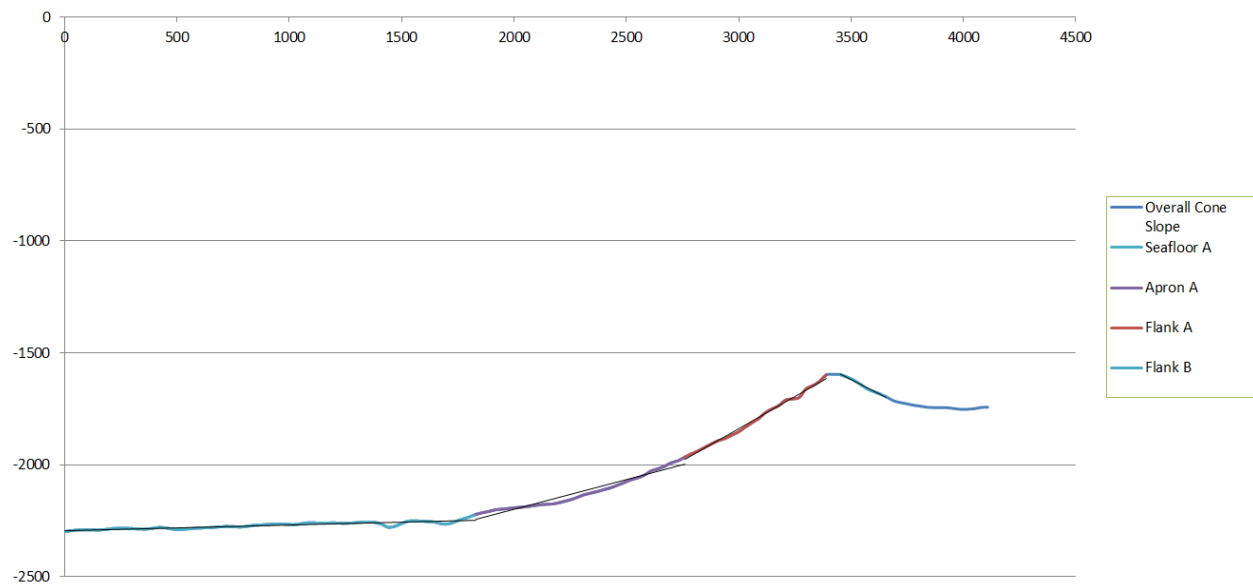


## Cone 23

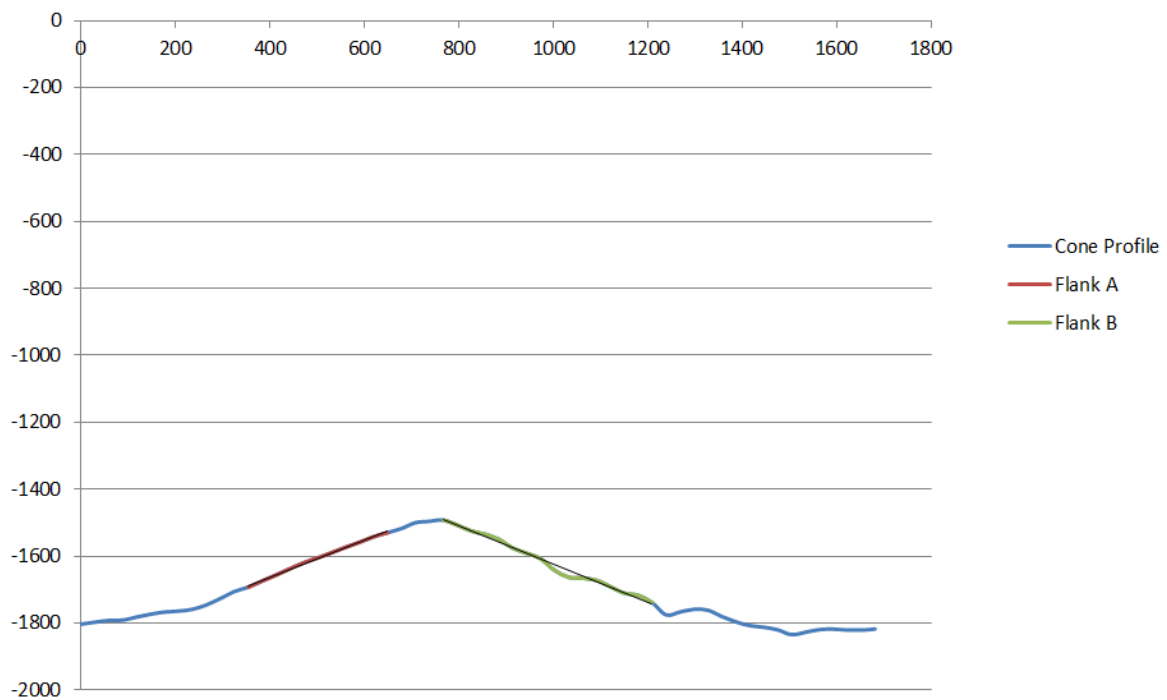




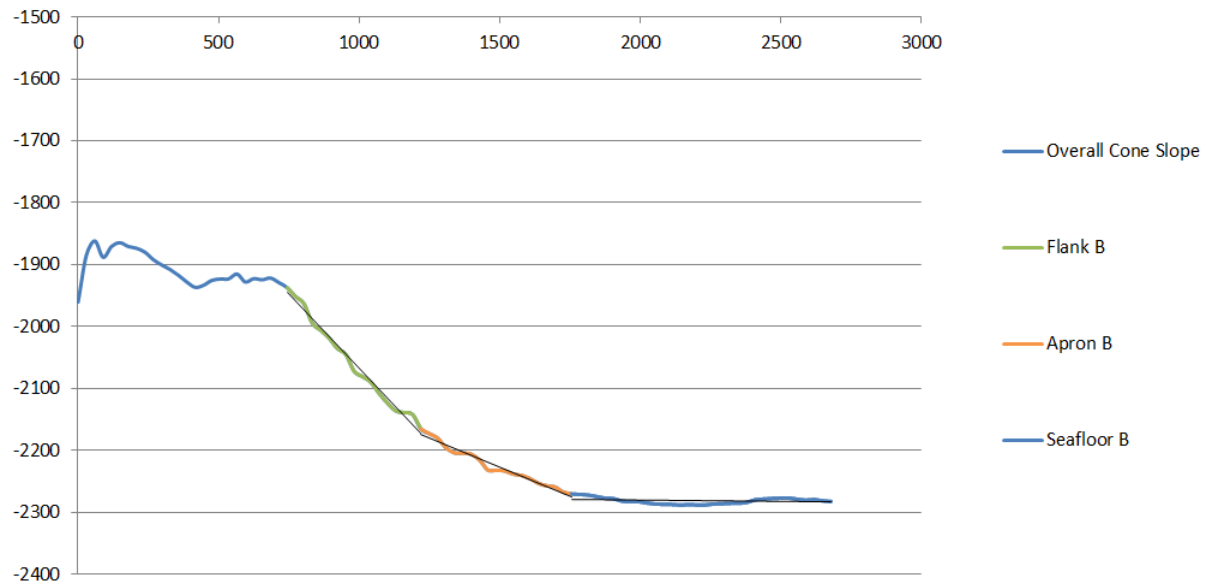
## Cone 24



## Cone 25



## Cone 26



## Cone 27

